Fall 2007

Shielding characteristics of a commercial 19-inch rack-based cabinet

Jue Chen

Department:

SHIELDING CHARACTERISTICS OF A COMMERCIAL 19-INCH RACK-BASED CABINET

by

JUE CHEN

A THESIS

Presented to the Faculty of the Graduate School of the

UNIVERSITY OF MISSOURI-ROLLA

In Partial Fulfillment of the Requirements for the Degree

MASTER OF SCIENCE IN ELECTRICAL ENGINEERING

2007

Approved by

_____	_____
R. E. DuBroff, Advisor	J. L. Drewniak

_____

D. J. Pommerenke

ABSTRACT

From an electromagnetic compatibility perspective, a commercial 19-inch rack-based cabinet of 40U height is comprised of different functional modules housed in well-shielded enclosures. Three methodologies are applied to investigate the overall shielding performance of various cabinet features, including doors, side panels and cable egress, an important feature that is of primary interest here.

The first methodology discussed is the in situ measurements on a functioning cabinet using a spectrum analyzer. The second, and most detailed mythology discussed is the swept frequency three-port mixed-mode S-parameter measurements using a vector network analyzer. And the last is a HFSS simulation of a simplified cabinet model.

Results from the above approaches show that the rack cabinet, while not specifically designed to be a high-performance EMI shielded enclosure, does, however, provide about 5 to 10 dBμV/m of overall shielding performance that is important in meeting EMI regulatory requirements with the current system. The swept frequency approach, as proved, may be an effective method in the evaluation of shielding performance of similar equipment.

ACKNOWLEDGMENTS

I would like to express my sincere gratitude to Dr Richard E. DuBroff and Dr. James L. Drewniak, for their direction in this thesis, their teaching and instruction efforts on my research work, and the financial support to my study. I would also like to thank Dr. Pommerenke for the stimulating discussions and warm helps on my research topics.

I would like to extend my gratitude to Dr. James L. Knighten and Dr Jun Fan for their insightful guidance on this thesis topic and warm encouragement on my research. I would like to express my thanks to Roberta Cox for her efforts of checking the formatting of the thesis. I would also like to express my thanks to all the other faculty members and students in the UMR EMC Lab. It has been my great pleasure to work with you!

And last but not least, I would like to thank my husband Jianmin, my older sister Jianmin, my daughter Brianna and my son Andrew. Without their unconditional support, love, and encouragement, I would not be able to complete this work. I love you and thank you all!

TABLE OF CONTENTS

LIST OF ILLUSTRATIONS

LIST OF TABLES

1. DATA FROM NCR'S FUNCTIONING NODE RACK CABINET

1.1. INTRODUCTION

From an electromagnetic compatibility perspective, the NCR node rack is comprised of different functional modules housed in well-shielded enclosures. The installation of these modules, including computer nodes, BYNET switch modules, Ethernet switches, Fiber Channel switches, and UPS power modules etc, is schematically illustrated in Figure 1.1. Communication between the modules internal to the rack is over copper cables that must penetrate the module enclosures. The copper cables exit the rack in order to provide connections to the power mains and communications with neighboring node and storage racks and an administrative workstation computer. The inherent imperfections in connector systems that are used in the equipment result in energy coupling to the cables, which in turn results in electromagnetic interference. The rack cabinet, while not specifically engineered to be a superior EMI shielding enclosure, does, however, provide on the order of 10 dB of overall shielding effectiveness that is essential in meeting EMI regulatory requirements with the current system.

Currently, the cable egress is through a large opening in the bottom of the rack near the floor of the datacenter. An engineering design change being considered to the rack equipment is to change the egress of the cables from the rack out the top as opposed to out the bottom. This change can have significant EMI consequences. Measurements on the NCR system were conducted at NCR to quantify the shielding effectiveness of the rack cabinet, and to conduct measurements on the impact of the cable egress from the top of the rack, as opposed to the bottom. Shielding effectiveness of the rack cabinet on the order of 5 -10 dB was measured over a broad frequency range for the functioning equipment. Further, modifications to the equipment that brought the cables out the top of the rack resulted in exceeding the EMI regulatory limit at the critical BYNET frequency of 627 MHz.

The major results and conclusions of these measurements were discussed in a previous report [1]. A more detailed data analysis is presented herein.

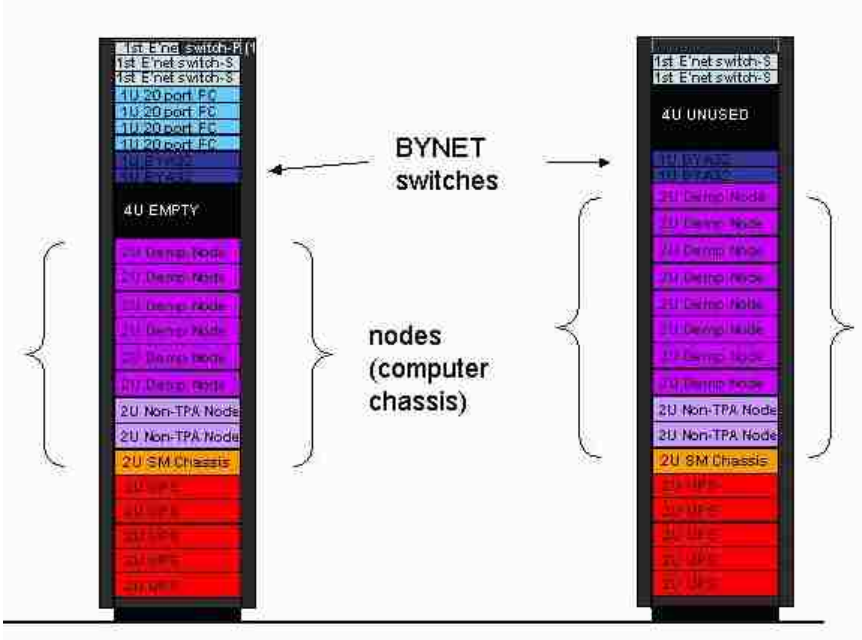

Figure 1.1. Schematic Representation of the NCR Node Rack Equipment

1.2. EMI MEASUREMENTS ON THE RACK EQUIPMENT

The equipment under test (EUT) was staged in the NCR's 3 m chamber and including three interconnected equipment racks: (1) the storage rack, (2) the node rack, (3) a BYNET cabinet, and the AWS controller. (It should be noted that the node rack was configured in a conventional Rittal rack, whereas the storage rack and the BYNET systems were configured in the new, cost-reduced rack.) Digital photographs of the equipment with the cable egress at the bottom of the rack cabinet, which was standard for all working node racks, are shown in Figures 1.2. The cabinet on the right is filled with node chasses, and the cabinet on the left is the disk array rack. Since the signals in and out of the disk array cabinet are on optical fibers, the measurements focused on the node and BYNET cabinets. EMI measurements were conducted for various node rack test configurations, combined with the antenna setups, as shown in Table 1.1.

Because of the superior chassis design used in the individual module chasses, the EMI coupling path out of these enclosures is dominated by the chassis/connector interface, e.g., the HSSDC2, and results in common-mode currents on the cables within

Figure 1.2. Digital Photographs of the NCR Node Rack Equipment from Two Different Angles

the larger cabinet rack. Consequently, the measured radiation is always greatest from the rear of the cabinet, both with the door closed as well as open.

To determine approximately the overall shielding effectiveness of the cabinet rack, with the current cable egress at the bottom of the node rack cabinet, an A/B comparison was made with the rear of the cabinets facing the antenna. The measurements were made with the rear cabinet doors closed, and then the identical measurements were made with the cabinet doors open.

Table 1.1. Antenna Setups

	Vertical polarization	Horizontal polarization
Height at 1 m	√	√
Height at 2 m	√	√

For the test configuration of the cable egress at the top of the node rack cabinet, a large aperture approximately 9”x12” was cut in the top panel to allow all the cables to come out the top of the node cabinet rack. The BYNET cables were then routed through the approximately 2” holes that were standard in the rack. The power (thick cable with the large yellow connector) and AWS communication cables were draped from the node rack to the floor. The cable attenuations were included in the spectrum analyzer settings, and the receiving antenna was positioned in both the vertical and horizontal polarizations for the measurements, and raised to a height of 2 m, where the radiation was a maximum (as dictated by the FCC standards).

1.3. RESULTS AND DATA ANALYSIS

Figure 1.3 shows the screen shots of the data of the measurements with the AWS controller off and BYNET cabinet not connected. It is a baseline measurement as the interest here is in the effect of the BYNET activity on the EMI of the node rack cabinets. With the antenna factor known, as shown in Figure 1.4, the results are tabulated in Table 1.2 and plotted in Figure 1.5 with the frequency range of 30 MHz – 6 GHz. The antenna factor is included.

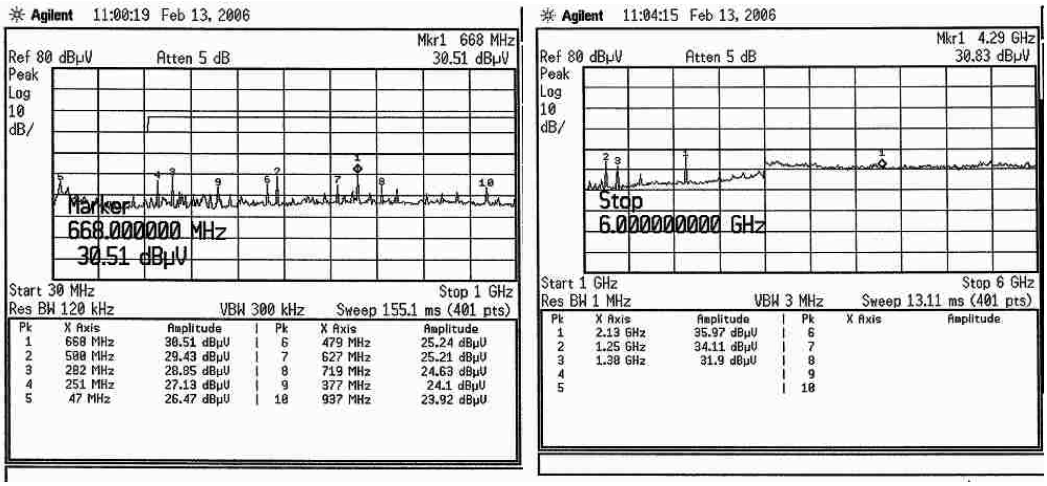

Figure 1.3. Measured Data for Baseline EMI Measurement – Cables Exits Bottom and Back Door Open

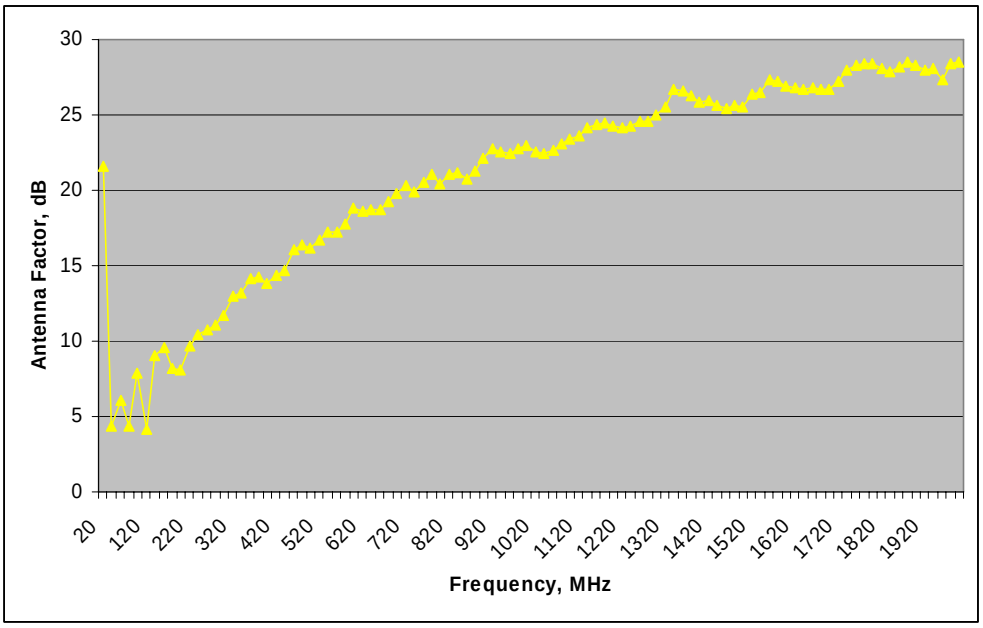

Figure 1.4. Antenna Factor Provided by NCR

Table 1.2. Data for the Baseline Measurement (Door Open and Cable Egress Bottom)

Frequency, MHz	Amplitude, dBµV/m (Vertically polarized Antenna)
47	31.174
251	37.695
282	40.016
377	38.31
479	25.24
500	45.56
627	43.84
668	49.464
719	44.91
937	46.51
1250	58.55
1380	58.22
2130	64.97

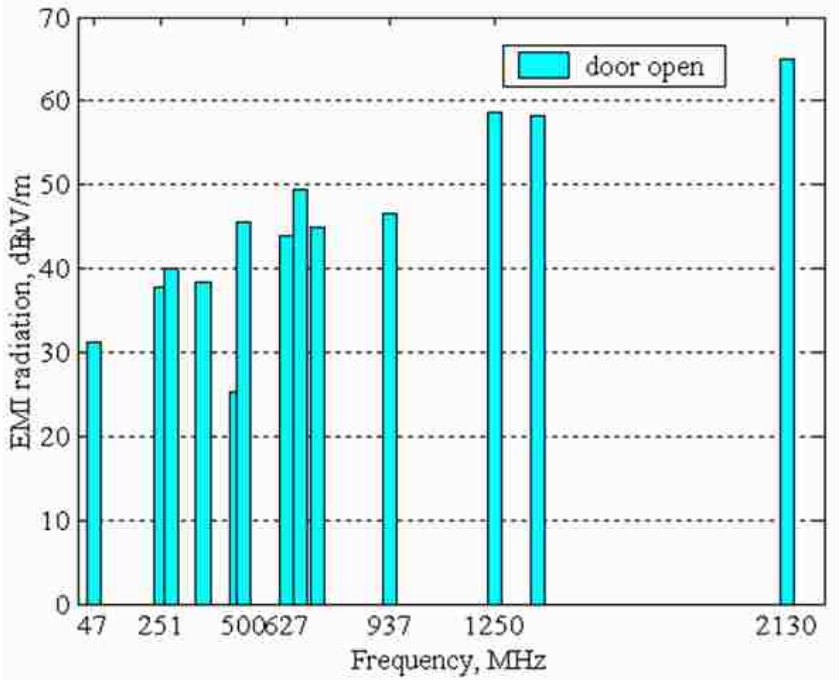

Figure 1.5. Baseline EMI Measurement of the Node Rack Cabinet with No BYNET Activity and Cable Exiting Bottom

Figure 1.6 and Figure 1.7 are the screen shots of the EMI measurement data with the AWS controller on and connected to the node cabinet, and with normal traffic from the node to BYNET cabinet. The receiving antenna was in the vertical orientation and

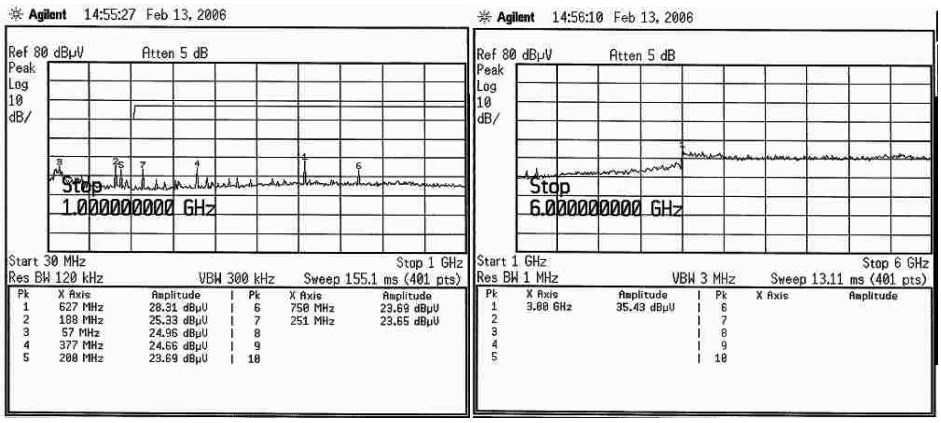

Figure 1.6. EMI Measurement Data – Cable Egress Bottom, Door Closed and Vertically Polarized Antenna

horizontal orientation respectively with regard to the chamber ground plane. The cable egress was at the bottom of the node rack cabinet. The data from these screen shots is tabulated in Table 1.3.

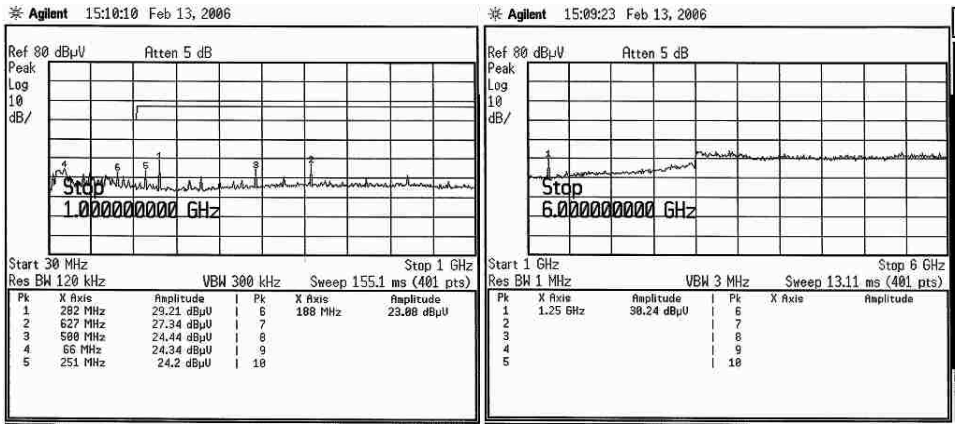

Figure 1.7. EMI Measurement Data – Cable Egress Bottom, Door Closed and Horizontally Polarized Antenna

Table 1.3. EMI Measurement Data – Cable Egress Bottom and Back Door Closed

Frequency (MHz)	Amplitude (dB µV/m) (Antenna – vertical polarization)	Amplitude (dBµV/m) (Antenna – horizontal polarization)
57	30.75	
66		29.88
188	33.47	32.02
200	31.8	
251	34.17	34.72
282		40.33
377	38.88	
500		40.57
627	46.94	45.97
750	43.885	
1250		54.68

Figure 1.8 and Figure 1.9 are the screen shots of the EMI measurement data with the same measurement setups except that the back door of the node rack cabinet was open. The data from these screen shots is tabulated in Table 1.4.

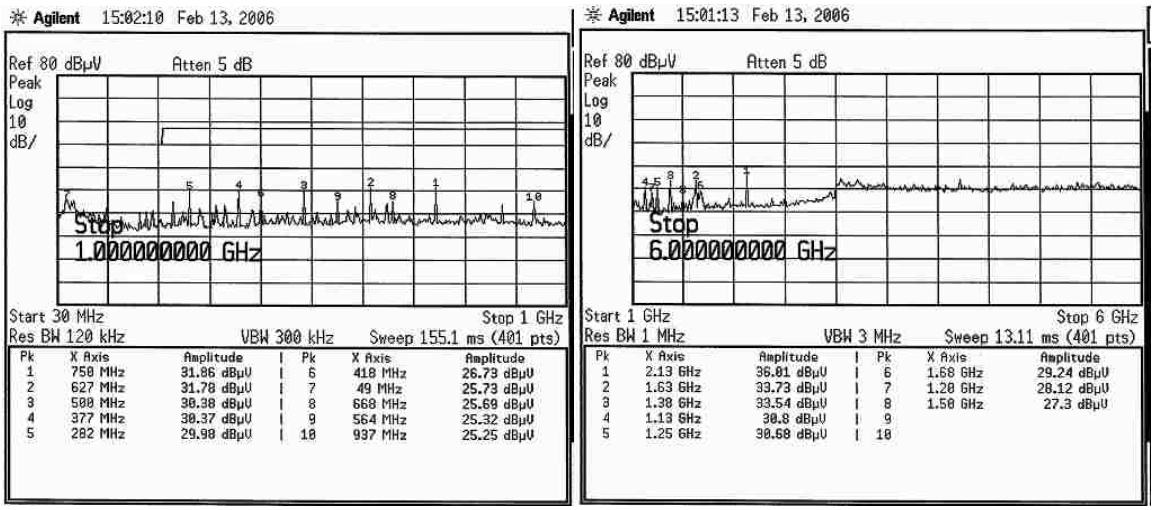

Figure 1.8. EMI Measurement Data – Cable Egress Bottom, Door Open and Vertically Polarized Antenna

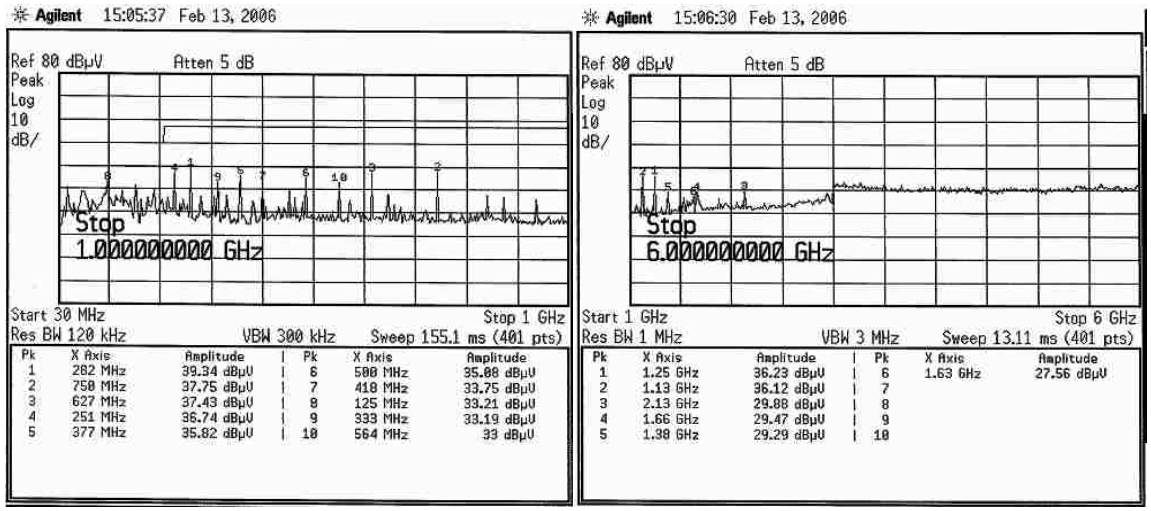

Figure 1.9. EMI Measurement Data – Cable Egress Bottom, Door Open and Horizontally Polarized Antenna

Table 1.4. EMI Measurement Data – Cable Egress Bottom and Back Door Open

Frequency (MHz)	Amplitude (dB μV/m) (Antenna – vertical polarization)	Amplitude (dBμV/m) (Antenna – horizontal polarization)
49	30.935	
125		38.56
188	33.47	
251	34.17	46.26
282	41.1	50.46
377	44.59	50.04
418	41.02	48.04
500	46.51	51.21
564	42.64	50.32
627	50.41	56.06
668	44.644	
750	52.055	57.945
937	47.84	
1130	54.7	60.02
1200	52.5	
1250	55.12	60.67
1380	59.72	65.61
1500	52.86	20.56
1630	60.49	54.32
1660		56.25
1680	55.95	
2130	65.01	58.88

Figure 1.10 is the comparison of the tabulated measured frequencies in the frequency range of 30 MHz – 6 GHz. For each frequency that has differing measured amplitudes corresponding to different antenna polarization, the maximum value is picked and plotted. It is seen that there is a general increase in the EMI of 5-10 dBμV/m in the low-frequency range when the rack cabinet doors are open. In the high-frequency range,

there is little detectable radiation above the noise floor at 20 dBμV/m with the cabinet doors closed. However, when the doors are open, there is an increase of again, 5-10 dBμV/m at eight frequencies. At the BYNET frequency of 627 MHz and the second harmonic at 1254 MHz, the increase is about 11 dBμV/m and 6 dBμV/m respectively. These frequencies correspond to the common-mode current on the outer shields of the BYNET cables. Overall, the cabinet rack provides additional shielding effectiveness of up to 10 dBμV/m, though it is not intentionally designed with shielding effectiveness in mind. This is consistent with previous measurements and assessments [2].

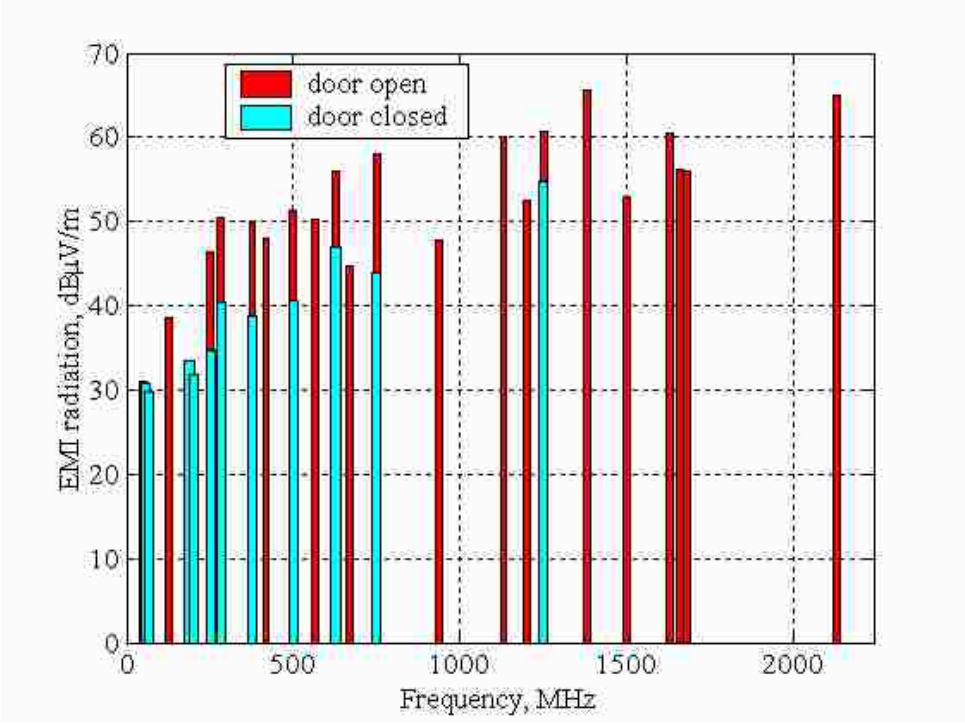

Figure 1.10. Comparison of EMI for Cabinet Rack Doors Open and Closed with Cables Exiting Bottom

Figure 1.11 and Figure 1.12 are the screen shots of the data of the EMI measurement with the AWS controller on and connected, normal traffic to BYNET cabinet, BYNET Cables Fed into the top of the BYNET cabinet, back doors

closed and the antenna was at 2 m height and in the vertical orientation and horizontal orientation respectively with regard to the chamber ground plane. Figure 1.13 shows the node rack cabinets' doors were closed and the cable egress was changed from bottom to

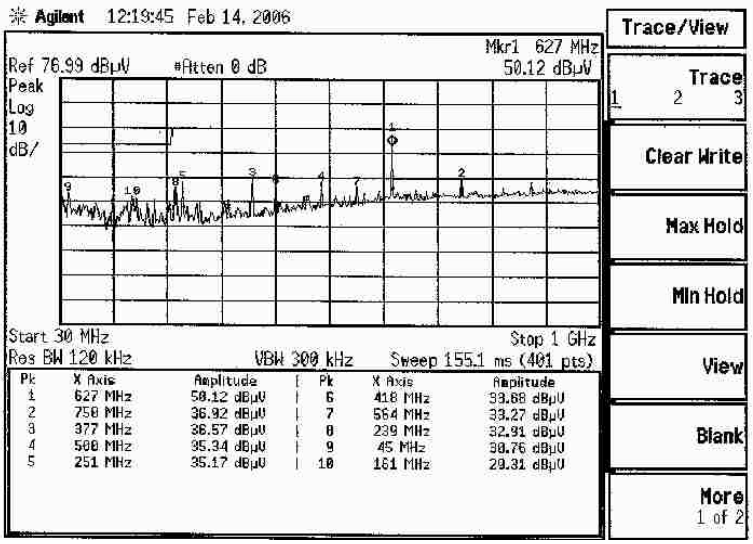

Figure 1.11. Measured EMI – Cables Egressing from the Top of the Node Cabinet and Vertical Antenna Polarization

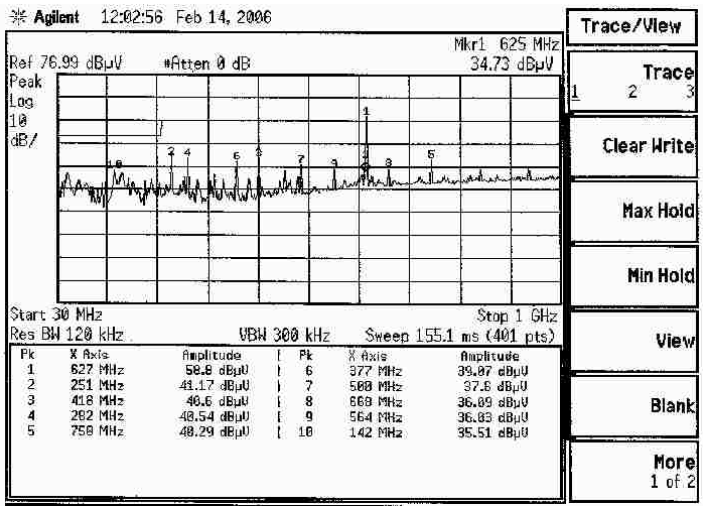

Figure 1.12. Measured EMI – Cables Egressing from the Top of the Node Cabinet and Horizontal Antenna Polarization

top. The data from these screen shots is adjusted and tabulated in Table 1.5. The measurements for the frequency range from 30 MHz – 1 GHz are shown in Figure 1.14. Of particular note in this case is the 627 MHz fundamental of the BYNET data stream. The measured radiation of 72 dBμV/m exceeds the FCC 3 m regulatory limit of 47 dBμV/m by nearly 25 dB for this configuration. Testing was done for the cables egressing from the top with only the cabinet doors closed.

Figure 1.13. Cabinet Rack with the Cable Harness Egressing From the Top

Table 1.5. EMI Measurement Data – Cable Egress Top and Doors Closed

Frequency (MHz)	Amplitude (dBμV/m) (Antenna – vertical polarization)	Amplitude (dBμV/m) (Antenna – horizontal polarization)
45	30.464	
142		39.608
161	33.93	
239	38.33	
251	40.735	46.735
282		46.706
377	45.78	48.28
418	42.97	49.89
500	46.47	48.73
564	45.59	48.35
627	63.75	72.43
668		50.044
750	52.115	55.485

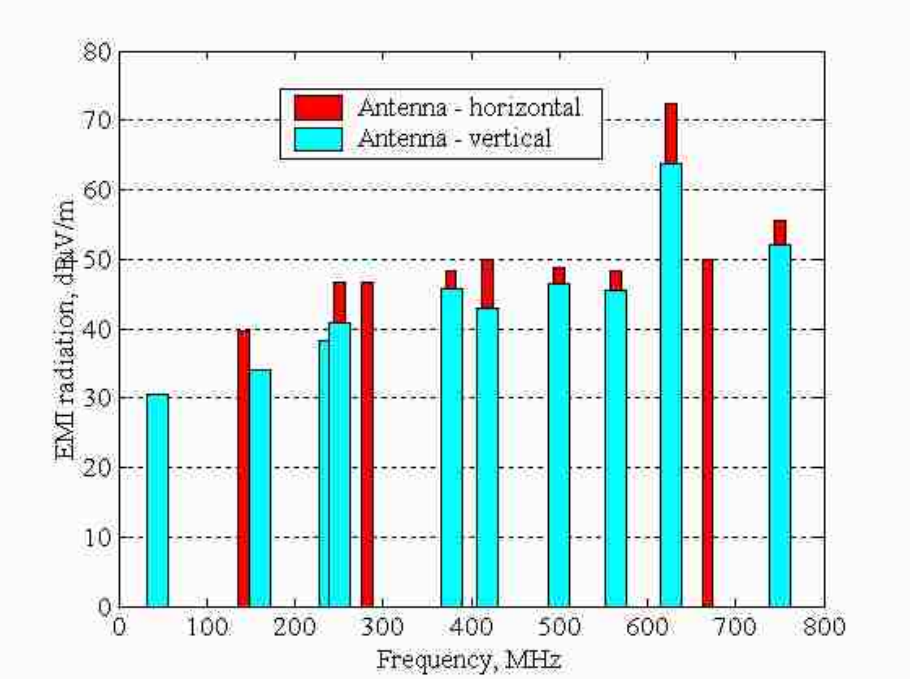

Figure 1.14. Comparison of the Measured EMI for Vertical and Horizontal Antenna Polarizations – Cables Egressing From Top of Node Cabinet

Figure 1.15 shows the comparison of the EMI measurements for cables egressing from the top of the node rack cabinet and cables egressing from the bottom of the cabinet in the frequency range of 30 MHz – 1 GHz. The cabinet doors were closed. For the frequencies that have different value of amplitude corresponding to the different antenna polarization, only the maximum value is plotted. It is observed that at most frequencies, when cables exit the top of the node rack cabinet, the measured radiation is much higher than that when cables egress from the bottom of the cabinet, especially at the clock frequency of 627 MHz, the difference reaches 25 dBμV/m.

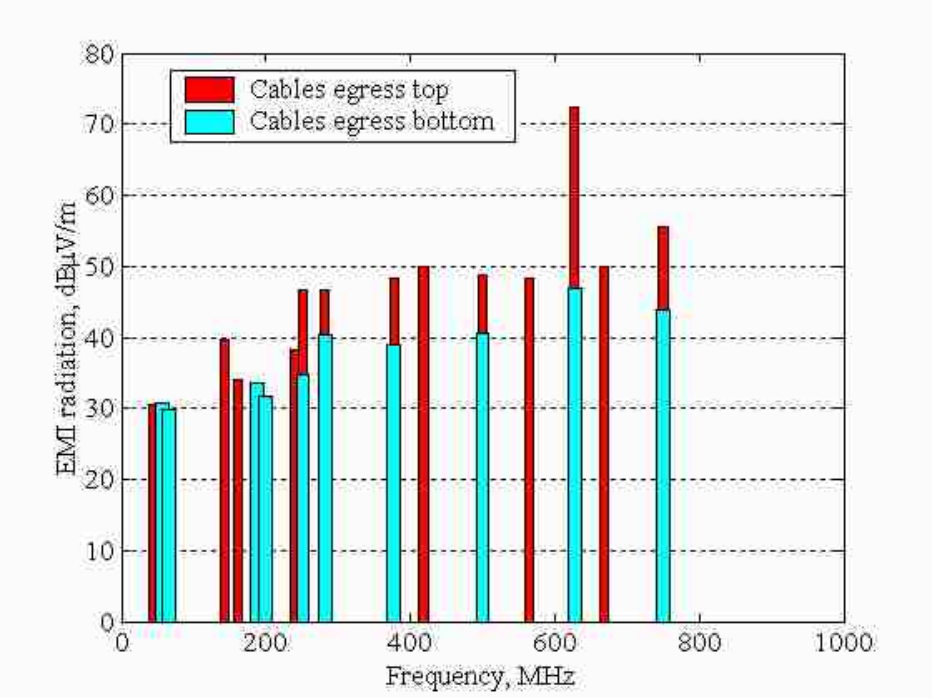

Figure 1.15. Comparison of Measured EMI for Cables Exiting Top and exiting Bottom of Node Rack Cabinet

1.4. CONCLUSION

The measurements on the NCR node rack equipment focused on two aspects of the configuration in particular: 1) the additional shielding effectiveness provided by the

equipment rack; and, 2) the EMI potential risk associated with the cables egressing from the top of the equipment, as opposed to through the bottom of the rack and to the conducting floor of the chamber. The measurements demonstrated an additional shielding effectiveness of 5-10 dBμV/m for the rack cabinet, even though it was not specifically for shielding purposes.

The cable egress from the top of the rack equipment resulted in EMI at the 627 MHz BYNET fundamental that was 30 dB higher than that with the cables exiting the bottom of the node rack cabinet, and exceeded the FCC regulatory limits by more than 20 dB. This is expected to present severe risk to EMI certification compliance if cables are allowed to egress from the top of the rack.

2. SWEPT FREQUENCY MEASUREMENTS AND STUDY

2.1. INTRODUCTION

The primary purpose of this study is to use swept frequency method to experimentally examine the EMI shielding effectiveness of the NCR node rack to determine the ramifications on electromagnetic interference/compatibility (EMI/EMC) regulatory compliance if cables egress from the top (roof) of the rack instead of the bottom, which is standard in today's products. Another purpose of this study is to apply various cabinet and cable egress setup combinations to the NCR node rack, measure the EMI shielding effectiveness, analyze and synthesis the measurement data for the optimization of the design of the node rack in the future.

As described in Chapter 1, the major source of high frequency EMI of the NCR node rack comes from the common-mode current on the cables, which is caused by the inherent imperfections of the connector, printed circuit boards, and cabling systems used in the equipment. Prior experimental surveys indicated that BYNET clock frequencies in the 627 MHz range are associated with the dominant radiated emissions due to cable egress [3].

In this study, an NCR node rack was mocked up using a Rittal 19-inch, 40U rack with doors and side panels (skins), populated with an empty node chassis and a simulated node cable. Swept frequency measurements for S-parameters were conducted in three ways using different measurement setups: spectrum analyzer (SA) setup, two-port vector network analyzer (VNA) setup and three-port VNA setup. After the convergence of the first two methods, the SA setup and the two-port VNA setup, was acquired, the S-parameters measurements of the node rack were done mainly using a method of three-port VNA.

This study confirms that, the rack cabinet, while not specifically engineered to be a superior EMI shielding enclosure, does, however, provide on the order of 10 dB of overall shielding effectiveness that is essential in meeting EMI regulatory requirements with the current system. From an EMI compliance standpoint, it is also shown that, with the current architecture of the cabinet's shielding, having cables exit the top of the node rack is very risky compared with having the cables exit the bottom of the rack.

It is worth mentioning that although a node rack was studied, the measurement setup is applicable to other rack types; thus the conclusions should apply to other types of racks (storage and BYNET) as well.

2.2. PCB DESIGN

To simulate the EMI problem in the real rack cabinet and measure the E field, A PCB, as shown in Figure 2.1, was used in the computer node to provide a differential current path for the signals.

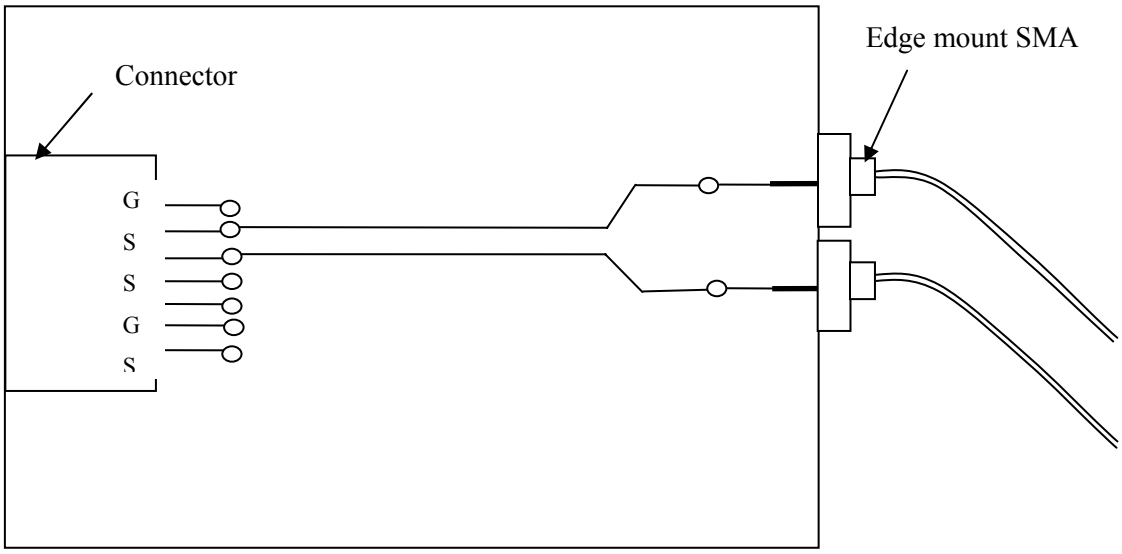

Figure 2.1. Schematic Plot of the 2-Layer PCB

By using HyperLynx the geometry of the traces is represented as shown in Figure 2.2. The differential impedance of the two traces on the PCB is designed as:

$$Z_{diff} = 2Z_0(1-k) \tag{1}$$

Let Z_{diff} = 100 Ohms, and assume the coupling coefficient is $k = 10\%$, then the impedance of a single trace is $Z_0 = 55.56\Omega$. The real PCB made is shown in Figure 2.3.

The actual impedance of each trace on the PCB is measured using a TDR, as indicated in Figure 2.4. The measurement results along the traces, as in Figure 2.5, clearly show the impedance of each single trace is around the design value 55.56 Ohms, with a variance of no more than 1 Ohm.

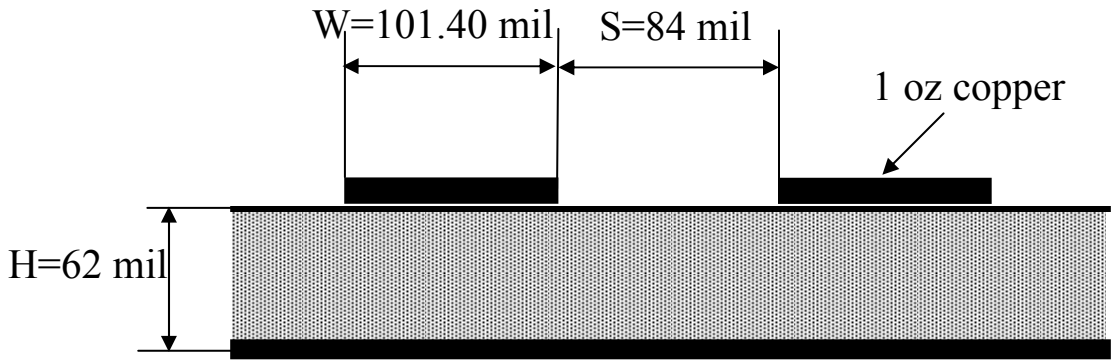

Figure 2.2. Geometry of the Differential Signal Traces

Figure 2.3. 2-Layer PCB with Differential Signal Traces and with Connectors Mounted

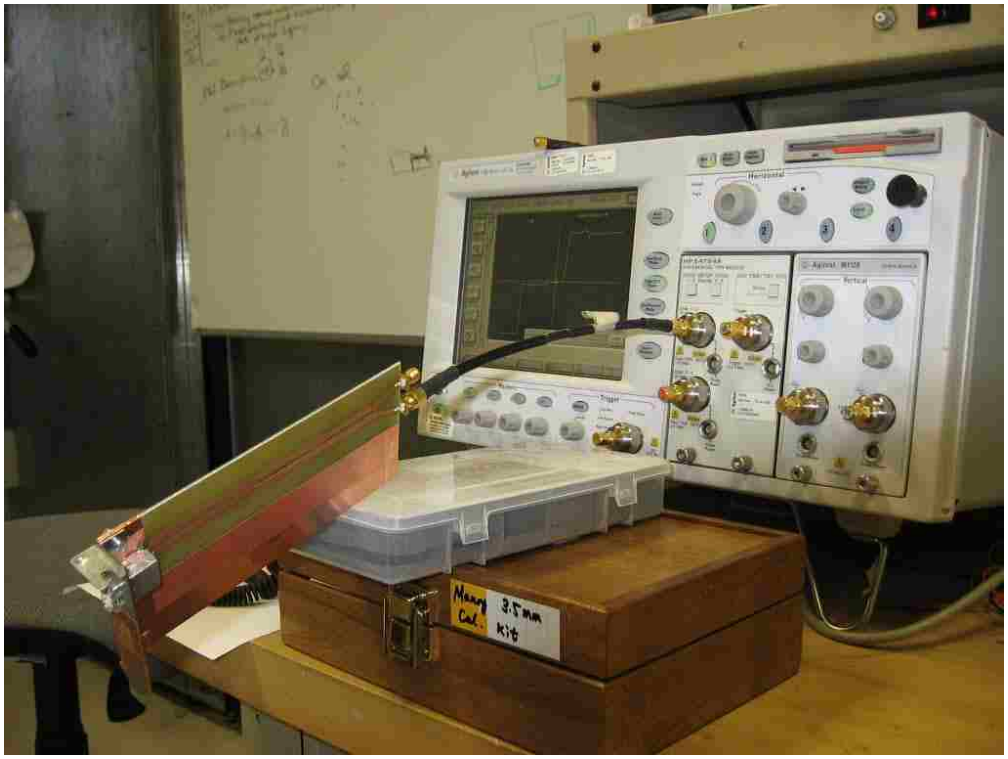

Figure 2.4. TDR Test Setup for Single Trace on the PCB

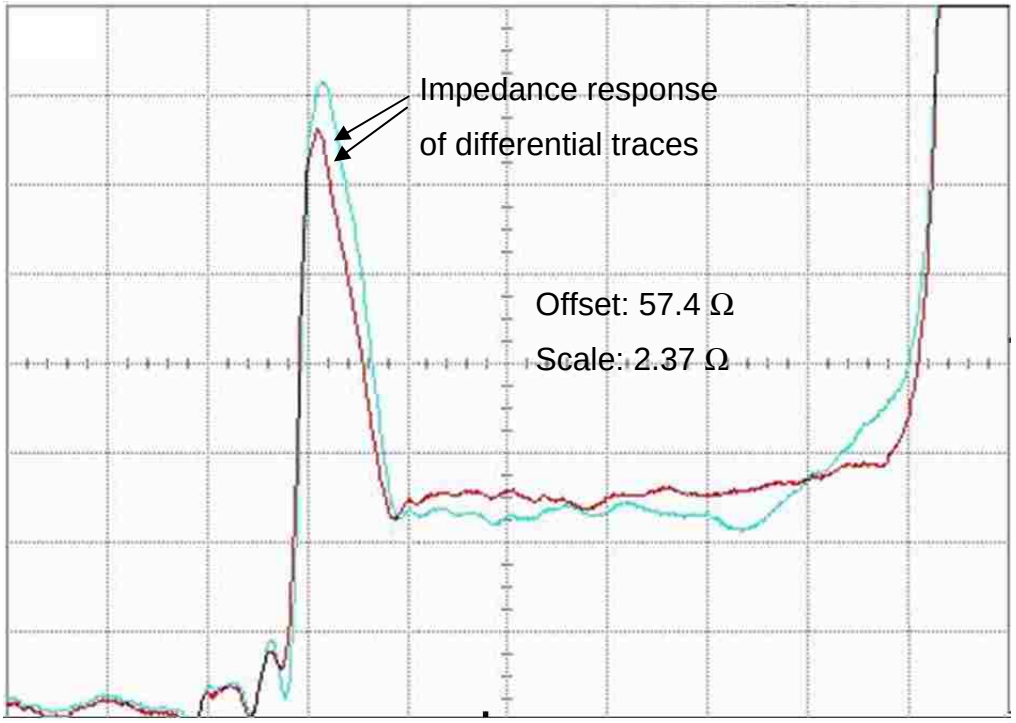

Figure 2.5. TDR Measurement Results of Impedance of the Differential Traces on PCB

2.3. MEASUREMENT SETUP

The equipment under test (EUT), the rack cabinet shipped from NCR, was staged in the UMR EMC Lab's 3-m semi-anechoic chamber, as seen in Figure 2.6. The EUT is a passive unit as it contains no power source and only a single computer node chassis. Polystyrene foam boxes wrapped with aluminum foil are used as the electromagnetic substitutions for the computer nodes normally in an operational node rack. The PCB with two differential signal traces, as designed in Section 2.2, was put into the computer node, shown in Figure 2.7, to provide a differential current path for the signals coming from the hybrid in the SA setup or coming from the vector network analyzer in the methods of two-port VNA setup and three-port VNA setup. The excitation sources, shown in Figure 2.8, are the twisted wires that connect to the ends of the differential signal traces and exit the computer module at the back of the cabinet.

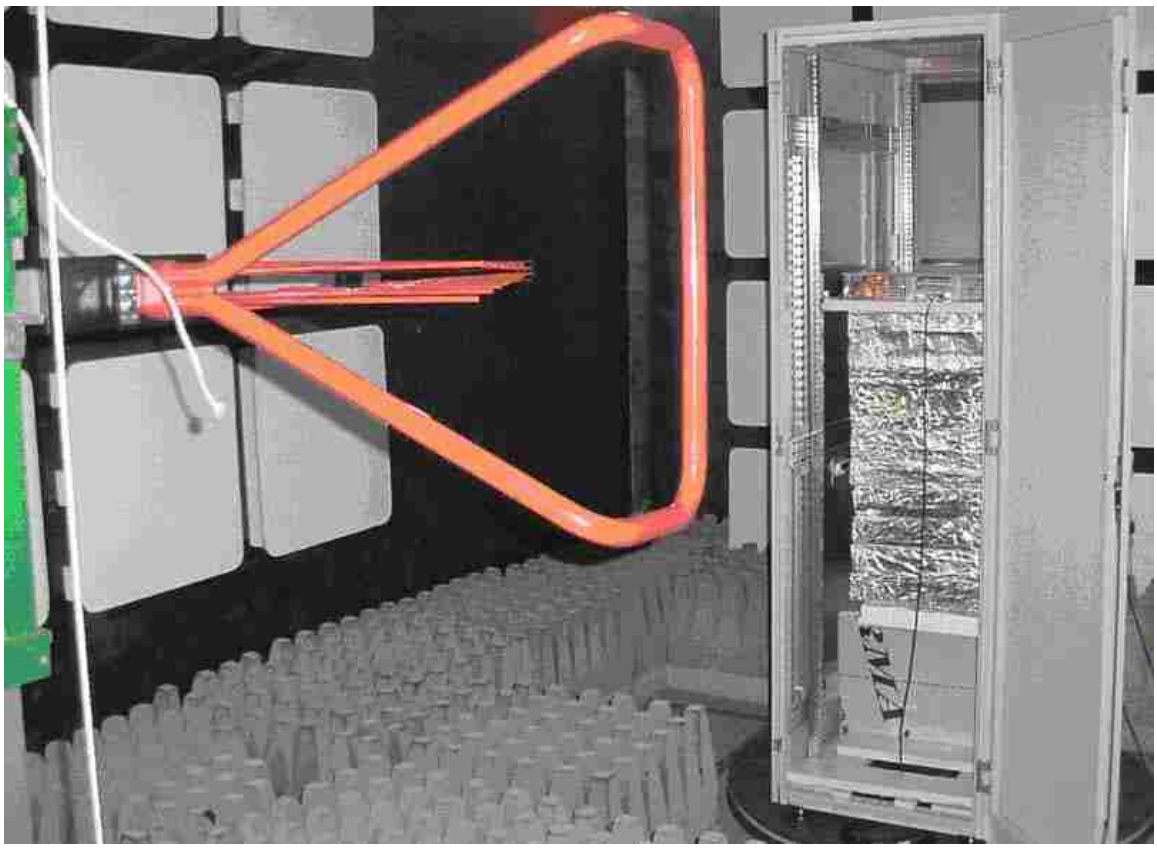

Figure 2.6. Cabinet Setup in the UMR EMC Lab's 3-m Semi-Anechoic Chamber

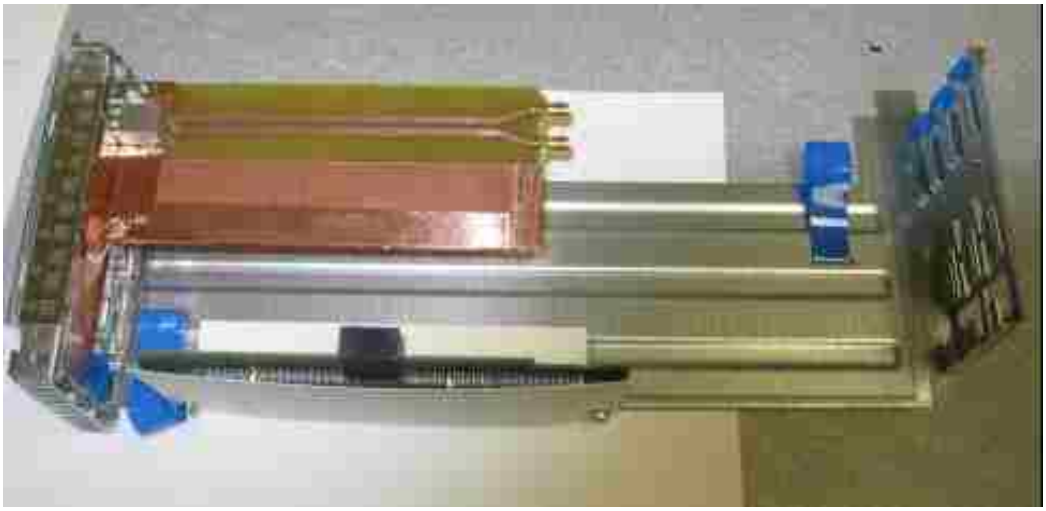

Figure 2.7. The PCB Inserted into a Slot of a Module in the Computer Node

Figure 2.8. Two Twisted Wires as the Radiation Source in the S-parameter Measurements

2.3.1. Spectrum Analyzer (SA) Setup. The schematic measurement setup is shown in Figure 2.9. The signal generator used is HP 8530 Sweep Oscillator. The swept signal has the frequency range of 100 MHz to 2 GHz, with the sweep time at 0.01s and power level at 5 dBm. The spectrum analyzer used is Rhode and Schwarz FSEB (20 Hz to 7 GHz). Figure 2.10 shows the two devices. The hybrid was set up in the rack cabinet

as in Figure 2.11 and Figure 2.12 is a close view of the hybrid. It has the outputs of either common mode voltage or differential mode voltage. When A is the input, C and D ports form differential outputs. When B is the input, C and D ports form common mode outputs. The measurement setup combinations are shown in Table 2.1. The power spectrum was measured by the antenna at the height of 1m and at the distance of 1.5 m from the cabinet's back door.

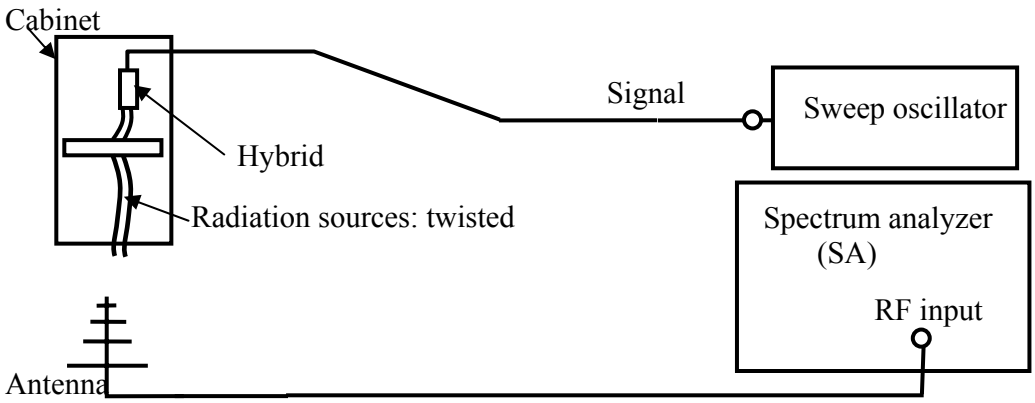

Figure 2.9. S21 Measurement Setup Using SA with Cables Exiting Bottom

Figure 2.10. Spectrum Analyzer and Sweep Oscillator for S_{21} Measurements of Cabinet

Figure 2.11. Hybrid Setup in Spectrum Analyzer or 2-port VNA Measurements

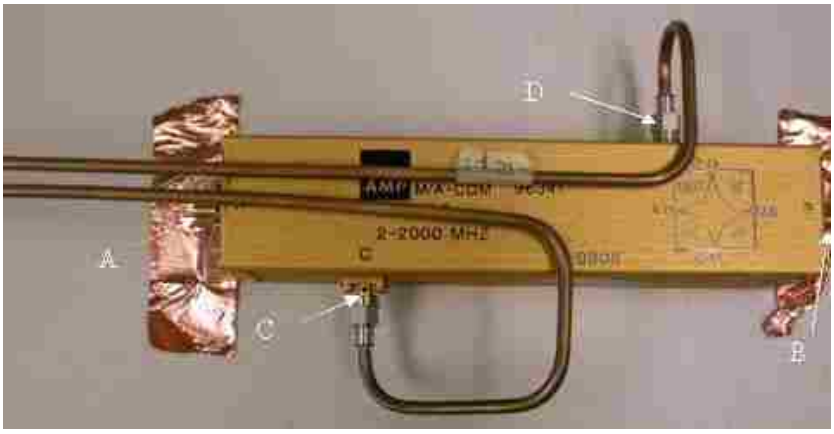

Figure 2.12. Close View of Hybrid

Table 2.1. Cabinet Setups and Antenna Polarization Setups

CABINET SETUP \ ANTENNA	HORIZONTAL	VERTICAL
▪ Back door open ▪ Differential mode currents from hybrid	✓	✓
▪ Back door closed ▪ Differential mode currents from hybrid	✓	✓
▪ Back door open ▪ Common mode currents from hybrid	✓	✓
▪ Back door closed ▪ Common mode currents from hybrid	✓	✓

The measured power should assume the same shape of the S_{21} curve only with a difference in amplitude. S_{21} can be approximately found through its definition,

$$S_{21} = \frac{V^-}{V^+} = \frac{V_{measured}}{V_{signal}} = \frac{\sqrt{P_{measured} \cdot 50\Omega}}{\sqrt{P_{signal} \cdot 50\Omega}} = \frac{\sqrt{P_{measured}}}{\sqrt{P_{signal}}} \tag{2}$$

and the S_{21} in dB can be calculated as

$$S_{21}(\text{dB}) = P_{measured}(\text{dBm}) - P_{signal}(\text{dBm}) + Cable\_loss(\text{dB}) \tag{3}$$

where $P_{measured}$ and P_{signal} are power in watts. $P_{signal}(\text{dBm})$ is 5 dBm and the C*able_loss* is measured by VNA. With antenna factor AF known, the electric field E is

$$E(\text{dBV/m}) = S_{21}(\text{dB}) + AF(\text{dB}) \tag{4}$$

2.3.2. Two-Port VNA Setup. The schematic two-port VNA measurement setup is shown in Figure 2.13. The VNA used is HP 8753D (30 kHz to 6 GHz). The output power of the signal is 5 dBm. The hybrid setup is the same as that in Section 2.3.1 and its outputs are either in common mode or in differential mode. The distance of the antenna to the cabinet door is 1.5 m. The two-port VNA measurements are done using the same rack cabinet and antenna setup combinations as in Table 2.1. The electric field E can be acquired based on the measured S_{21} using Equation (4).

2.3.3. Three-Port VNA Setup for Mixed-Mode S-parameter Measurement. A schematic of the three-port VNA measurement setup for mixed-mode S-parameter measurement is shown in Figure 2.14, which represents the test setup when cables exit the bottom of the cabinet. Absorbing floor tiles are used to absorb waves reflected by the ground. Figure 2.14 shows the complete current path in the measurement setup. When cables egress from the top of the rack, they must make their way back to the floor in order to connect to power and other connections. This is dictated by test configurations

possible at an Open Air Test Site (OATS). An OATS has no facility for cables to egress the test volume other than through the center of the turntable floor. OATS power to the rack comes from beneath the turntable and most other connections require cables to reach the floor. Figure 2.15 and 2.16 show the test setup when cables exit the top of the cabinet.

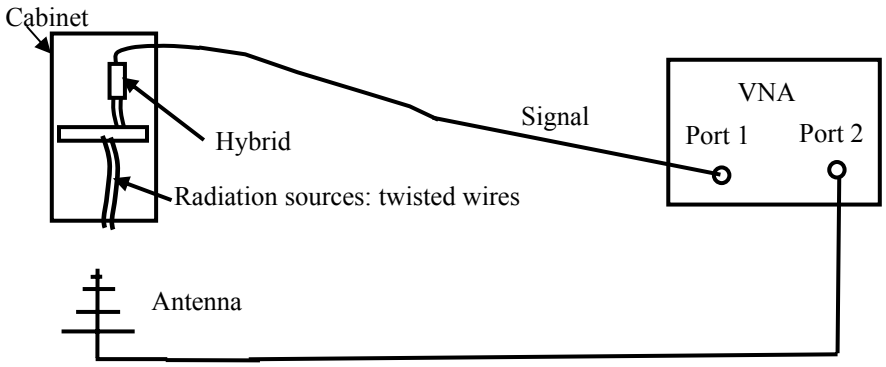

Figure 2.13. Two-Port VNA Setup for S_{21} Measurement of NCR's Rack Cabinet

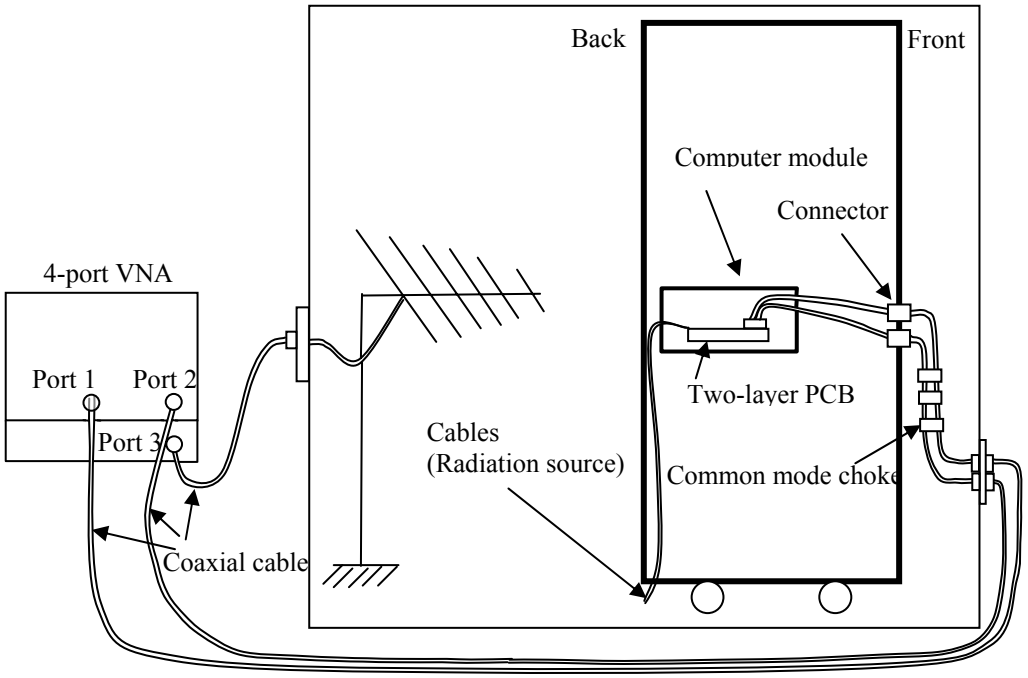

Figure 2.14. Schematic Representation of the Three-Port Mixed-Mode S-Parameter Measurement Setup for Cables Exiting the Bottom of Cabinet

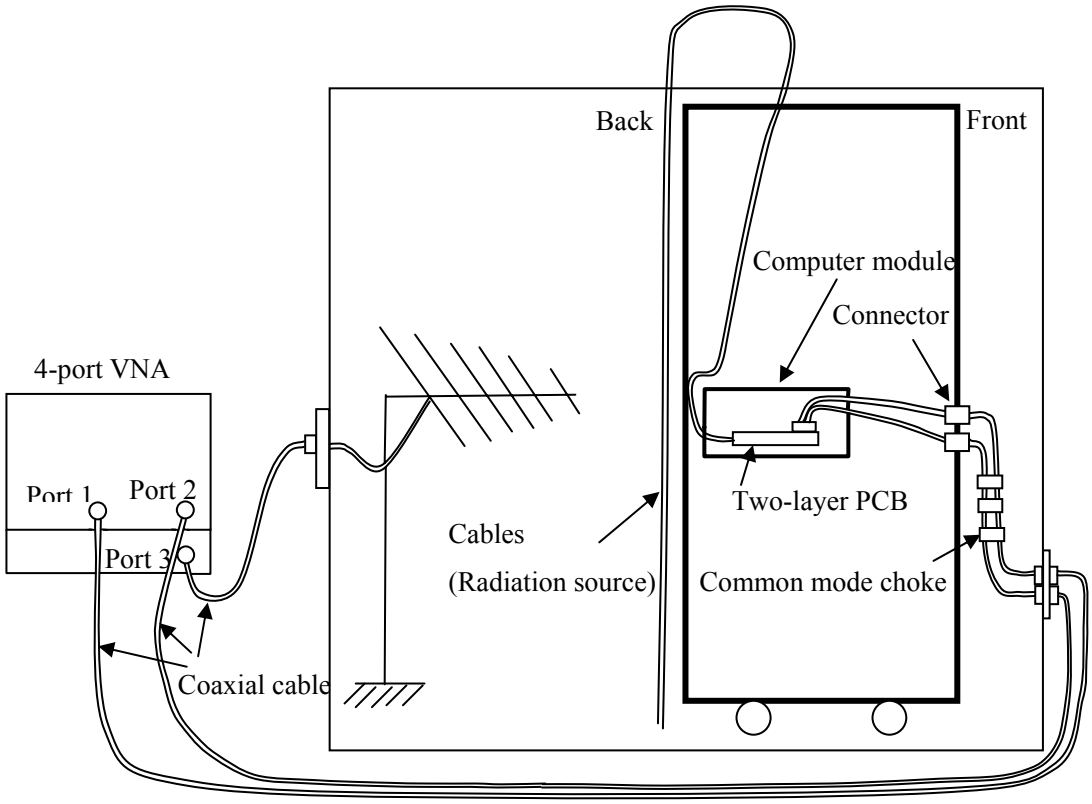

Figure 2.15. Schematic Representation of Three-Port Mixed-Mode S-Parameter Measurement Setup for Cables Exiting the Top of Cabinet

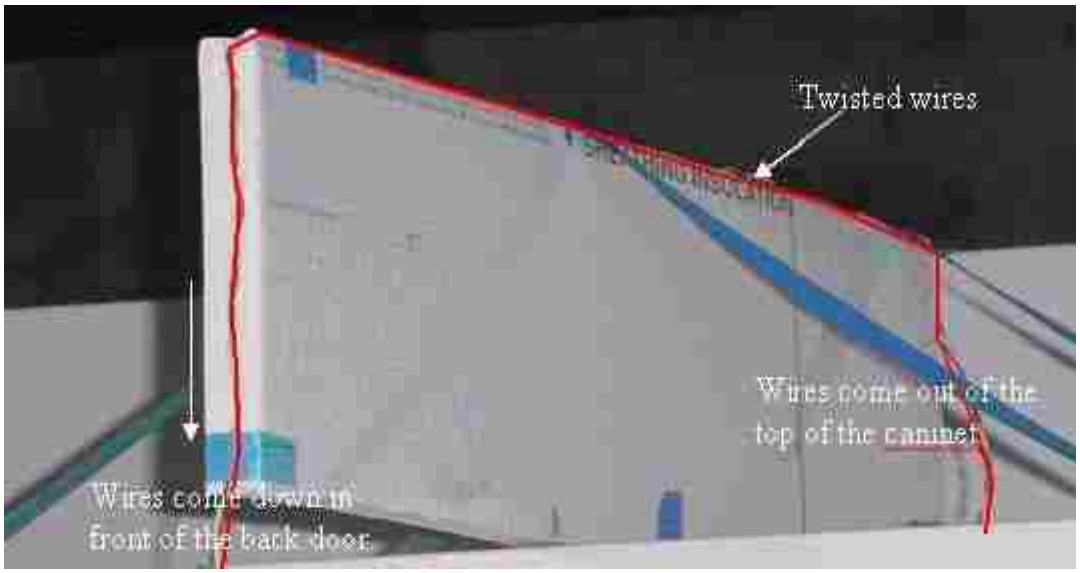

Figure 2.16. Two Twisted Wires Exiting the Top of Cabinet

The antenna was set at a distance of 1.5 m away from the back door of the rack cabinet. To obtain the maximum electric field, the antenna was oriented to measure vertical and horizontal polarizations at four different heights. Table 2.32 shows the antenna setups for each measurement. The antenna height was allowed to vary from 61 cm to 170 cm, except in the case of vertical polarization where the size of the antenna elements prohibited measurements at 61 cm from the floor.

Table 2.32. Various Antenna Heights and Polarizations for Each Cabinet Setup

Polarization / Height	HORIZONTAL	VERTICAL
61 cm	√	×
100 cm	√	√
135 cm	√	√
170 cm	√	√

A vector network analyzer, HP 8720ES (50 MHz to 20 GHz), was used for the three-port mixed-mode S-parameter measurement. The software used was Agilent Multiport version 1.38. The actual cabinet setup is shown in Figure 2.17, where ferrite floor tiles are used and twisted wires are used as the radiation source to intensify the electric field which would have been very weak if using the BYNET cable. The back door is not shown in the figure but measurements were performed with the back door on and closed. The three port mixed-mode S-parameter measurements were done for various cabinet setups described in Table 2.3. As described in Table 2.32, for each setup the measurements were done at different antenna heights and polarizations with the purpose of finding the maximum radiations.

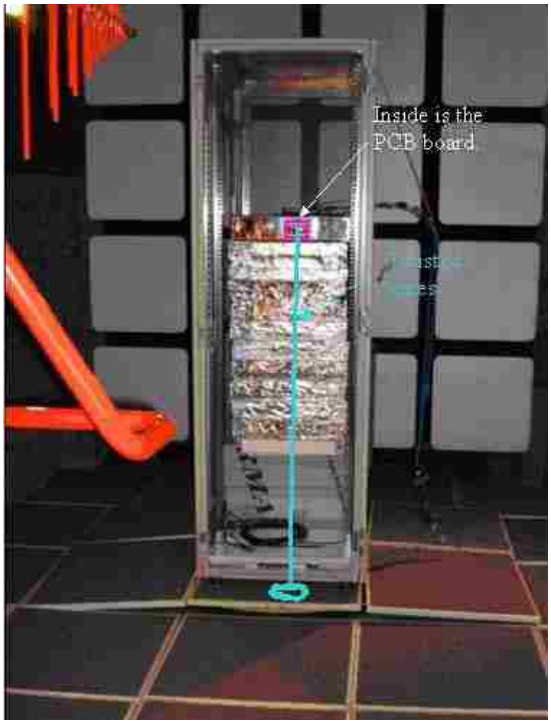

Figure 2.17. Cabinet Setup for Three-Port Mixed-Mode S-Parameter Measurements

Table 2.3. Cabinet Setups

Back door / Side panels / Cable exit	Door closed Panels on	Door off Panels on	Panels off Door closed	Panels off Door off
Bottom	√	√	√	√
Bottom Ferrite floor	√	√	√	√
Top	√	√	√	√
Top Ferrite floor	√	√	√	√
No twisted cables	√	√	√	√
No twisted cables Ferrite floor	√	√	√	√

To find the radiation caused by common-mode currents and differential-mode currents, the common mode S-parameter s_{21}^{Ac} ($s_{21}^{Ac} = \frac{v_3^-}{v_1^+ + v_2^+}$) and the differential mode S-parameter s_{21}^{Ad} ($s_{21}^{Ad} = \frac{v_3^-}{v_1^+ - v_2^+}$) need to be found from the measured unbalanced S-parameters. Using the method described in [4] and [5], the common- and differential-mode S-parameters are derived.

The three port unbalanced s-parameter matrix is defined in equation (5). The quantities b_1, b_2 and b_3 are the reflective scattering wave of port 1, port 2 and port 3 respectively; the quantities a_1, a_2 and a_3 are the incident wave of port 1, port 2 and port 3 respectively, as shown in Figure 2.18.

$$\begin{pmatrix} b_1 \\ b_2 \\ b_3 \end{pmatrix} = \begin{pmatrix} s_{11} & s_{12} & s_{13} \\ s_{21} & s_{22} & s_{23} \\ s_{31} & s_{32} & s_{33} \end{pmatrix} \begin{pmatrix} a_1 \\ a_2 \\ a_3 \end{pmatrix} \equiv [s]_3 \begin{pmatrix} a_1 \\ a_2 \\ a_3 \end{pmatrix} \tag{5}$$

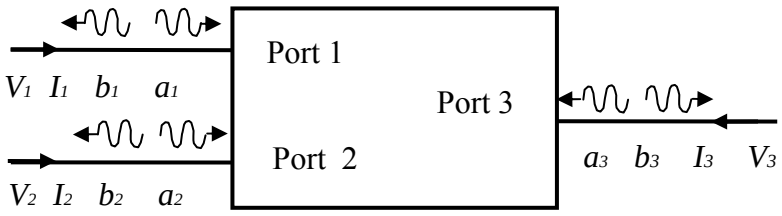

Figure 2.18. Nodal Scattering Wave Representation of a Three-Port Measurement

The three port mixed-mode s-parameter (complex) matrix is defined in Equation (6). Figure 2.18 shows the corresponding mixed-mode scattering wave representation of the three-port S-parameter measurement setup. P_A is the antenna port. ΔP_1 represents the signal ports, with one as the differential-mode port 1 (represented with upper script *d*)

and the other as the common-mode port 1 (represented by upper script *c*). The quantities b_1^d, b_2^A and b_1^c are the reflective mixed-mode scattering wave of differential port 1, antenna port 2 and common-mode port 1 respectively; a_1^d, a_2^A and a_1^c are the incident mixed-mode scattering wave of differential port 1, antenna port 2 and common-mode port 1 respectively.

$$\begin{pmatrix} b_1^d \\ b_2^A \\ b_1^c \end{pmatrix} = \begin{pmatrix} s_{11}^{dd} & s_{12}^{dA} & s_{11}^{dc} \\ s_{21}^{Ad} & s_{22}^{AA} & s_{21}^{Ac} \\ s_{11}^{cd} & s_{12}^{cA} & s_{11}^{cc} \end{pmatrix} \begin{pmatrix} a_1^d \\ a_2^A \\ a_1^c \end{pmatrix} \equiv [\Delta s]_3 \begin{pmatrix} a_1^d \\ a_2^A \\ a_1^c \end{pmatrix} \tag{6}$$

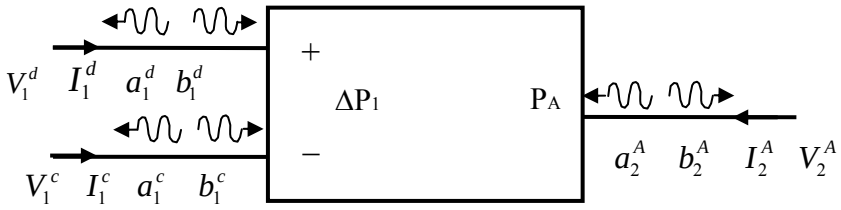

Figure 2.19. Mixed-Mode Scattering Wave Representation of Three-Port Setup

To find the mixed-mode S-parameters from the unbalanced S-parameters, the transformation matrix here is defined as

$$[m] = \frac{1}{\sqrt{2}} \begin{pmatrix} 1 & -1 & 0 \\ 0 & 0 & 1 \\ 1 & 1 & 0 \end{pmatrix} \tag{7}$$

and the mixed-mode s-parameter can be found as

$$[\Delta s]_3 = [m][s]_3[m]^{-1} = \frac{1}{2} \begin{pmatrix} s_{11}-s_{21}-s_{12}+s_{22} & 2(s_{13}-s_{23}) & s_{11}-s_{21}+s_{12}-s_{22} \\ s_{31}-s_{32} & 2s_{33} & s_{31}+s_{32} \\ s_{11}+s_{21}-s_{12}-s_{22} & 2(s_{13}+s_{23}) & s_{11}+s_{21}+s_{12}+s_{22} \end{pmatrix} \tag{8}$$

The differential mode S-parameters and the common-mode S-parameters then are characterized with Equation (9) and (10) respectively.

$$\begin{pmatrix} s_{11}^{dd} & s_{12}^{dA} \\ s_{21}^{Ad} & s_{22}^{AA} \end{pmatrix} = \begin{pmatrix} \frac{1}{2}\left(s_{11}-s_{21}-s_{12}+s_{22}\right) & s_{13}-s_{23} \\ \frac{1}{2}\left(s_{31}-s_{32}\right) & s_{33} \end{pmatrix} \tag{9}$$

$$\begin{pmatrix} s_{22}^{AA} & s_{21}^{Ac} \\ s_{12}^{cA} & s_{11}^{cc} \end{pmatrix} = \begin{pmatrix} s_{33} & \frac{1}{2}\left(s_{31}+s_{32}\right) \\ \left(s_{13}+s_{23}\right) & \frac{1}{2}\left(s_{11}+s_{21}+s_{12}+s_{22}\right) \end{pmatrix} \tag{10}$$

To find the radiation at the antenna, the electric field E_d caused by the differential-mode current and the electric field E_c caused by the common-mode current need to be found. From the differential-mode S-parameter s_{21}^{Ad} and the common-mode S-parameter s_{21}^{Ac}, with the antenna factor AF (in dB) considered for the unbalanced S-parameter term s_{31} and s_{32}, the magnitude of E_d and E_c (both in dBV/m) are

$$E_d = 20\log_{10}\left|\frac{1}{2}\left(s_{31}-s_{32}\right)\right| + AF \tag{11}$$

$$E_c = 20\log_{10}\left|\frac{1}{2}\left(s_{31}+s_{32}\right)\right| + AF \tag{12}$$

2.4. RESULTS AND DISCUSSION

There was some concern that the use of the hybrid would alter the fields normally emitted from the cabinet in the absence of the hybrid. Therefore, the purpose of performing the S-parameter measurements using the SA setup and two-port VNA setup was mainly to validate all three setup methods before using the third method, the three-port VNA for mixed-mode S-parameter measurements, to extensively investigate the shielding effectiveness of the rack cabinet.

2.4.1. Measurement Results for SA Setup and Two-Port VNA Setup.

Convergence of the first two methods, discussed in Section 2.3.1 and Section 2.3.2, is as expected for all cases of the cabinet setups described in Table 2.1 with the cables exiting the bottom. S_{21} is a measure of the electric field at the antenna, normalized so that it is independent of the input voltage to the PCB within the cabinet. A larger value of $|S_{21}|$ indicates a higher value of the radiated electric field for the same amount of the input voltage. With antenna factor known, as in Equation (4) or in Equations (11) and (12), the electric field E at antenna point is plotted, compared and discussed.

Figure 2.20 through Figure 2.23 show the electric field , over the frequency range of 100 MHz to 2 GHz at the antenna point (antenna height is 1 m) for various cabinet setups and with the twisted cables exiting the bottom of the cabinet. It is seen that the maximum |E| in dBV/m calculated from the measured power spectrum in the SA measurement setup, matches the result from the two-port VNA measurements very well. The match indicates that the same radiated emissions were measured by the two methods, which means that the measurement setups are valid. Figure 2.24 shows the cable loss of the whole path in the SA setup acquired by "through" (S21) measurement using VNA. Figure 2.25 is the antenna factor data provided by the manufacturer. Both were needed in the calculation of the |E|.

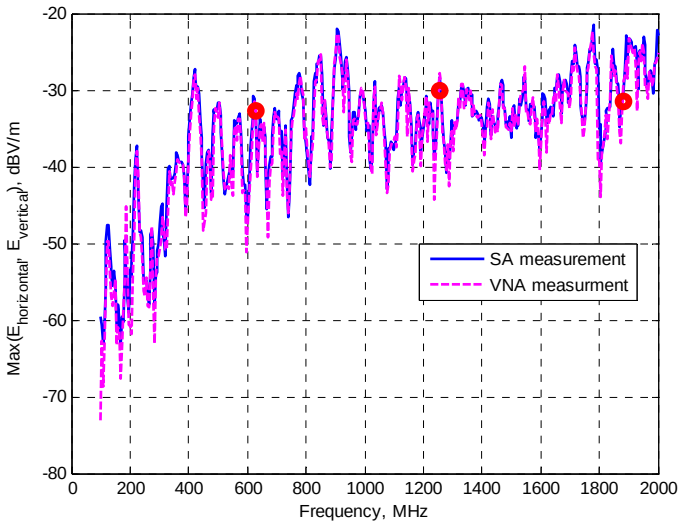

Figure 2.20. Radiated Emission for Differential-Mode Current with Cabinet Door Closed

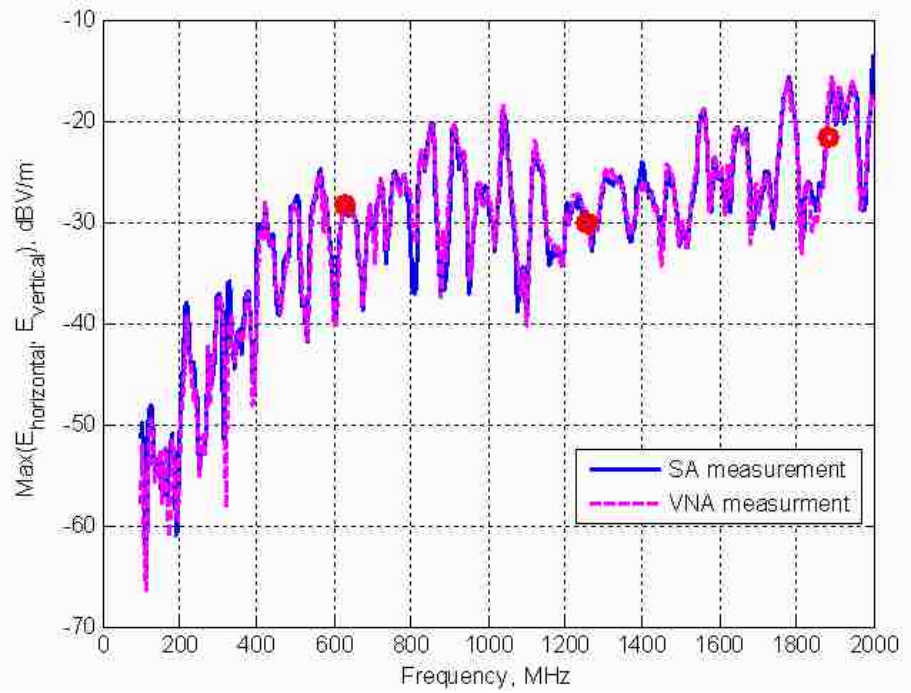

Figure 2.21. Radiated Emission for Differential-Mode Current with Cabinet Door Open

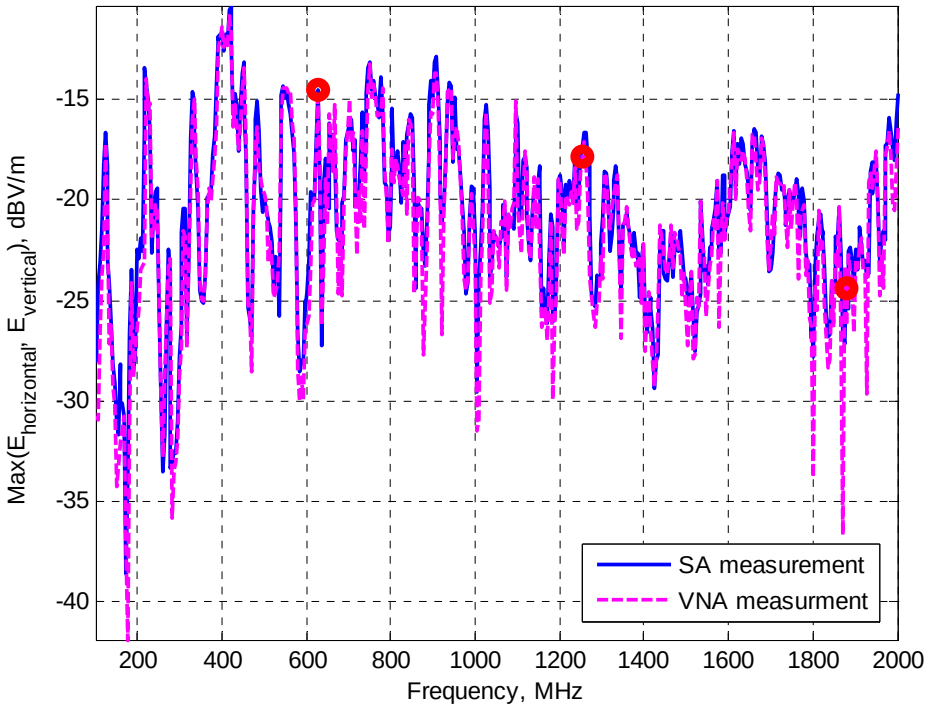

Figure 2.22. Radiated Emission for Common-Mode Current with Cabinet Door Closed

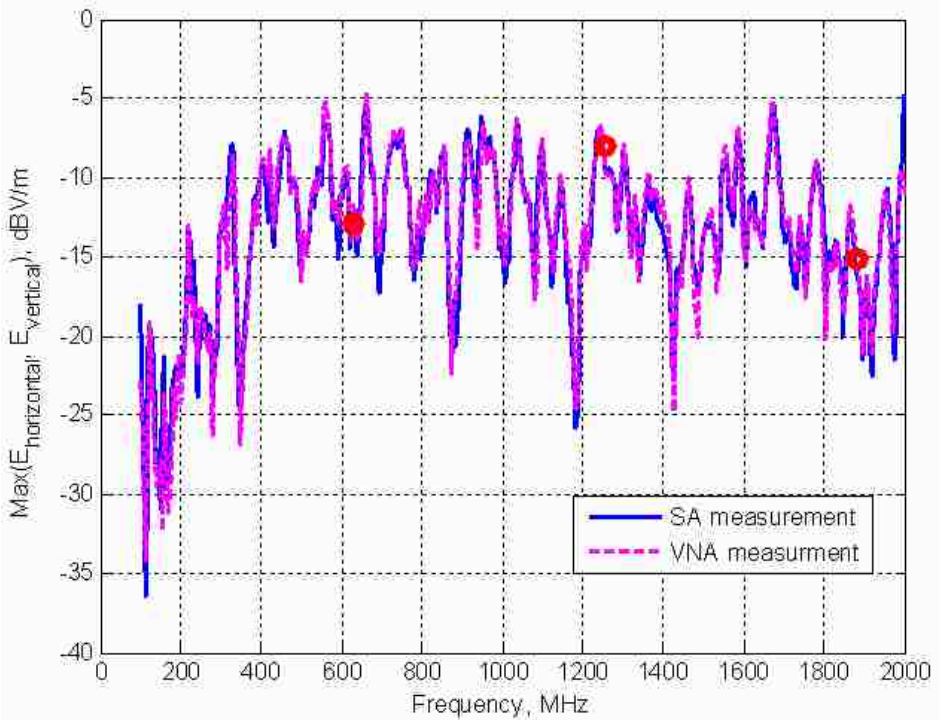

Figure 2.23. Radiated Emission for Common-Mode Current with Cabinet Door Open

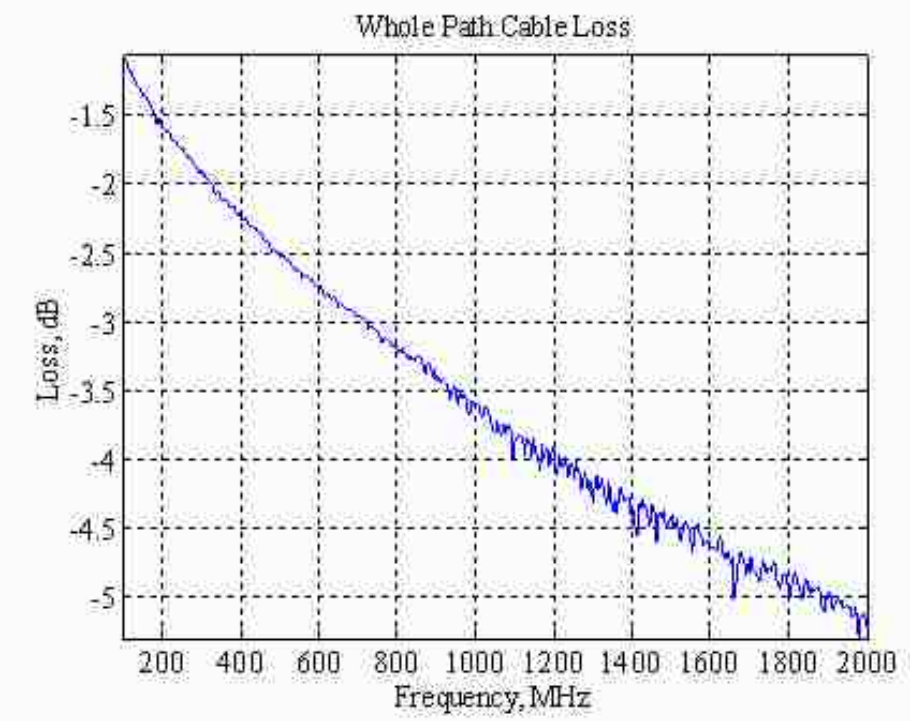

Figure 2.24. Measurement of Cable Loss in SA Measurement Setup

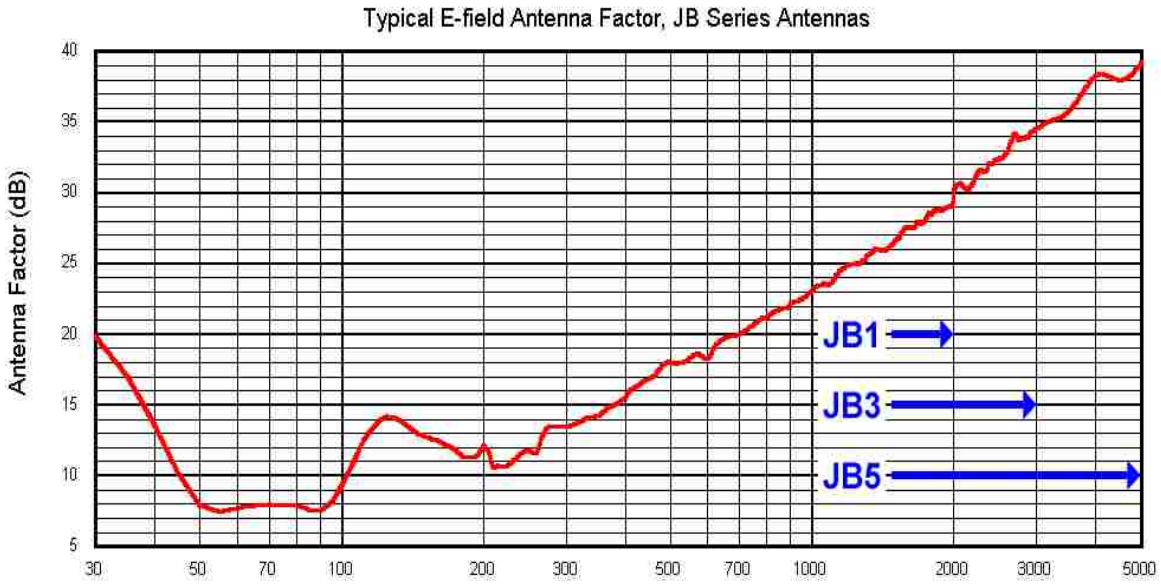

Figure 2.25. Antenna Factor (AF) of Sunol Sciences' JB Series Antennas from Sunol Sciences' Website

2.4.2. Measurement Results for Three-Port VNA Setup. To characterize the EMI Radiation from the cabinet, results of electric field |E| acquired from the measurements of three-port mixed-mode S-parameter for various cabinet setups are compared and discussed. The frequency range considered is 100 MHz to 2 GHz. At each frequency only the maximum values of |E| are considered for all antenna heights and polarizations. The cable attenuation was eliminated from the results through the three port calibration of the measurement.

2.4.2.1. Radiation source – common-mode currents. For most devices common-mode (CM) currents are a significant source of electromagnetic interference [6]. Results for $|E_c|$, the magnitude of the electric field determined from the common-mode measurement of S_{21}^{AC}, will be discussed based on the measured three-port unbalanced S-parameters using the three-port VNA setup discussed in Section 2.3.3

2.4.2.1.1. Cabinet on ground plane. Figure 2.26 shows the radiated emissions of the cabinet at the antenna point with the radiation sources, the twisted cables, exiting the top of the cabinet. Figure 2.27 shows the radiated emission of the cabinet with the similar

setting as in Figure 2.26 but with the twisted cables exiting the bottom. Both figures have plots of the maximum value of $|E_c|$ for all four cabinet setups – door closed and side panels on, door off and side panels on, side panels off and door closed and side panels off and door off in the frequency range of 100 MHz to 2 GHz. It is observed that, first, for all four cabinet setups, with cables exiting either top or bottom, the cabinet provides little shielding effectiveness (< 4 dBV/m) at lower frequencies and more shielding effectiveness (> 15 dBV/m) for higher frequencies; second, the antenna detected the overall strongest radiation only when the back door was taken off and detected the overall weakest radiation when the two side panels were taken off while the back door was kept closed. Even with the cabinet turned at 45 degree and 90 degree, as shown in Figure 2.28 and Figure 2.29, the radiation detected by the antenna with only side panels taken off is still weaker than that in the case of no back door for the cabinet setup. It may be explained that the side panels reflect waves in the cabinet. When only the back door was taken off while the side panels were kept on, all the radiation came out from the back door. But when side panels were also taken off, the radiation came out the cabinet in three directions, so the total radiation from the cabinet may have increased but the field detected at the antenna point was decreased.

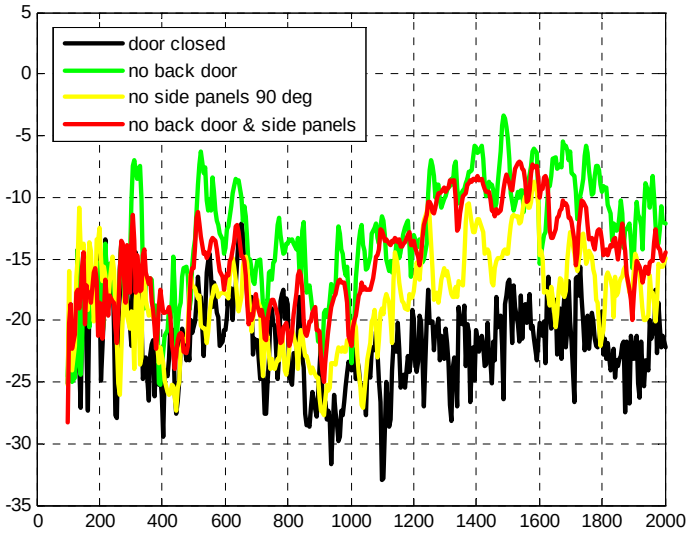

Figure 2.26. EMI Radiation by CM Current with Twisted Cables Exiting Top

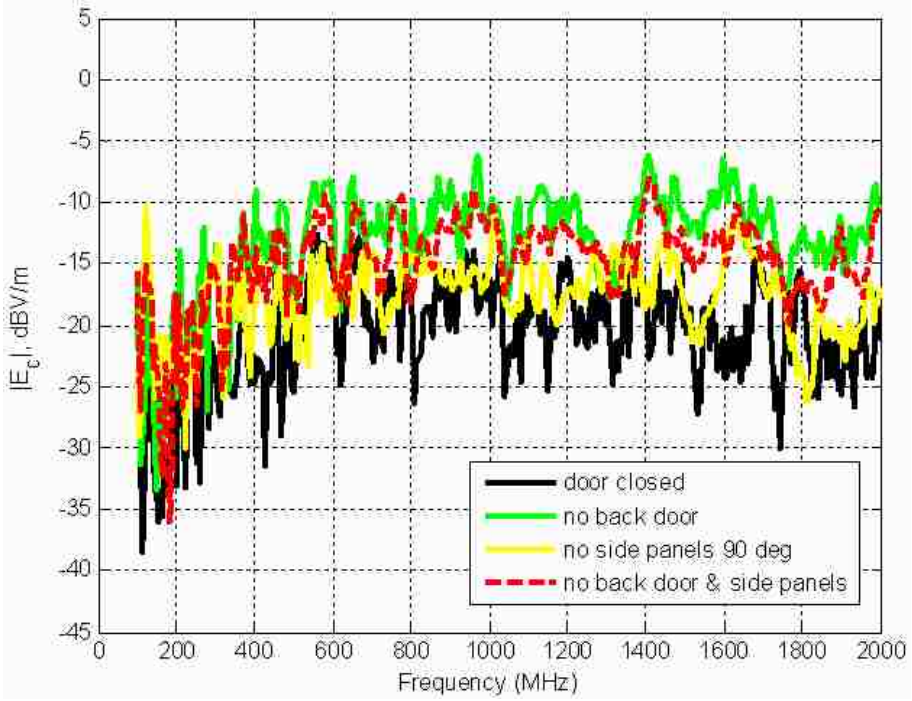

Figure 2.27. EMI Radiation by CM Current with Twisted Cables Exiting Bottom

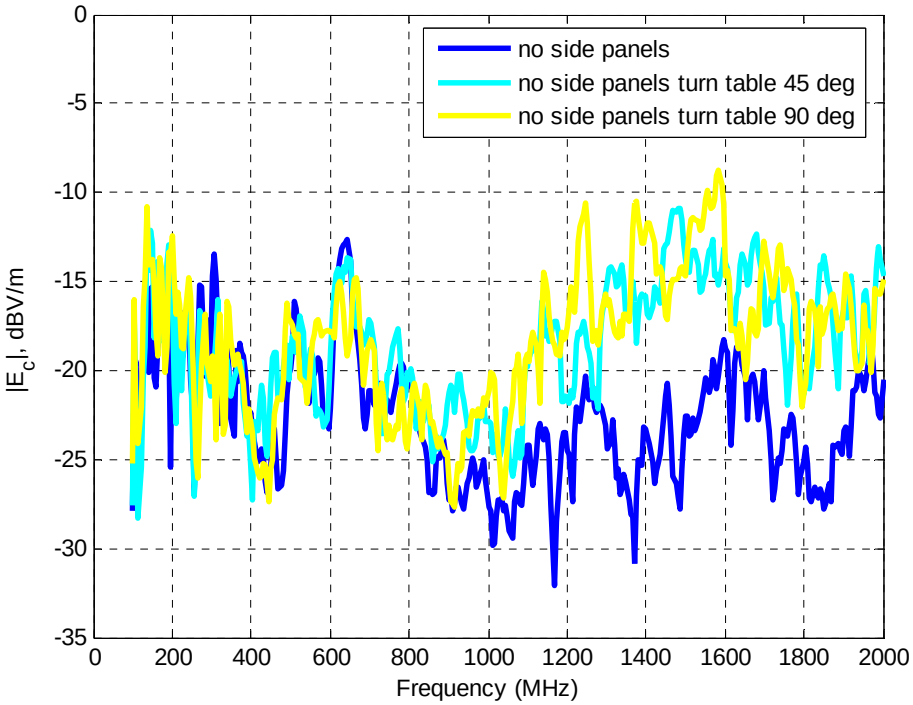

Figure 2.28. EMI Radiation by CM Current with Twisted Cables Exiting Top for Various Cabinet Side Panel Setups

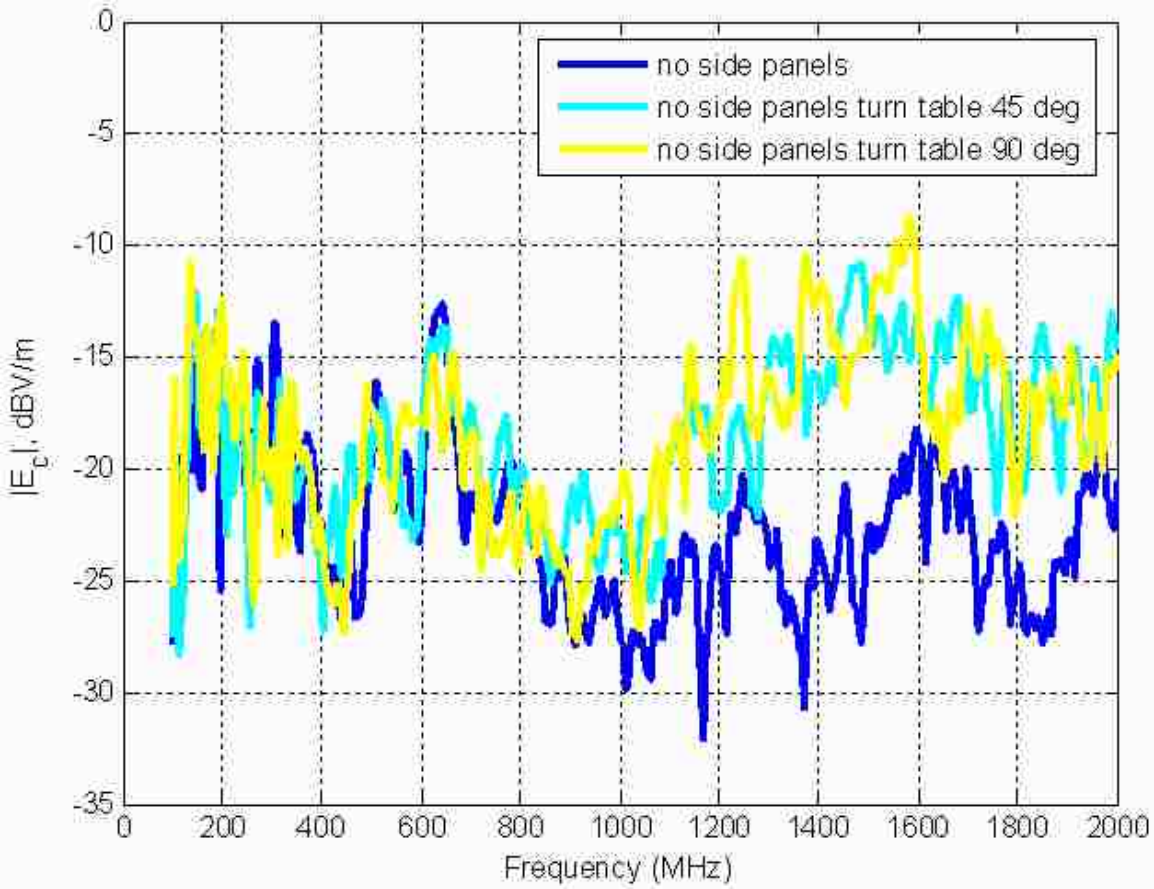

Figure 2.29. EMI Radiation by CM Current with Twisted Cables Exiting Bottom for Various Cabinet Side Panel Setups

One of the important objectives was to find out how the radiation varies with the change of the cable egress. A comparison was done for twisted cables exiting the top versus twisted cables exiting the bottom for each cabinet setup, Figure 2.30 and Figure 2.31show results for the cabinet back door closed, Figure 2.32 and Figure 2.33 for the cabinet back door taken off, Figure 2.34 and Figure 2.35 for the cabinet side panels taken off but the back door kept closed and Figure 2.36 and Figure 2.37 for both the cabinet side panels and the back door taken off. It is observed that there is no apparent trend existing for radiations of different cabinet setups. But at higher frequencies (> 1 GHz), for most frequency points the radiation is higher when cables exit the top of the cabinet than when cables exit the bottom.

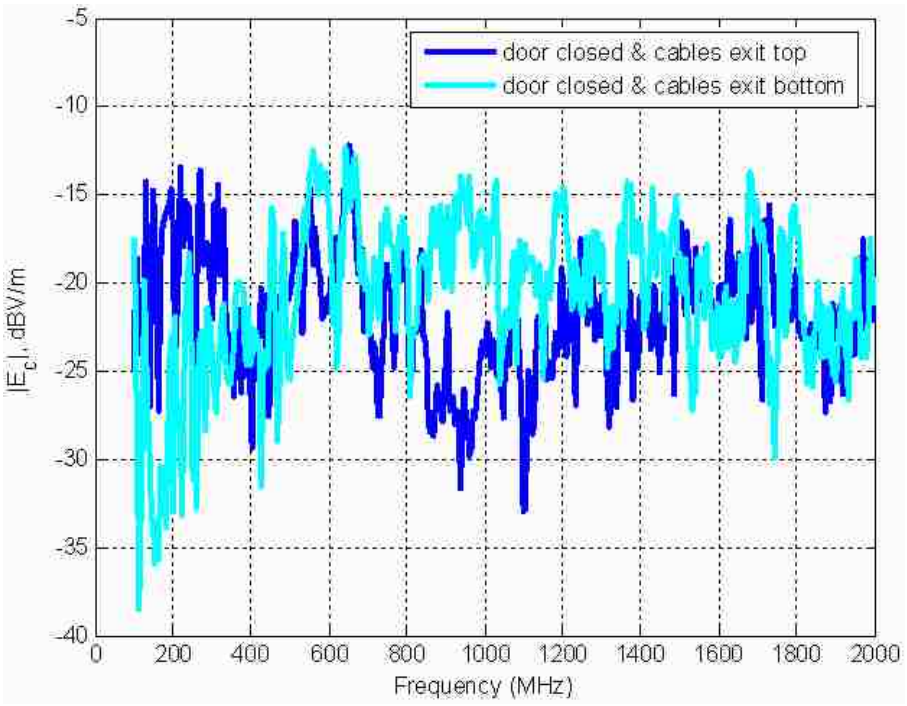

Figure 2.30. EMI Radiation Caused by CM Current for Closed Cabinet with Two Cables Egresses

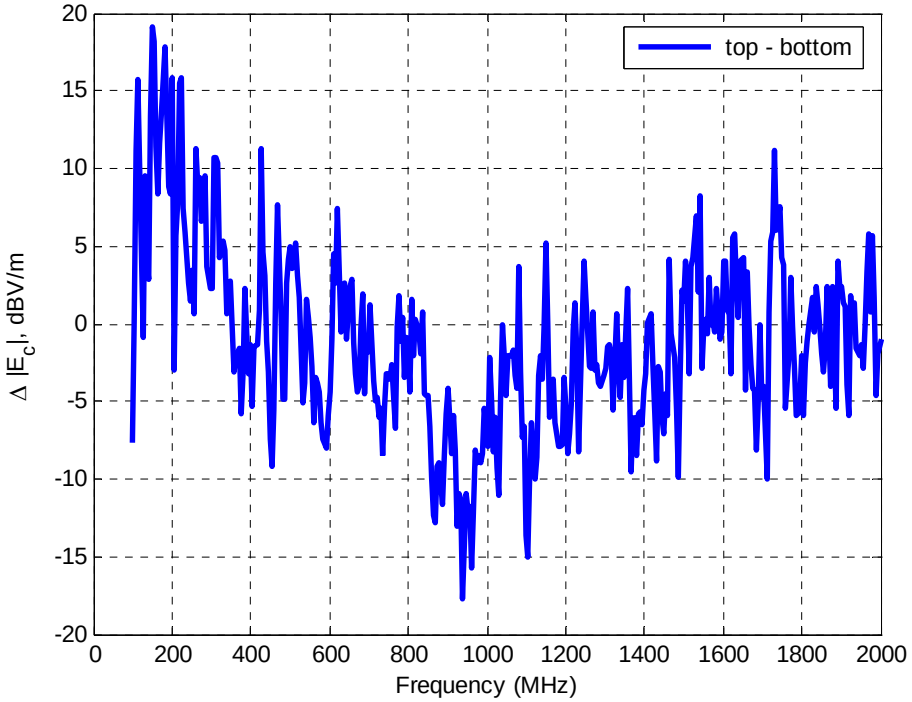

Figure 2.31. Difference of the EMI Radiation of the Two Cases in Figure 2.30

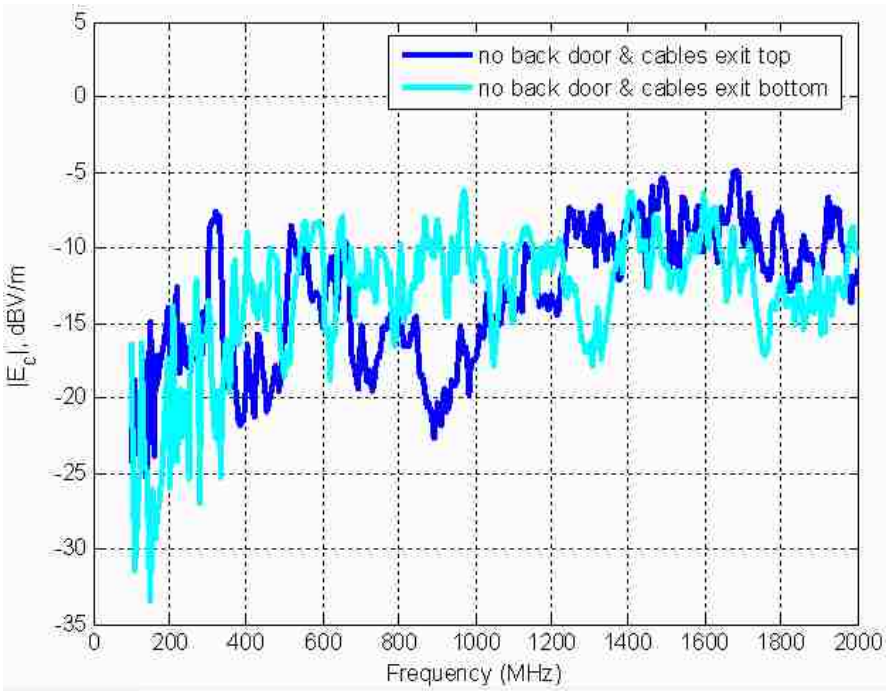

Figure 2.32. EMI Radiation by CM Current for Cabinet without Back Door and with Two Cable Egresses

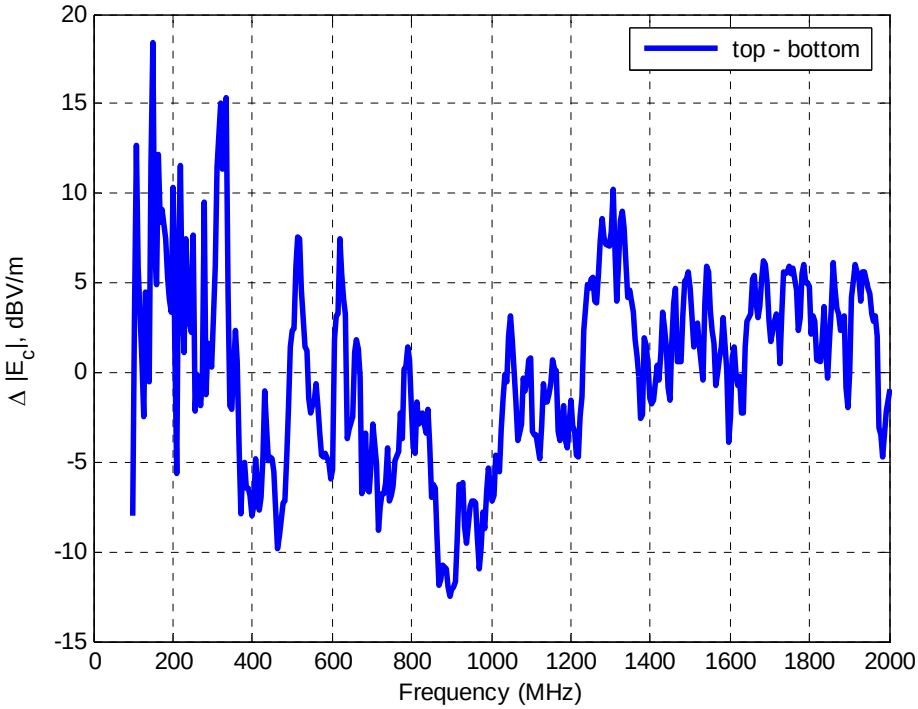

Figure 2.33. Difference of the EMI Radiation of the Two Cases in Figure 2.32

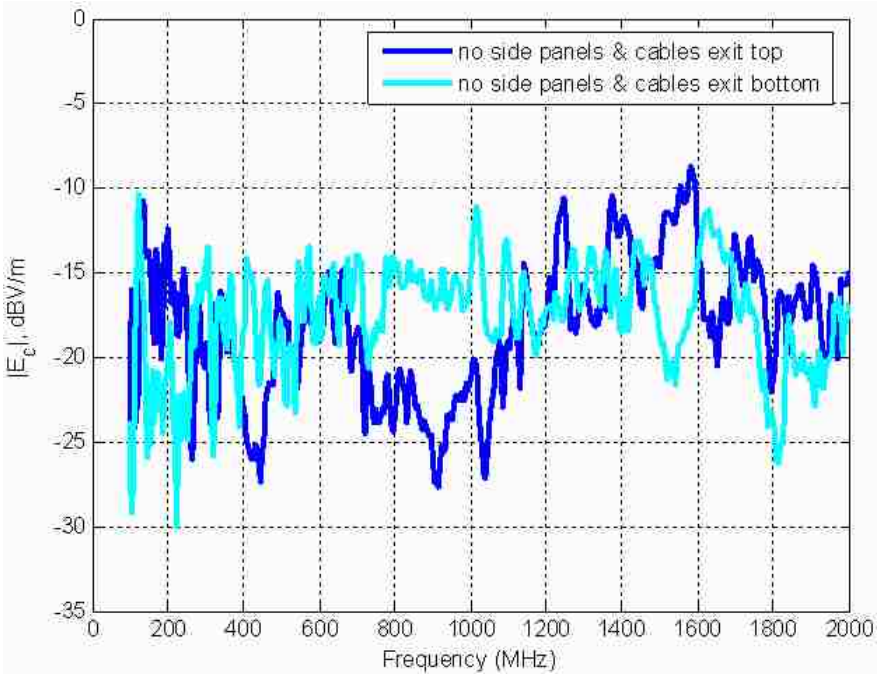

Figure 2.34. EMI Radiation by CM Current for Cabinet without Side-Panels and with Two Cable Egresses

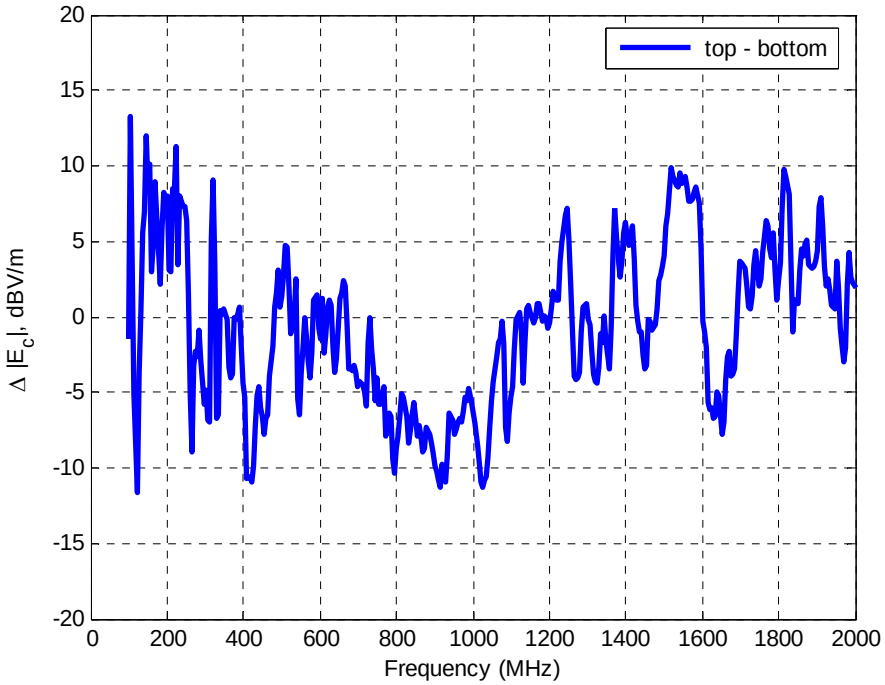

Figure 2.35. Difference of the EMI Radiation of the Two Cases in Figure 2.34

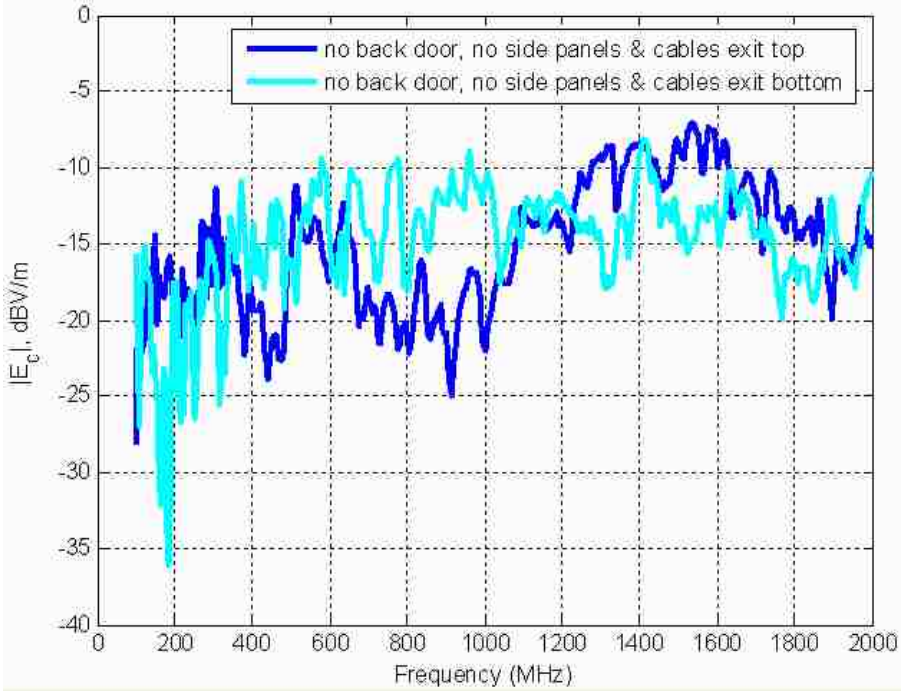

Figure 2.36. EMI Radiation by CM Current for a Cabinet without a Back Door and No Side Panels with Two Cable Egresses

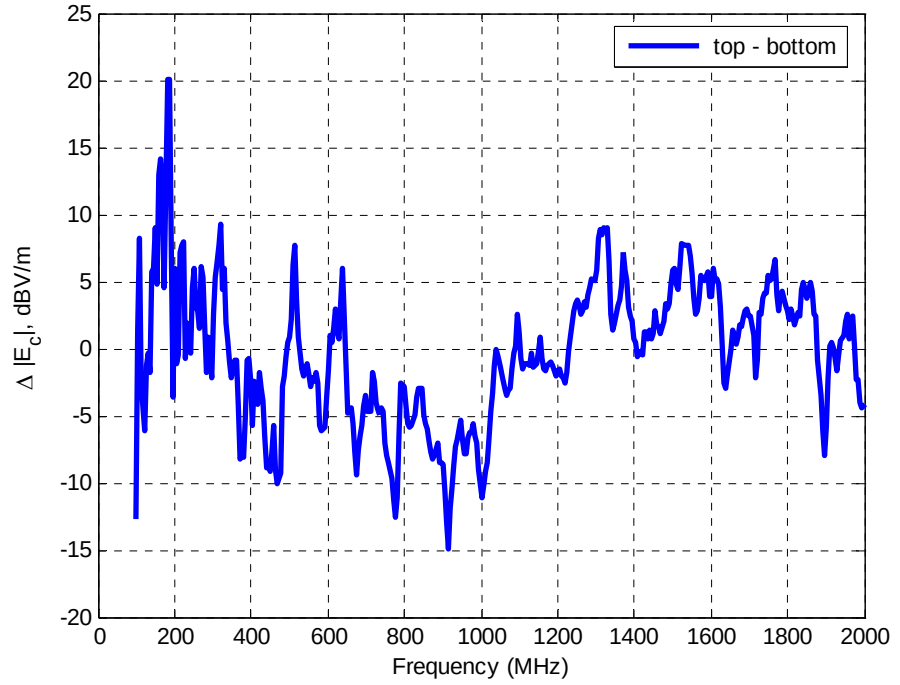

Figure 2.37. Difference of the EMI Radiation of the Two Cases in Figure 2.36

2.4.2.1.2. Cabinet on ferrite floor. A Ferrite floor absorbs waves otherwise bounced back by the ground and eliminates the interference introduced by the reflected waves in the measurement of the electric field radiated by the cabinet. A ferrite floor is typical in the environment of NCR's working node racks. Therefore measurements are performed for cabinet setting on the ferrite floor.

Figure 2.38 shows the radiation for various cabinet setups with the cables exiting the top of the cabinet; Figure 2.39 shows the radiation for the same cabinet setups as in Figure 2.38 with the cables exiting the bottom of the cabinet. Both figures have the plots of $|E_c|$ for all four cabinet setups – door closed and panels on, door off and panels on, Panels off and door closed and panels off and door off in the frequency range of 100 MHz to 2 GHz. Results are similar to those previously discussed for the cabinet setting on the ground plane. It is found that, for all four cabinet setups, with cables exiting either top or bottom, the cabinet at some frequencies provides less than 4 dBV/m of shielding effectiveness at lower frequencies and more than 15 dBV/m shielding effectiveness for higher frequencies.

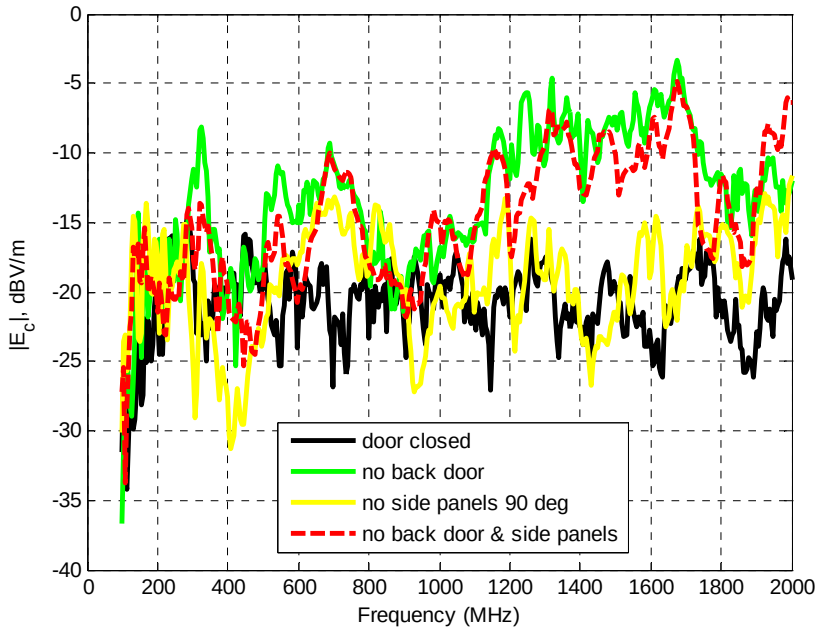

Figure 2.38. EMI Radiation by CM Current with Twisted Cables Exiting the Top for Cabinet on a Ferrite Floor

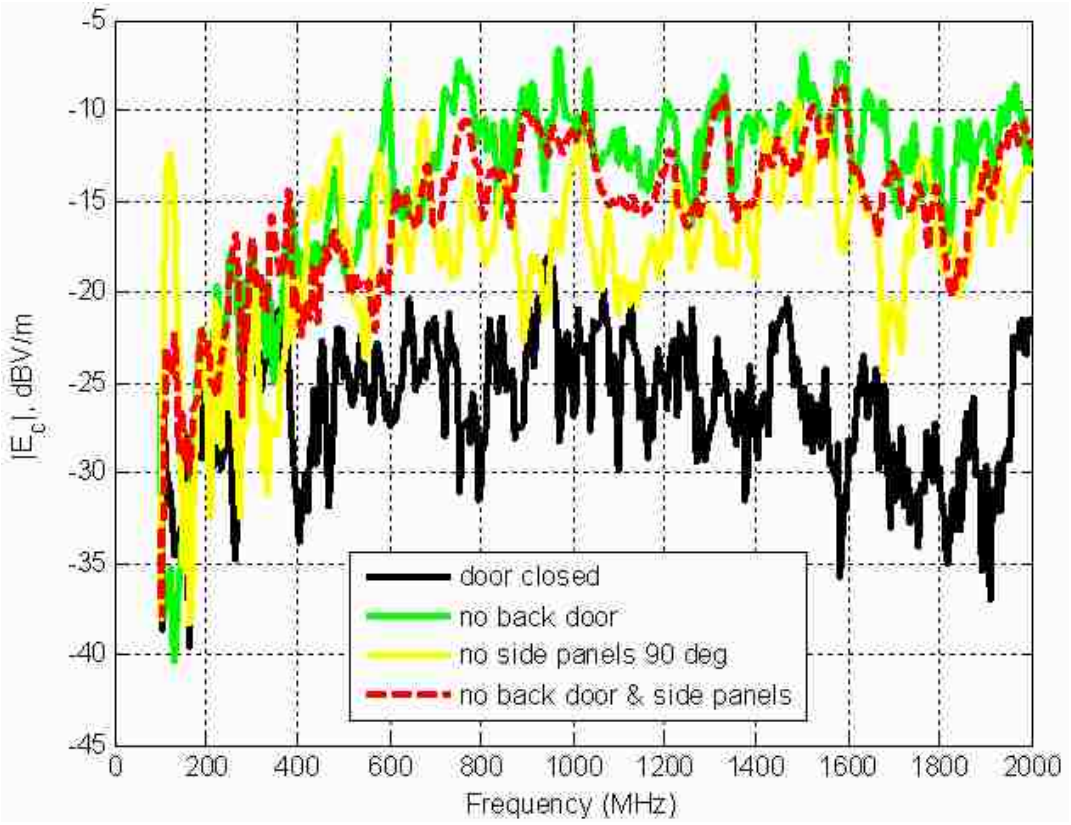

Figure 2.39. EMI Radiation by CM Current with Twisted Cables Exiting the Bottom for Cabinet on a Ferrite Floor

It is also true that with the cabinet setting up on the ferrite floor, the antenna detected the overall strongest radiation only when the back door was taken off and detected the overall weakest radiation when the two side panels were taken off while the back door was kept closed.

To find out how the radiation changes with the position of the cable egress, comparisons were made for cases of cables exiting top versus cables exiting bottom for each cabinet setup. Figure 2.40 and Figure 2.41 show the radiation comparison with a cabinet's back door closed. Figure 2.42 and Figure 2.43 are the radiation results and comparison when the cabinet's back door is taken off. Figure 2.44 and Figure 2.45 show the radiation when cabinet's side panels are taken off while the back door is kept closed. Figure 2.46 and Figure 2.47 are the plots of the radiated emission of the cabinet when both the side-panels and the back door are taken off.

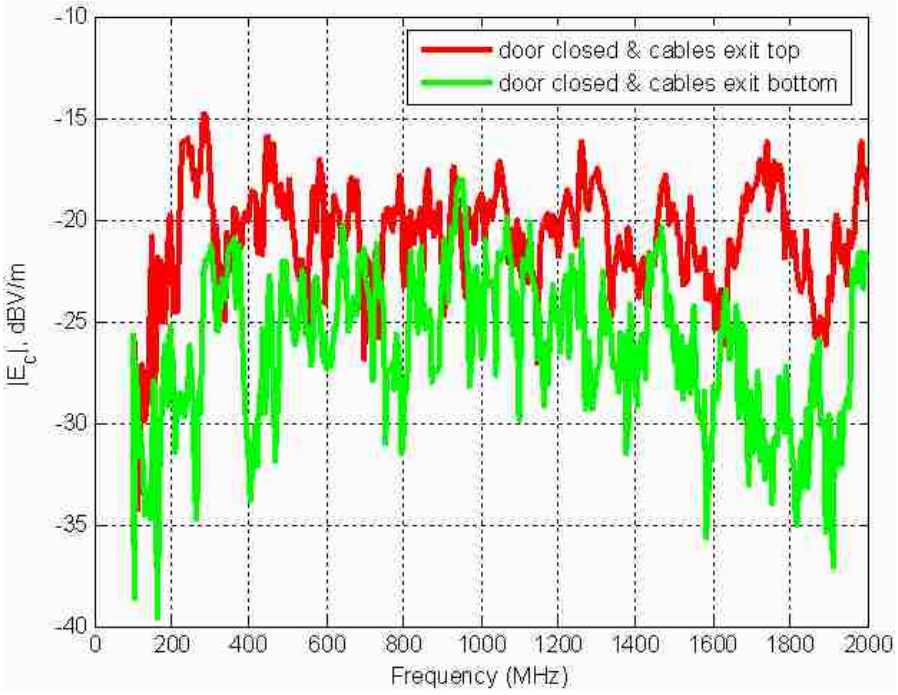

Figure 2.40. EMI Radiation by CM Current for a Closed Cabinet on a Ferrite Floor with Two Cable Egresses

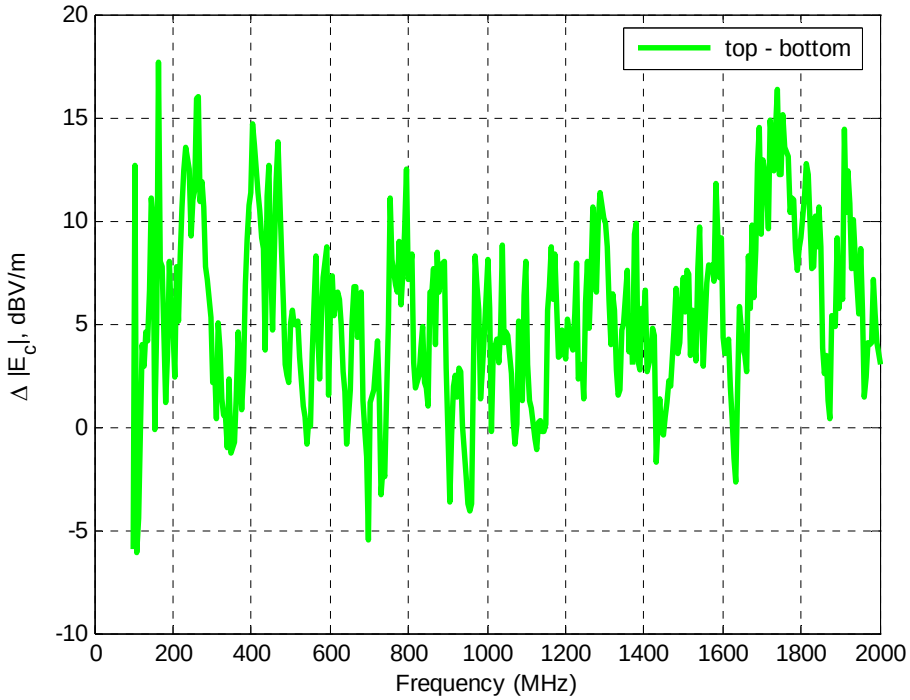

Figure 2.41. Difference of the EMI Radiation of the Two Cases in Figure 2.40

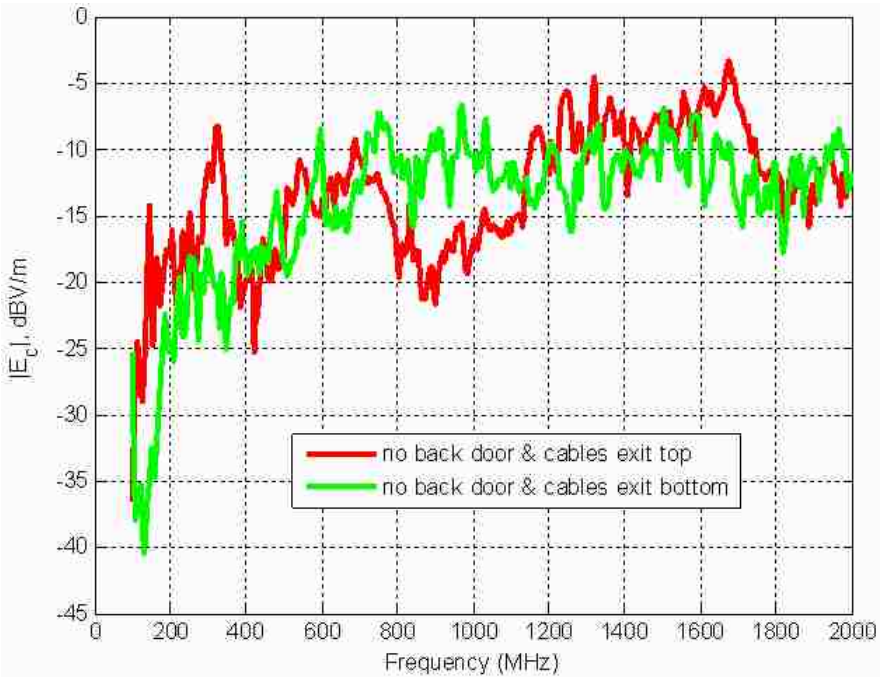

Figure 2.42. EMI Radiation by CM Current for a Cabinet without a Back Door on a Ferrite Floor and with Two Cable Egresses

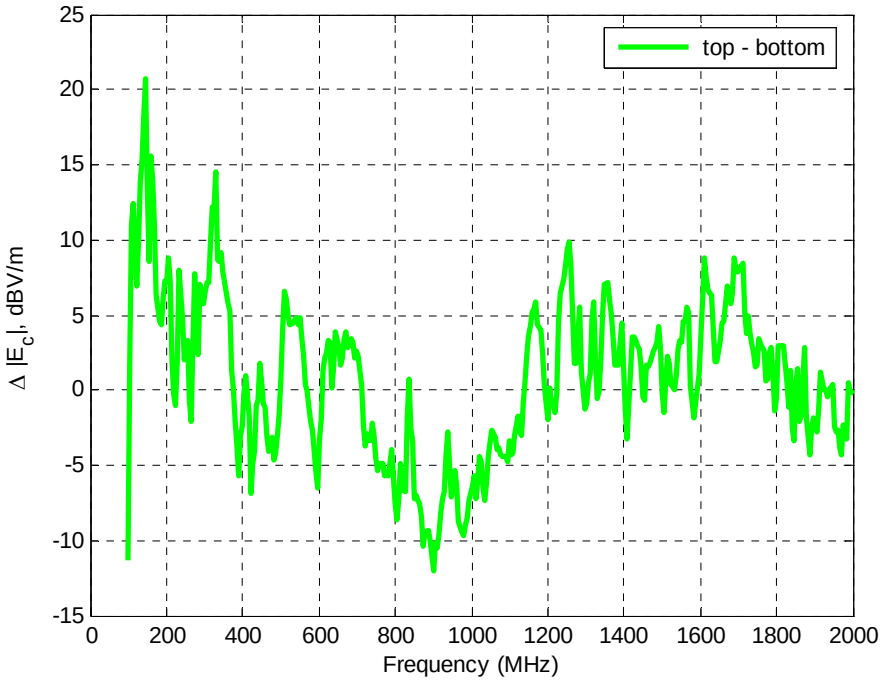

Figure 2.43. Difference of the EMI Radiation for the Two Cases in Figure 2.42

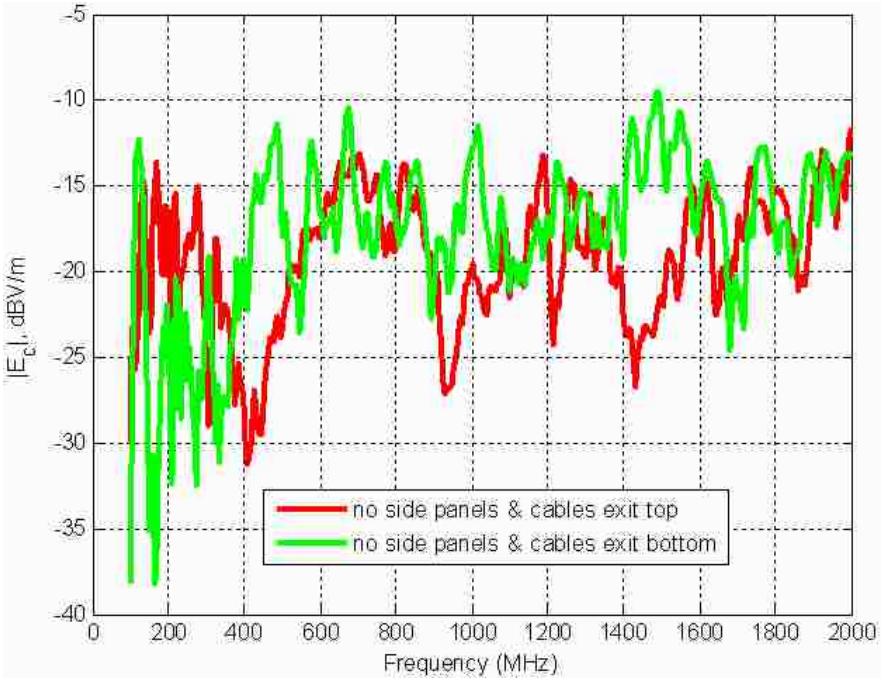

Figure 2.44. EMI Radiation by CM Current for a Cabinet without Side-Panels on a Ferrite Floor and with Two Cable Egresses

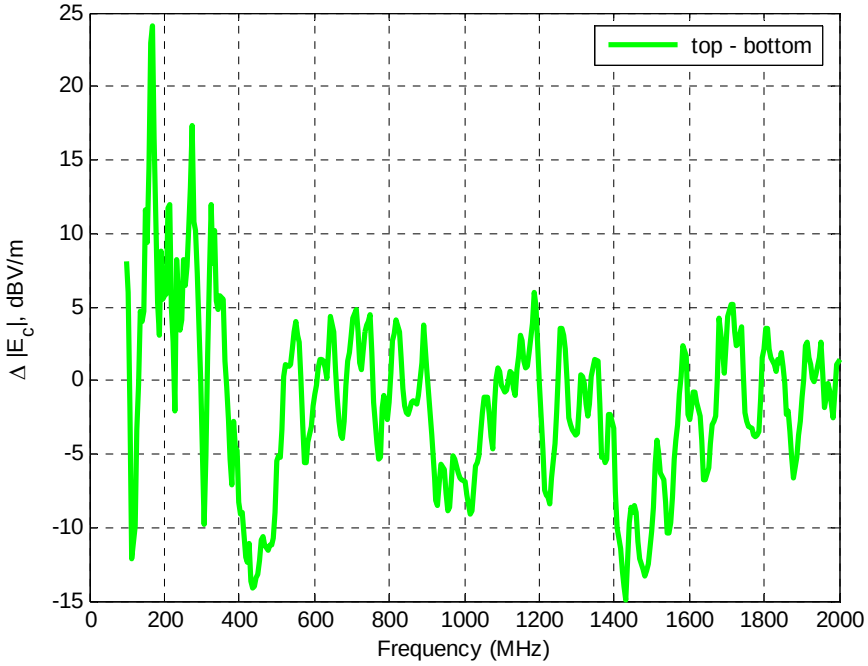

Figure 2.45. Difference of the EMI Radiation for the Two Cases in Figure 2.44

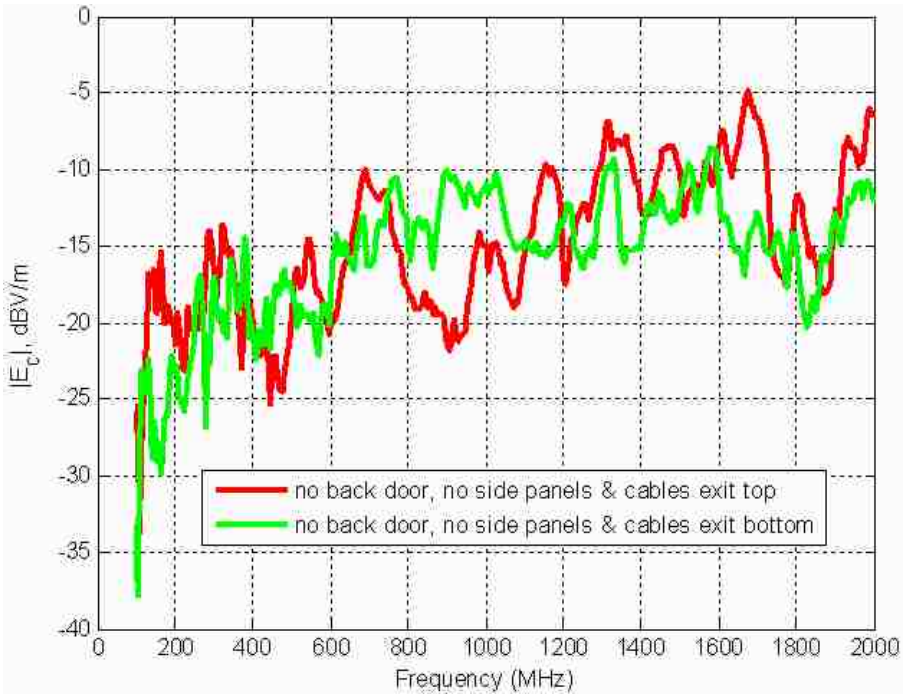

Figure 2.46. EMI Radiation by CM Current for a Cabinet with No Back Door and No Side Panels on a Ferrite Floor and with Two Cable Egresses

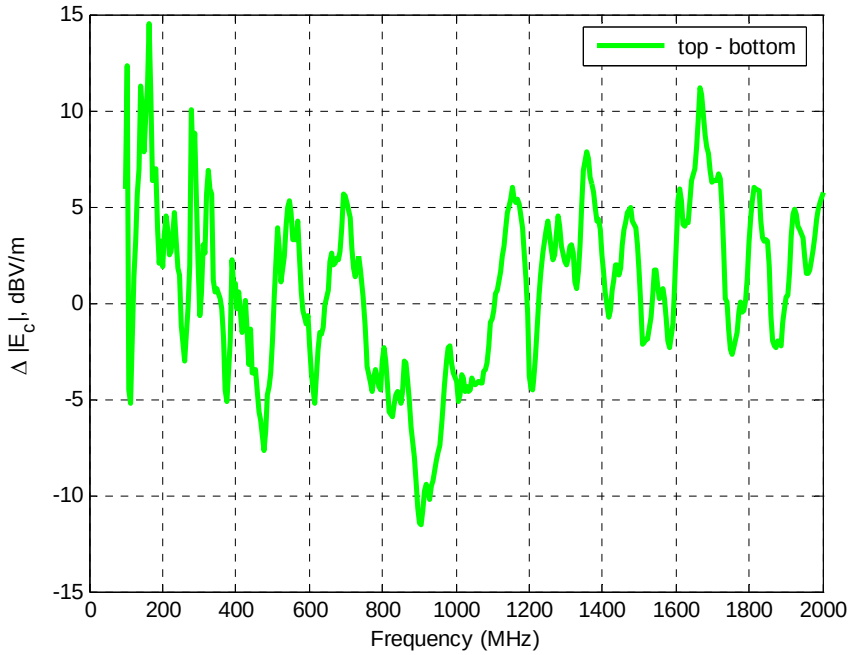

Figure 2.47. Difference of the EMI Radiation for the Two Cases in Figure 2.46

Figure 2.40 merits special attention. It shows that when cables exit the top of the rack cabinet, the radiations at almost all frequencies are higher than those measured for the cabinet setup where the twisted cables exit the bottom of the cabinet. Of particular note here are the frequencies of 627 MHz, 1254 MHz and 1881 MHz, which are the fundamental, the first harmonic and the second harmonic respectively of the BYNET data stream in the real working cabinet [1]. For the case of cables exiting the top, the radiation strength at the above mentioned frequencies are about -20 dBV/m, -17 dBV/m and -25 dBV/m respectively, which are at least 5 dBV/m higher than the corresponding values for a corresponding case which has the cables exiting the bottom of the cabinet.

Figure 2.41 shows the difference, in terms of $\Delta|E_c|$ in dBV/m, of the radiation as plotted in Figure 2.40. Positive values of $\Delta|E_c|$ imply that the radiated electric field from cables exiting the roof of the rack cabinet is larger than the corresponding radiation when cables exit the bottom of the rack cabinet. Figure 2.41 shows that for most frequencies in the range investigated, bringing cables out of the roof of the rack increased electric field radiation. This increase is greater than 15 dBV/m at some frequencies. The substantial increase in common-mode radiation over a broad frequency range is striking. This result shows that merely altering the means of cable egress to the top of the rack cabinet presents substantial technical risk to the ability to meet regulatory requirements on radiated emissions. To change the means of cable egress in a safe manner probably requires a substantial re-architecture of rack/cabinet shielding and cabling.

At the frequencies of significant interest, radiated emissions levels from NCR's systems often have much less than 10 dBV/m of margin. (Margin is the difference between the emission level and the regulatory limits). In fact at the frequencies that produce the highest emission levels, such as the BYNET frequencies, the margin may be only 2-4 dBV/m. Therefore, an increase in emission levels of 10-15 dBV/m might be a catastrophic change in terms of compliance with worldwide regulatory limits (CISPR 22).

For the cabinet setup with no back door, Figure 2.42 shows that except the frequency range 800 to 1200 MHz, when cables exit the top of the rack, at most frequencies the radiation is higher than that measured for the cabinet setup where cables exit the bottom. For the particular frequencies of 627 MHz and 1254 MHz, which are the fundamental and second harmonic of the BYNET data stream in the real working cabinet

[1], the radiation is still much higher than that measured for the cabinet setup where cables exit the bottom. For cables exiting the top, the radiation levels at 627 MHz and 1254 MHz are about -13 dBV/m and -5 dBV/m respectively, which are about 5 to 10 dBV/m higher than the radiation when the cables exit the bottom.

Regardless of the presence of the back door, for the cabinet setups with side panels taken off, as shown in Figure 2.44 and 2.45, the radiation in the cabinet setups where cables exit the top is lower at some frequencies and higher at other frequencies than that measured for the cabinet setup where cables exit the bottom. It is noticeable that, for cables exiting the top, the electric field strength at frequencies of 627 MHz, 1254 MHz and 1881 MHz are lower than that the electric field strength when the cables exit the bottom.

Figure 2.48 shows the radiations caused by common-mode current without twisted cables as the radiation source. The signals stop at the end of the traces on the PCB board in the module (refer to Figure 2.7 and Figure 2.8). It is concluded that the cabinet has a noise floor of about -60 dBV/m with the back door closed and a noise floor of about -50 dBV/m when the back door is taken off.

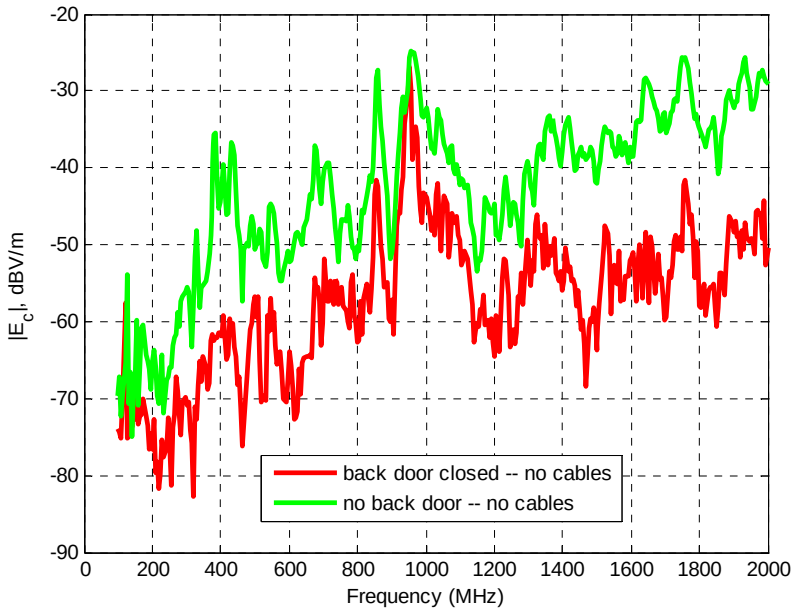

Figure 2.48. EMI Radiation by CM Current for Cabinet without Twisted Cables

2.4.2.1.3. Cabinet on ferrite floor and copper tape on side panels. It was found that the side-panels had poor contact with the brackets adhered to them. Using a LCR meter, it was detected that the value of the contact resistance between the panels and the brackets was in the number of thousands of Ohms. Therefore copper tape was used on the side panels to reduce high contact resistance between the side-panels and the brackets. The mixed-mode S-parameters were measured for the cabinet with the improved side-panels. The calculated $|E_c|$ is shown in Figure 2.49 with cables exiting top and Figure 2.50 with cables exiting bottom over a frequency range of 100 MHz to 2 GHz. Both figures have the plots of $|E_c|$ for two cabinet setups, back door closed and side panels on and back door off and side panels on. It is observed that, for both of the cabinet setups, with cables exiting either or bottom, the cabinet provides as low as less than 4 dBV/m of shielding effectiveness at lower frequencies and as high as more than 15 dBV/m shielding effectiveness for higher frequencies.

To observe how the radiation varies with a change in the position of the cable egress, a comparison was made for cases of cables exiting the top versus cables exiting the bottom for two cabinet setups, a closed cabinet with all panels and doors on and a cabinet without back door, as illustrated in Figure 2.51 and Figure 2.52 respectively. It is noticeable that overall, when cables exit the top, the radiation is higher than that when cables exit the bottom. However, exceptions always happen at frequencies between about 800 MHz to 1200 MHz. Specially when cables exit the top, the radiation is always much lower than that measured in the cabinet setup where the cables exits bottom. The difference can be as large as 10 dBV/m. This phenomenon was observed in all the previous measurements (refer to Figure 2.42 and Figure 2.43). The explanation is not available yet.

2.4.2.2. Radiation source – differential-mode currents. For most electric devices differential-mode (DM) currents causes much lower radiation than common-mode currents do. For the NCR's node rack cabinet with the installation of the PCB containing the simulated two differential signal traces, the radiation is relatively low compared with the radiations caused by common-mode current as in the discussions of Section 2.4.2.1.

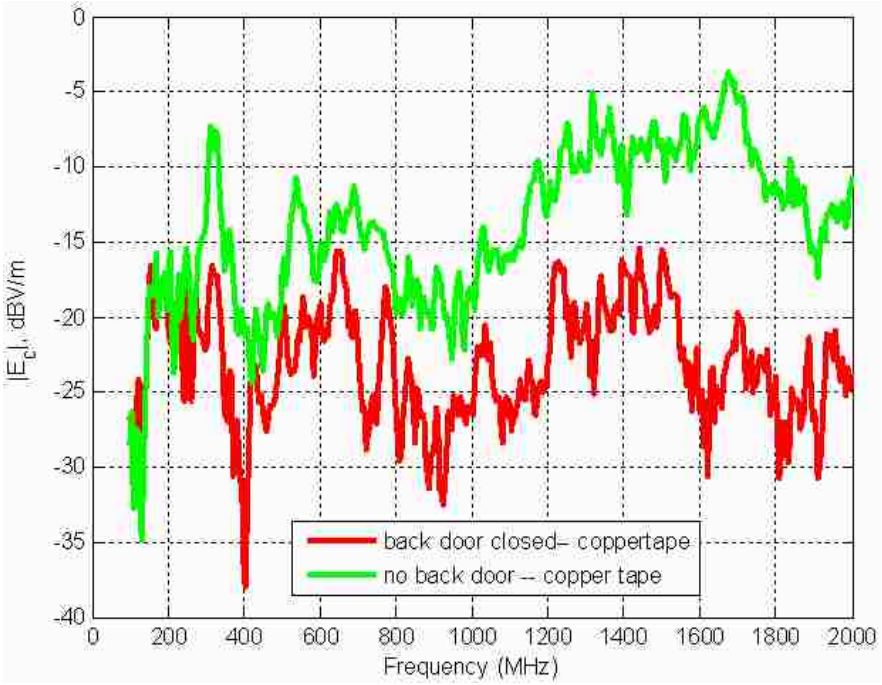

Figure 2.49. EMI Radiation by CM current with Twisted Cables Exiting Top for Various Cabinet Back Door Settings and with Copper Tape Used for Side Panels

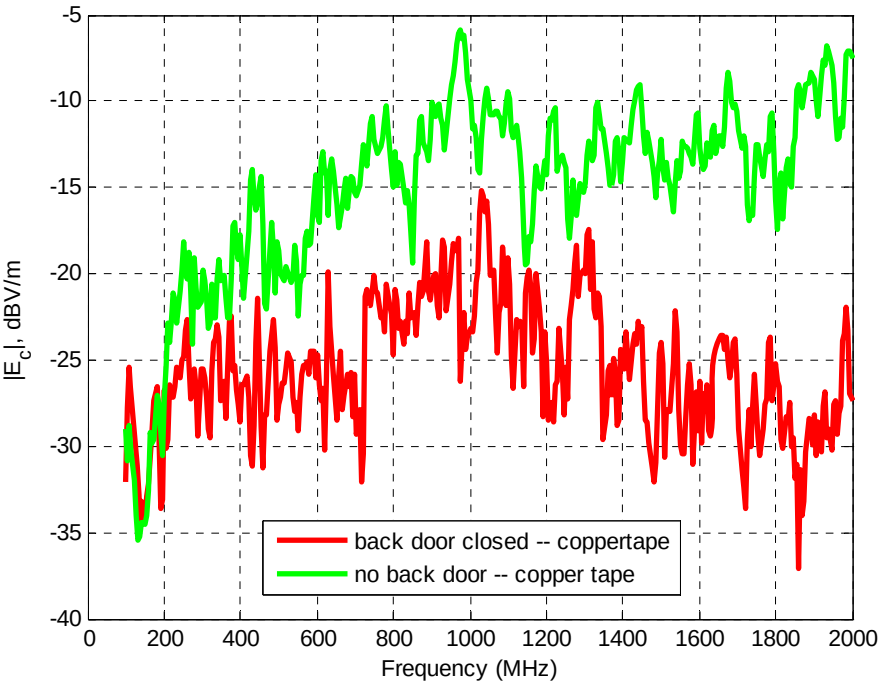

Figure 2.50. EMI Radiation by CM current with Twisted Cables Exiting Bottom for Two Cabinet Back Door Settings and with Copper Tape on Side Panels

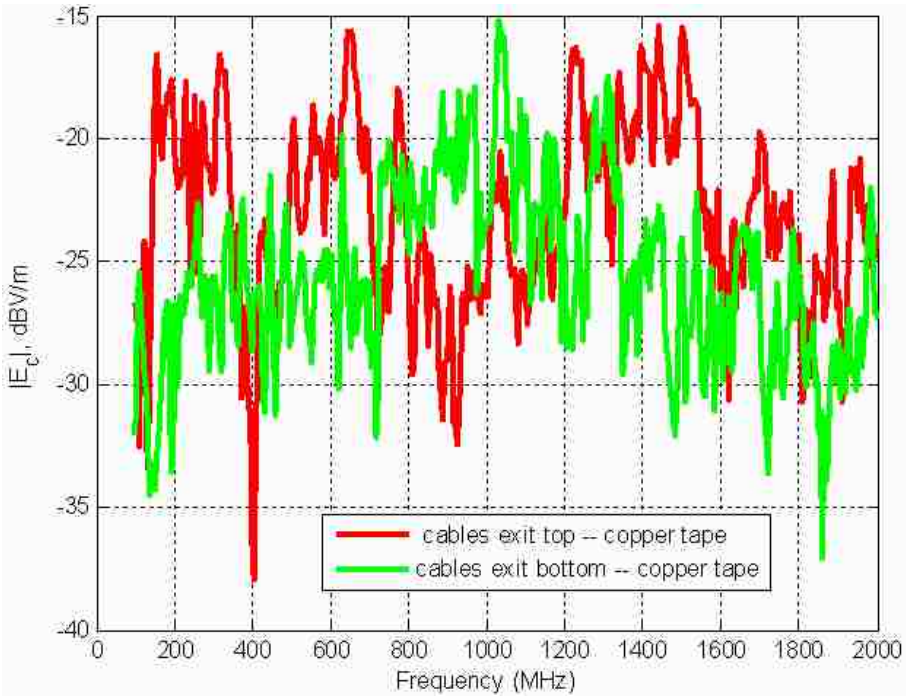

Figure 2.51. EMI Radiation by CM current for a Closed Cabinet with Two Cable Egresses and with Copper Tape Used for Side Panels

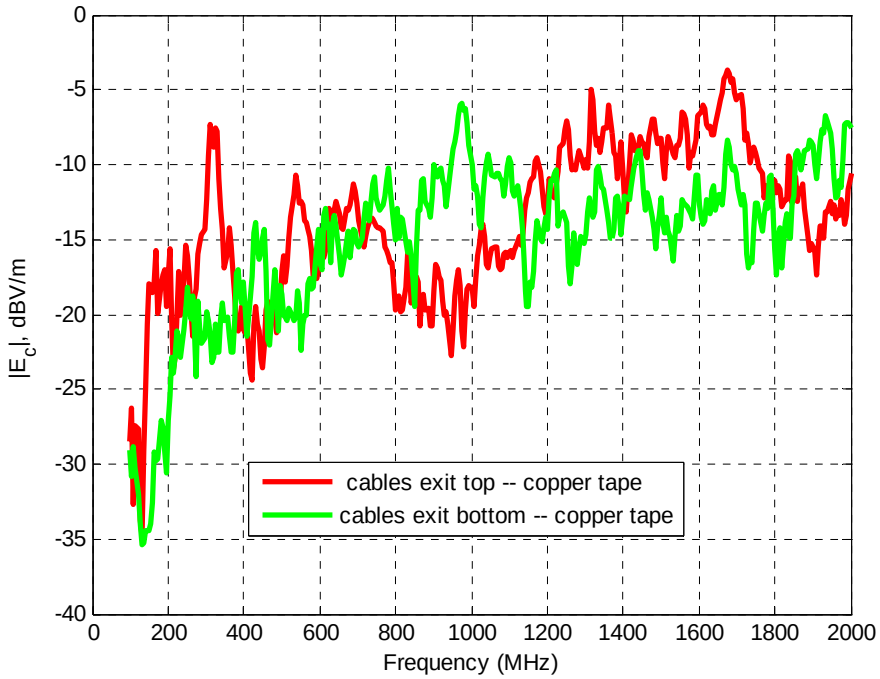

Figure 2.52. EMI Radiation by CM current with Two Cable Egresses for a Cabinet without Back Door and with Copper Tape on Side Panels

Figure 2.53 and Figure 2.54 show the electric field strength over the frequency of 100 MHz to 2 GHz for various cabinet setups on the ground plane with twisted cables exiting the top and the bottom of the cabinet respectively. Overall the electric field strength $|E_d|$ increases with frequency until reaching the maximum value of -14 to -12 dBV/m in the frequency range of 1700 to 2000 MHz. Comparing the two figures with corresponding plots for common-mode currents (refer to Figure 2.26 and Figure 2.27) in previous discussions, it is observed that for the rack cabinet, the radiation caused by the differential-mode currents is about 10 dBV/m lower than that caused by the common-mode currents. Figure 2.55 and Figure 2.56 are the plots for radiation when the cabinet side panels were taken off, and with the twisted cables exiting the top and exiting the bottom of the rack cabinet respectively. It is seen that the effects of side panels on the radiation caused by differential-mode current are similar to the effects observed for common-mode current excitation.

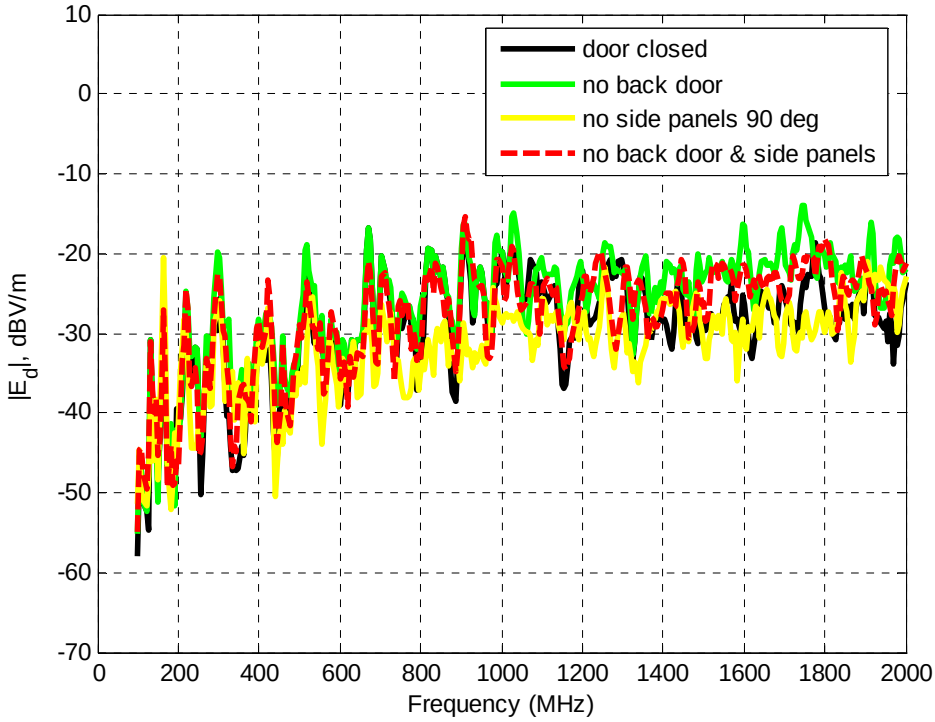

Figure 2.53. EMI Radiation by DM Current with Twisted Cables Exiting Top for Various Cabinet Setups

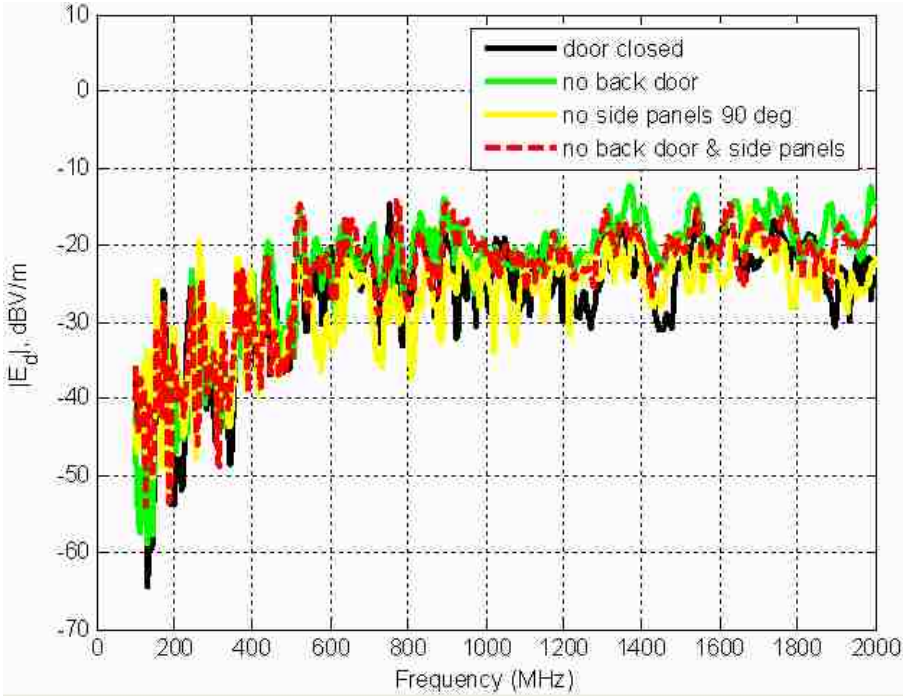

Figure 2.54. EMI Radiation by DM Current with Twisted Cables Exiting Bottom for Various Cabinet Setups

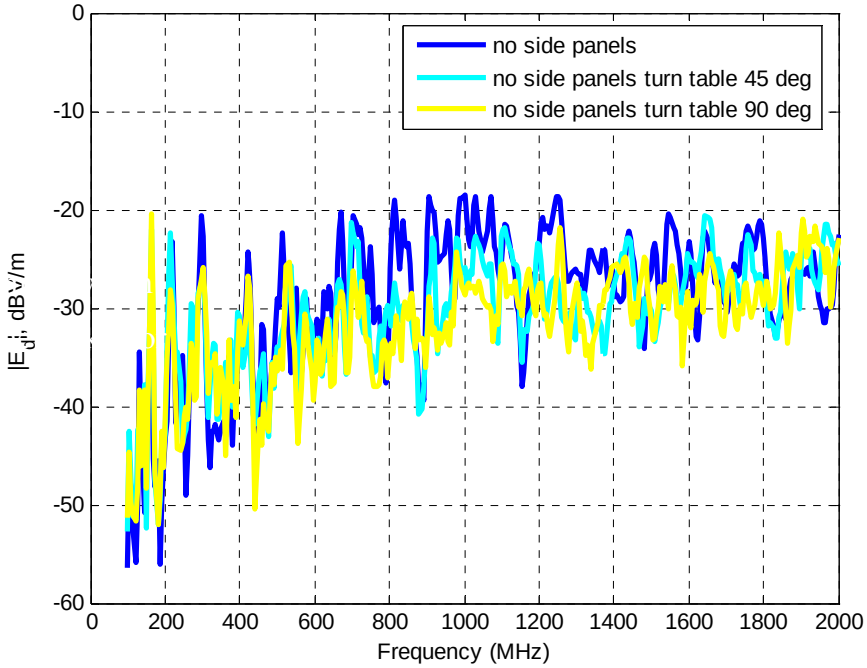

Figure 2.55. EMI Radiation by DM Current with Twisted Cables Exiting Top for Various Cabinet Setups in the Absence of Side Panels

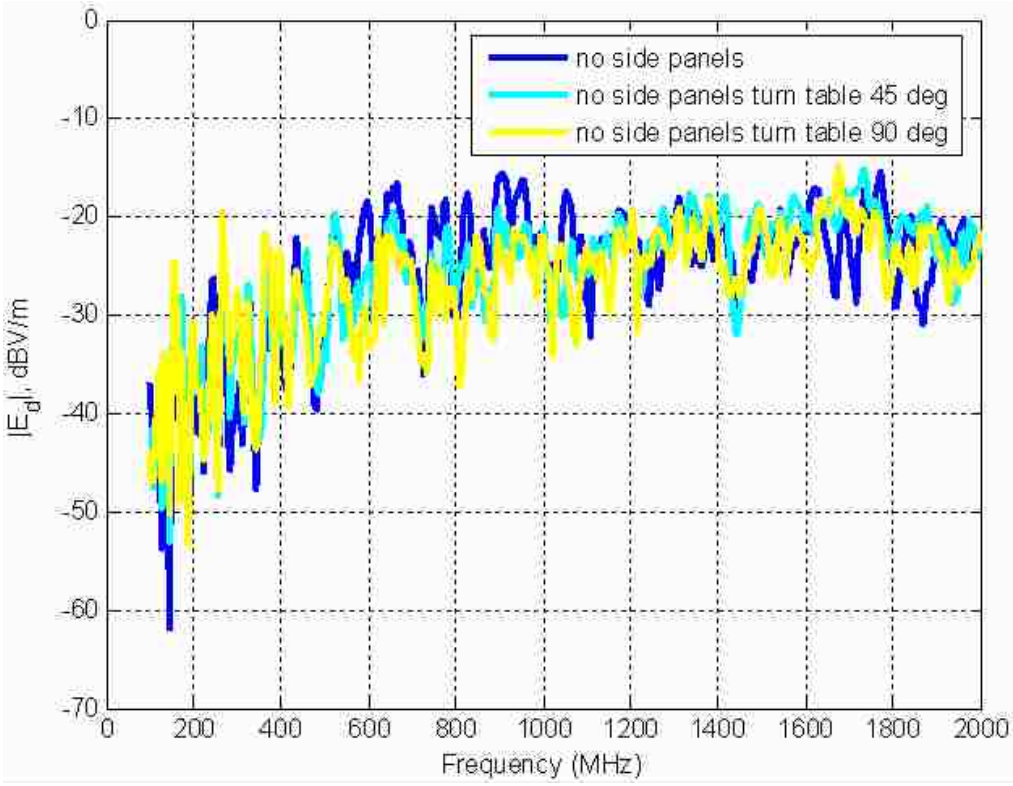

Figure 2.56. EMI Radiation by DM Current with Twisted Cables Exiting Bottom for Various Cabinet Setups in the Absence of Side Panels

Figure 2.57 through Figure 2.60 show the comparison of the radiation $|E_d|$ for two different cable egresses – cables exiting the top and cables exiting the bottom in different cabinet setups. Specially these configurations include the cases of back door closed and side panels on, back door taken off and side panels on, side panels off and back door closed and both side panels and back door off respectively. It is observed that for all four cabinet setups, at most frequencies, especially for frequencies higher that 1200 MHz, the radiations are stronger when cables exit the top of the cabinet, regardless of the configuration of the cabinet back door and side panels. This phenomena is in contract to the cases for common-mode current (refer to Figure 2.30, Figure 2.32, Figure 2.34 and Figure 2.36), where for most frequencies higher than 1 GHz, often the radiations are stronger when cables exit the top of the cabinet than that when cables exit the bottom of the cabinet.

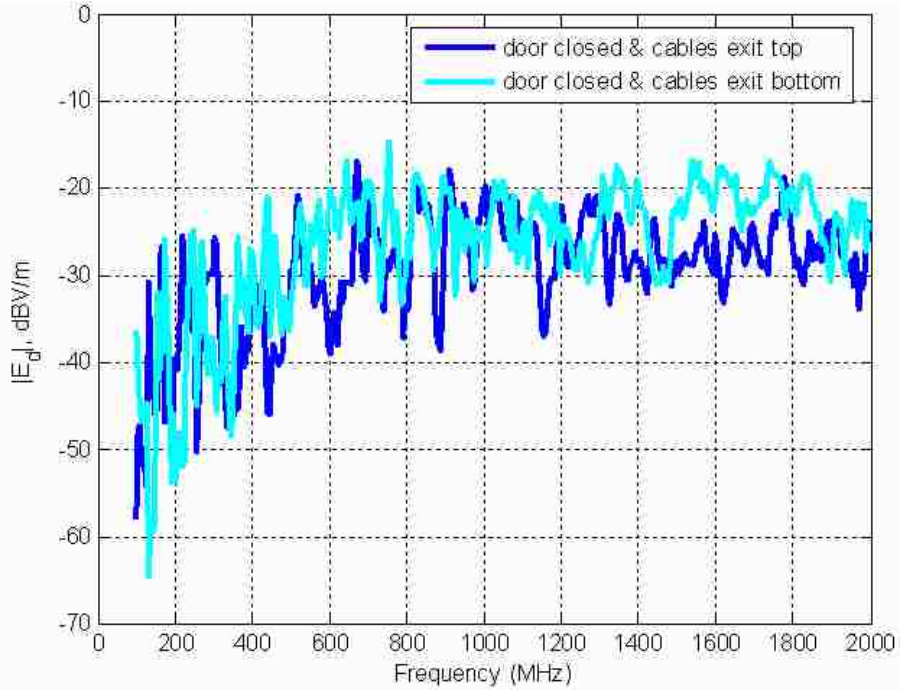

Figure 2.57. EMI Radiation Caused by DM Current for a Closed Cabinet with Two Cable Egresses

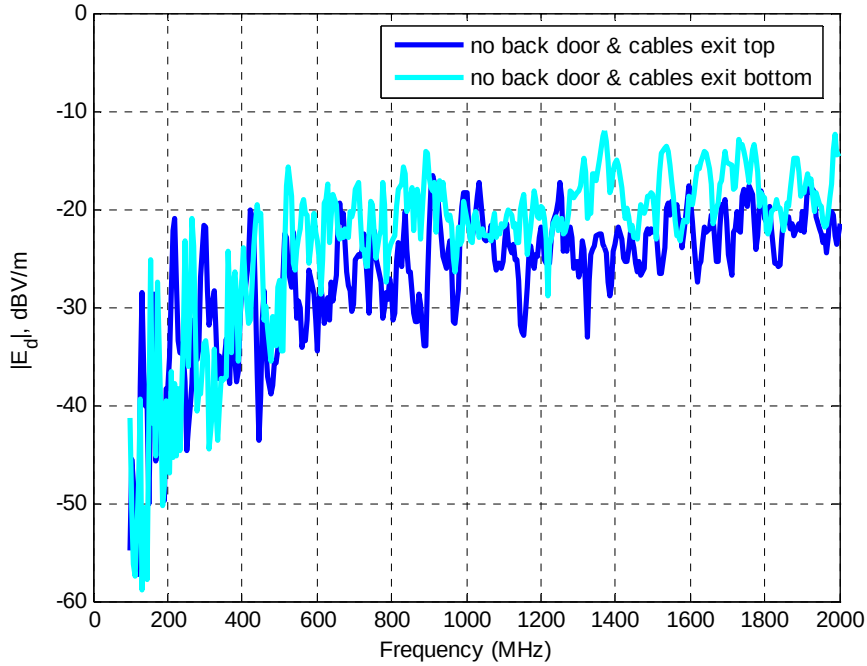

Figure 2.58. EMI Radiation by DM Current for a Cabinet without Back Door and with Two Cable Egresses

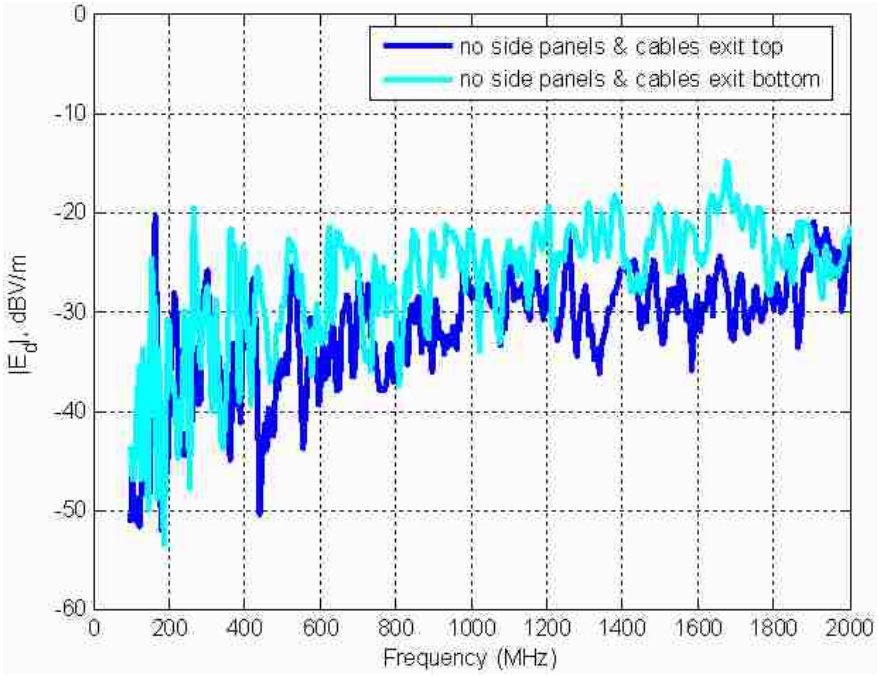

Figure 2.59. EMI Radiation by DM Current for Cabinet without Side Panels for Two Cable Egresses

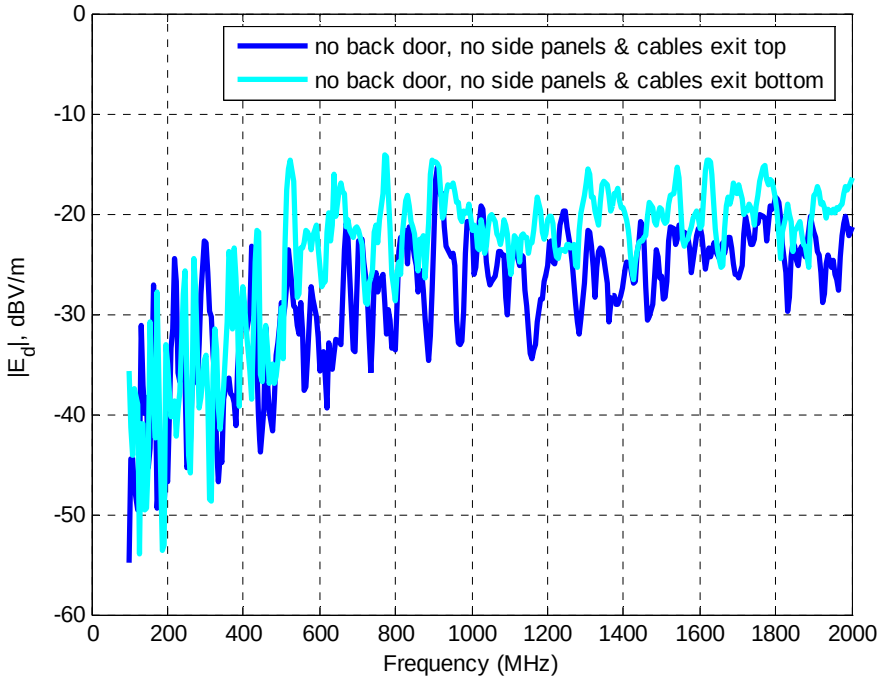

Figure 2.60. EMI Radiation by DM Current for Cabinet without Back Door and Side Panels for Two Cable Egresses

Figure 2.61 and Figure 2.62 indicate the radiations over a frequency range of 100 MHz to 2 GHz for cabinets on ferrite floor tiles with cables exiting the top and the bottom of the cabinet respectively. The $|E_d|$ increased with frequency, as incases for a cabinet setting on the ground. Comparing with corresponding plots for the same cabinet setup with common-mode currents, it is seen that the radiations caused by differential-mode currents is about 10 dBV/m lower than that for cabinet with common-mode currents. Figure 2.63 through Figure 2.66 compare the radiation of the cabinet with two kinds of cable egresses – cables exiting the top and cables exiting the bottom in four different cabinet setups, which are back door closed and side-panels on, back door off and side-panels on, side-panels off and back door closed and both cabinet's side-panels and back door off. Comparing with the radiation for the same cases without a ferrite floor, it is seen that in average the radiation decreased about 5 dBV/m., which is reasonable as a ferrite floor reduces ground reflections to the wave.

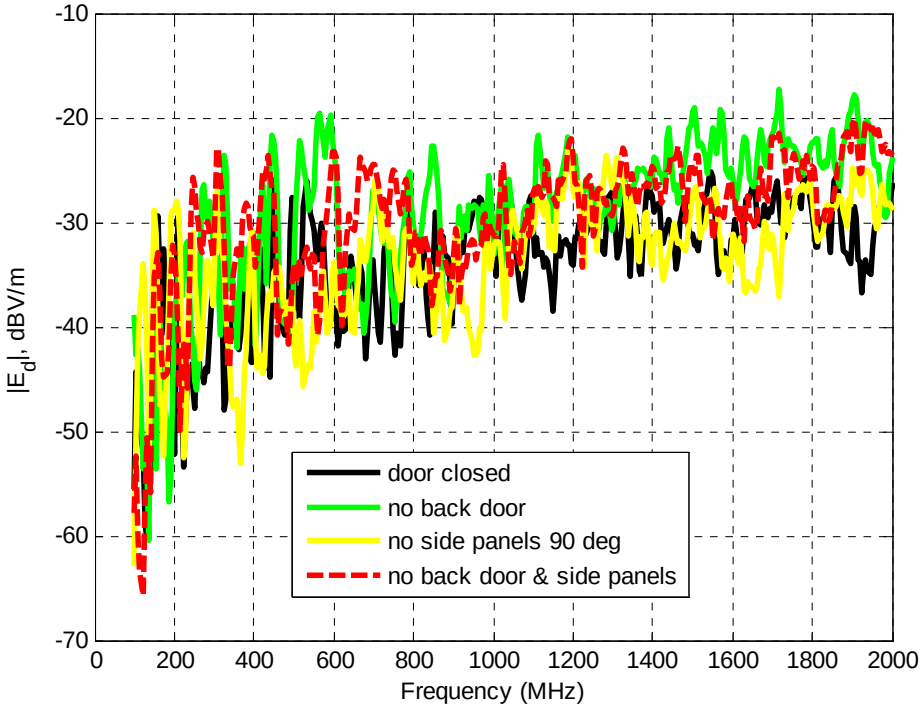

Figure 2.61. EMI Radiation by DM Current with Twisted Cables Exiting Top for Various Cabinet Setups on a Ferrite Floor

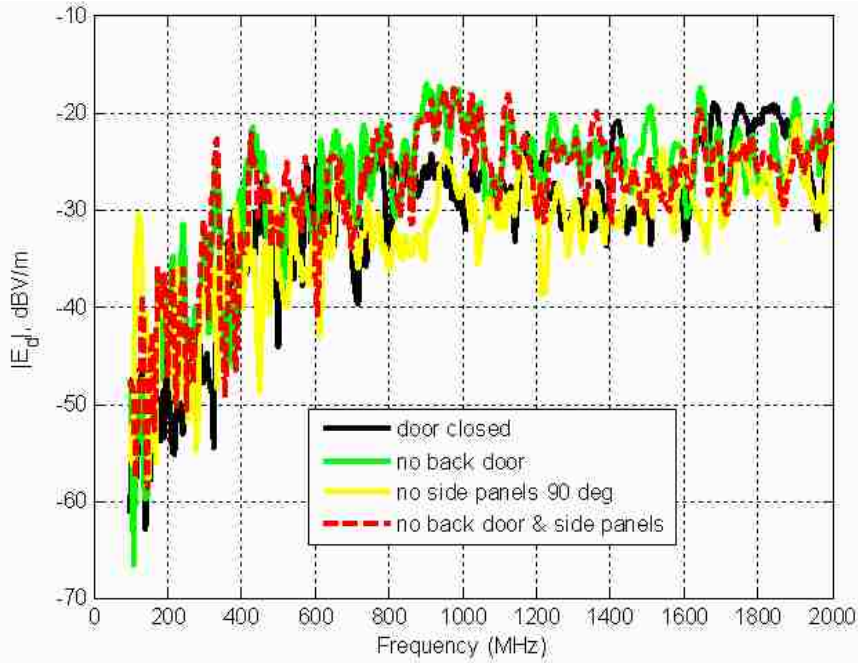

Figure 2.62. EMI Radiation by DM Current with Twisted Cables Exiting Bottom for Various Cabinet Setups on a Ferrite Floor

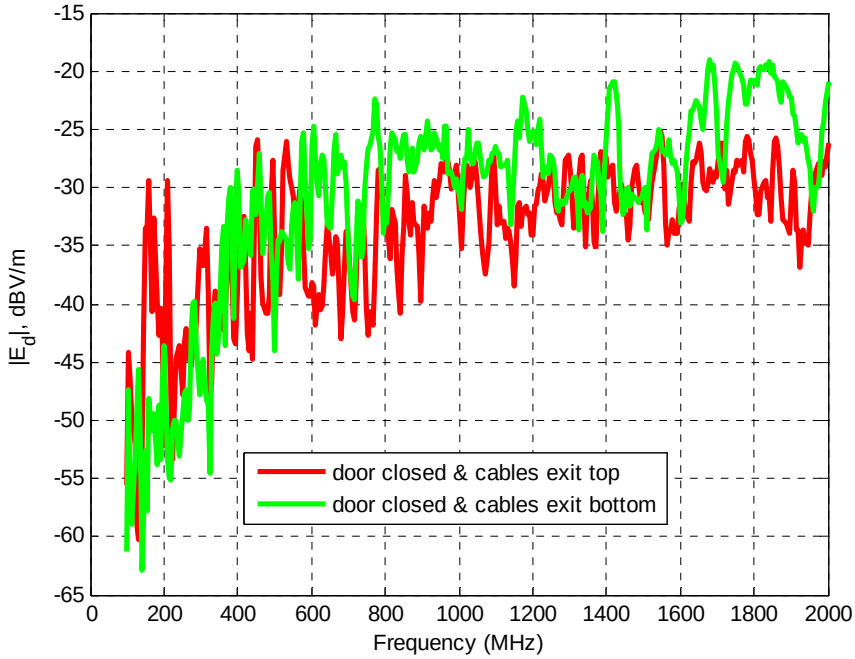

Figure 2.63. EMI Radiation by DM Current with Two Cable Egresses for a Closed Cabinet on a Ferrite Floor

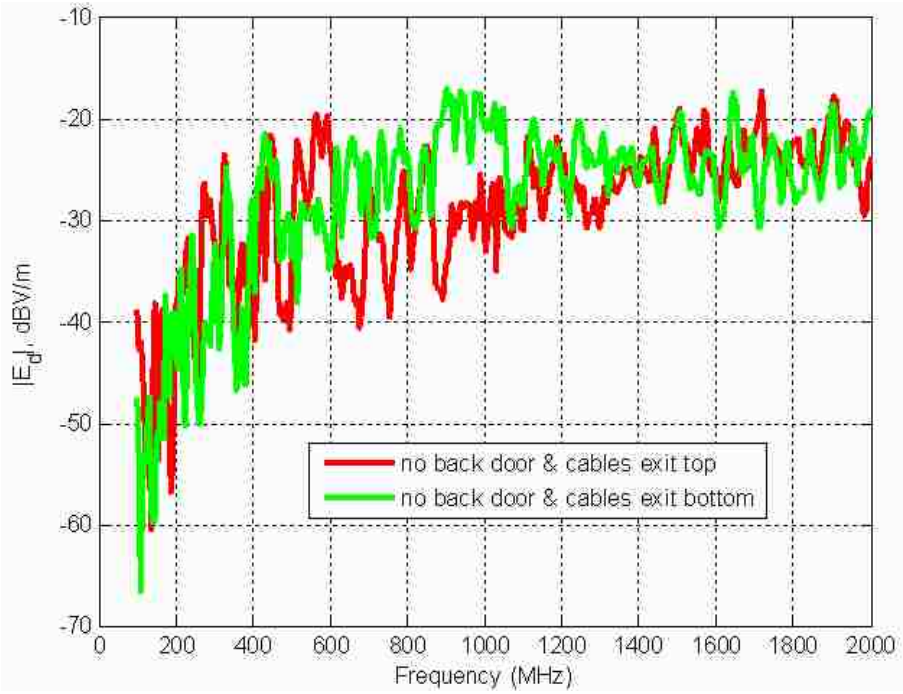

Figure 2.64. EMI Radiation by DM Current with Two Cable Egresses for a Cabinet without a Back Door on a Ferrite Floor

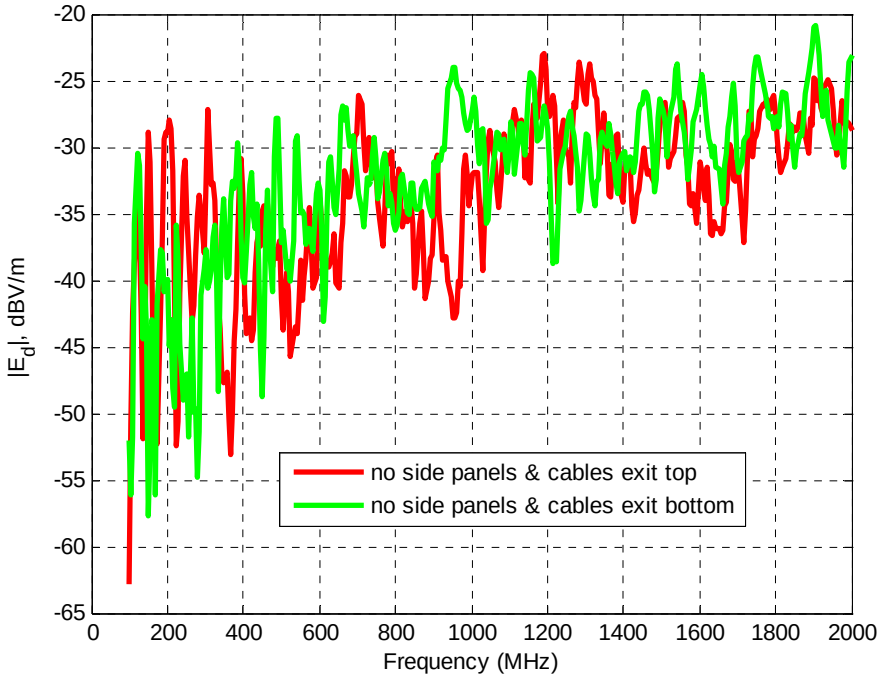

Figure 2.65. EMI Radiation by DM Current with Two Cable Egresses for a Cabinet without Side Panels on a Ferrite Floor

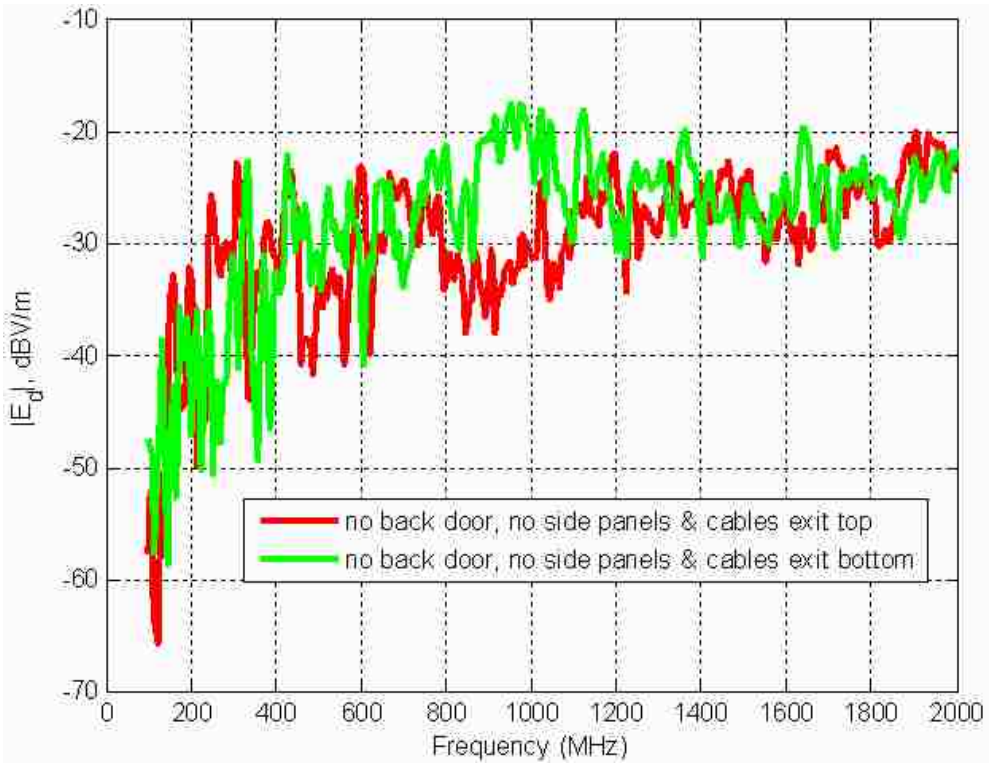

Figure 2.66. EMI Radiation by DM Current with Two Cable Egresses for a Cabinet without a Back Door and Side Panels on a Ferrite Floor

Figure 2.67 shows the radiations caused by differential-mode current without twisted cables as the radiation source. It is seen that the cabinet has a noise floor about -60 dBV/m when the back door of the cabinet which drops to about -70 dBV/m when the back door is taken off.

Figure 2.68 through Figure 2.71 show the results for radiation over the frequency range of 100 MHz to 2 GHz for cabinets on ferrite floor tiles. The side panels of the cabinet were grounded by applying copper tape between the side panels and the brackets on the side panels for the purpose of reducing the contact resistance. It is interesting to see that for the case of cables exiting the bottom with copper tape used (Figure 2.71), the maximum value of the radiation over the frequency range 100 to 2000 MHz is increased by about 5 dBV/m , compared with the maximum radiation in a similar case without copper tape applied (Figure 2.64), where the maximum radiation is about -18 dBV/m in the frequency range of 800 to 1000 MHz.

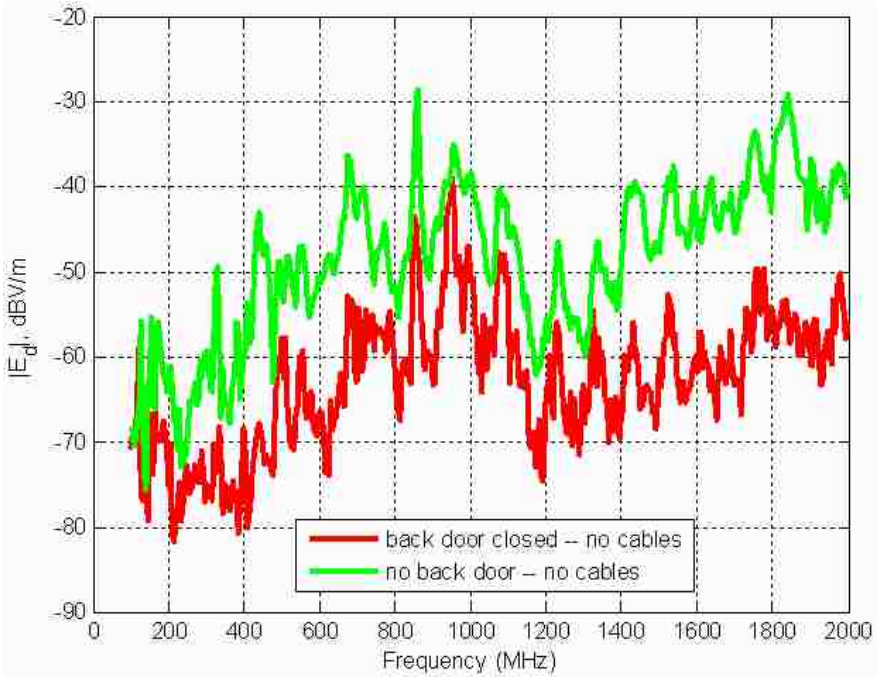

Figure 2.67. EMI Radiation by DM Current for Two Cabinet Setups on a Ferrite Floor without Twist Cables as the Radiation Source

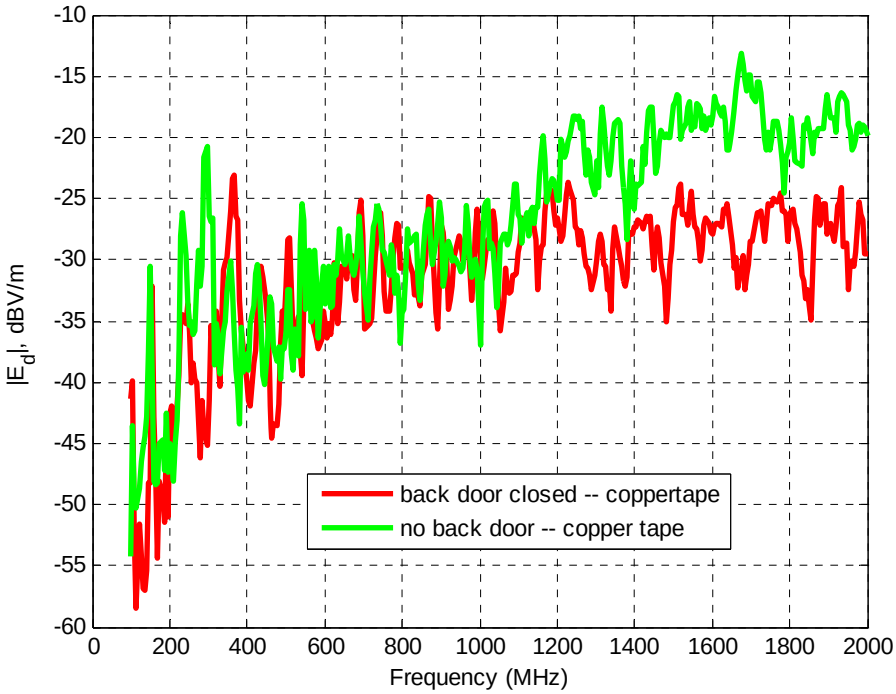

Figure 2.68. EMI Radiation by DM Current with Cables Exiting Top for Two Cabinet Setups on a Ferrite Floor and with Copper Tape on Side Panels

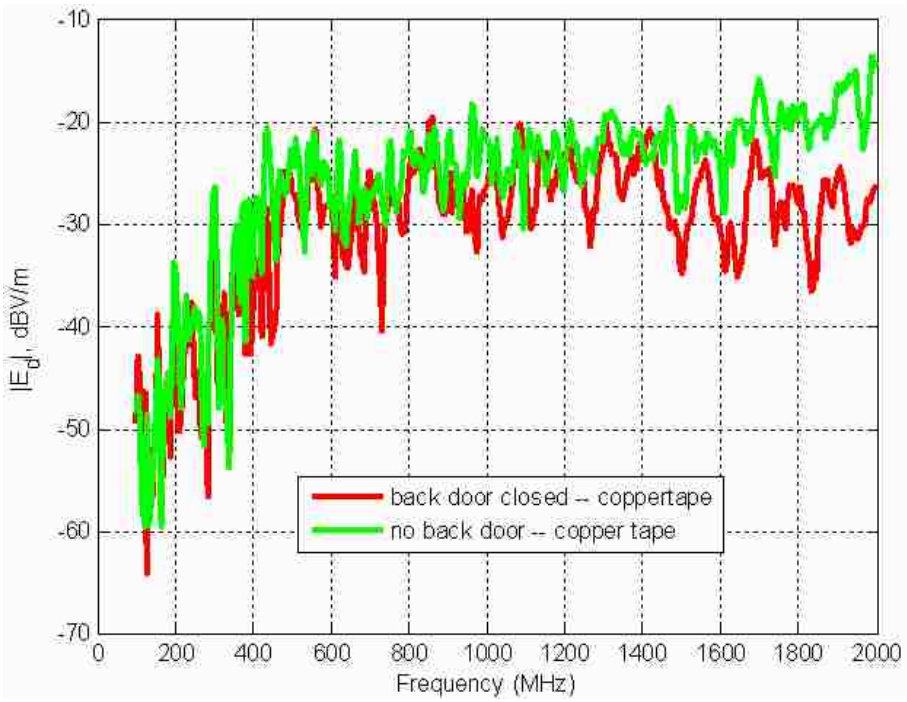

Figure 2.69. EMI Radiation by DM Current with Cables Exiting Top for Two Cabinet Setups on a Ferrite Floor and with Copper Tape on Side Panels

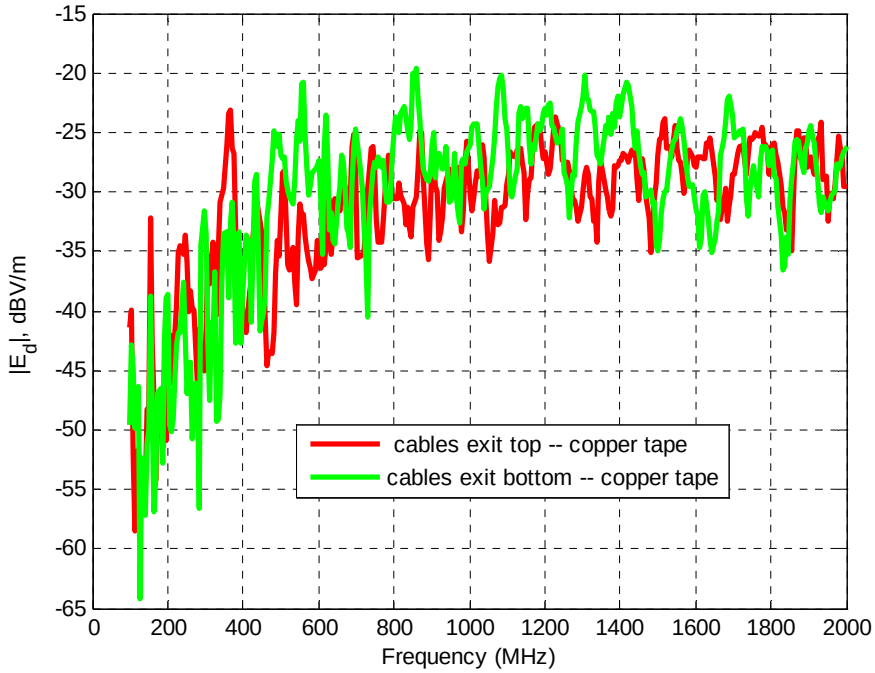

Figure 2.70. EMI Radiation by DM Current with Two Cable Egresses for a Closed Cabinet on Ferrite Floor and with Copper Tape on Side Panels

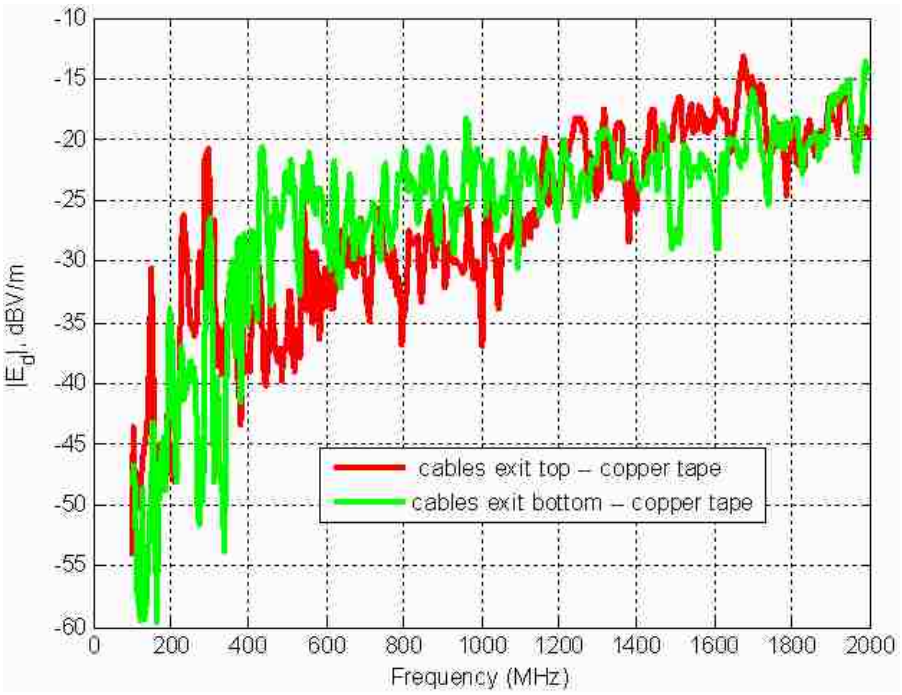

Figure 2.71. EMI Radiation by DM Current with Two Cable Egresses for a Cabinet on a Ferrite Floor without Back Door and with Copper Tape on Side Panels

2.5. SUMMARY AND CONCLUSIONS

The NCR node rack cabinet with the controlled configurations provides an average of 10 dBV/m shielding effectiveness, which is essential in meeting EMI regulatory requirements with the current system. The cabinet's structure, without any active source included, has a noise floor of about -60 dBV/m.

Regarding the cable egress, a primary conclusion is that mixed-mode S-parameter measurements on the controlled configurations of the NCR node rack equipment demonstrate that cables that egress from the top of the rack cause significantly higher EMI risk than the conventional egress fashion from the bottom of the rack. The increase in radiation can be as much as 10-15 dBV/m higher at some frequencies than when cables egress from the bottom of the rack, near the floor. Therefore, cable egress should not be changed without also changing the overall shielding architecture of the rack cabinet. To be effective, such a change may necessitate modifying the shielding requirements on chassis internal to the rack and on cabling.

The back door and side panels greatly affect the measured radiation. Taking off the back door alone increases the radiation by an average of 10 dBV/m over the frequency range of 100 MHz to 2 GHz. Removing both side panels has similar but weaker effects on the measured radiation than removing the back door does. Grounded side panels helps slightly decrease the radiation by about 2 to 3 dBV/m on the overall frequency range.

Regardless whether the cabinet rested on the ground or on ferrite floor tiles, It was consistently observed that when cables exit the top, the radiation is weaker than the cases when cables exit the bottom for a frequency range of 800 MHz to1200 MHz. This was observed almost for all cabinet setups. It should to be investigated and maybe it is related to the ceiling of the chamber.

3. NUMERICAL MODELING

3.1. INTRODUCTION

Numerical techniques are commonly used in solving EMC/EMI tasks. An agreement between measurements and model simulations can validate a design modification and render possible ways to the improved performance of a device. From the viewpoint of numerical simulation, the structure of the NCR's node rack is complicated and its sizes are huge due to its working frequency of up to 2 GHz. Both make the numerical modeling of the node rack a tempting but challenging task.

The efforts of the numerical modeling of NCR's node rack started with the construction of a complex model in HFSS that contained the true structure of the rack with an ideal current source. The ultimate restriction of limited computer memories failed a convergence in the HFSS simulation, resulting in a simplified model that was successful. The simplified HFSS model was simulated with the back door of the rack cabinet closed/removed and with the ideal current source exiting the bottom/top of the cabinet, etc. The simulations do show, however, that the rack cabinet can provide on the order of 10 dB of overall shielding effectiveness, which is a good agreement with the measurements taken in NCR for a functioning node rack and with the swept frequency measurements and study taken in the UMR's EMC Lab.

3.2. SIMULATION SETUP

3.2.1. Complex HFSS Model. The complex HFSS model containing the true structure of the rack cabinet is built as in Figure 3.1 (source not shown). Figure 3.2 through 3.5 show different parts of the node cabinet. The related setups of the simulation are as follows:

1) Boundary: Infinite ground plane and radiation boundary condition for the remaining boundaries.
2) Excitation: current source (1000mA) of the cable with one end in the module and the other end just above the ground plane.
3) Analysis: frequency sweep tried is from 100 MHz to 500 MHz. HFSS warned "extremely long simulation time" for frequencies above 1 GHz.

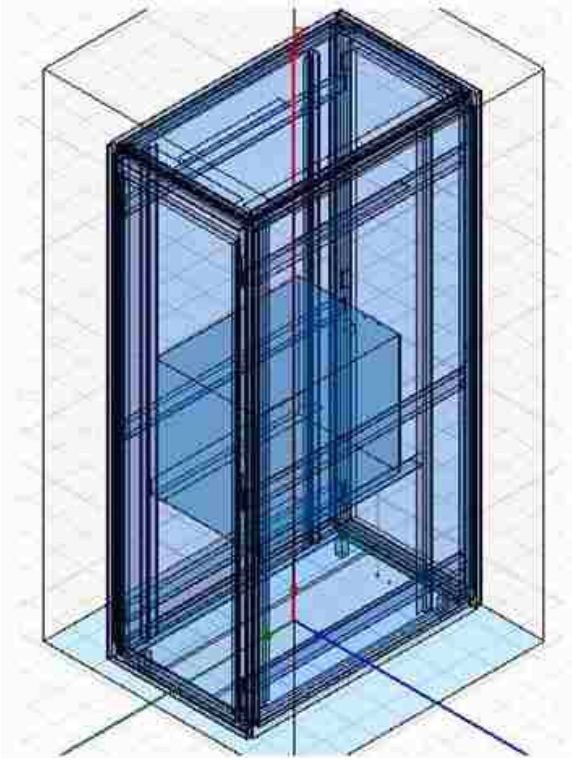

Figure 3.1. Complex HFSS Model – the NCR Node Rack Cabinet without Current Source (3D View)

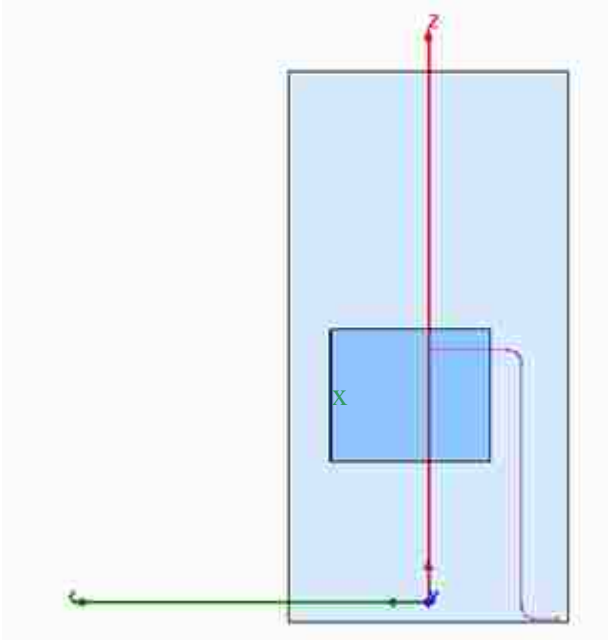

Figure 3.2. Complex HFSS Model – Computation Domain and Cable Source (Side View)

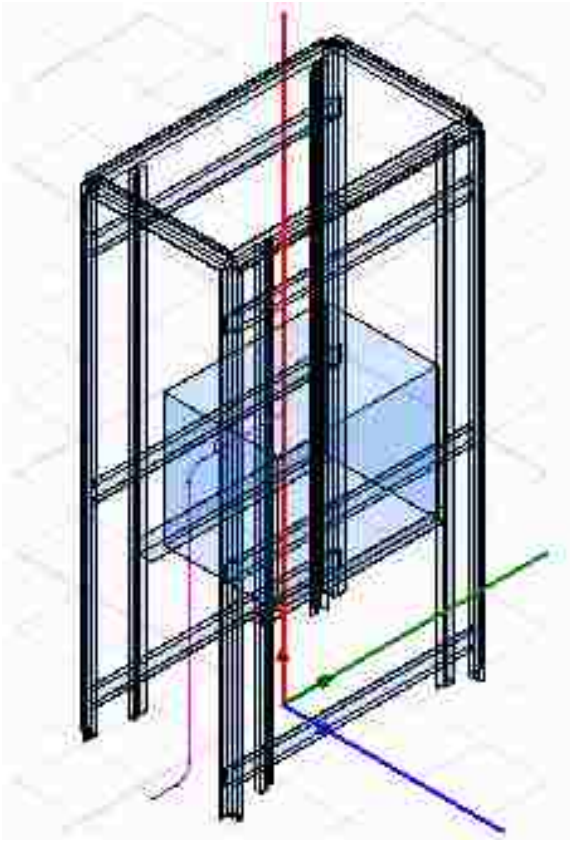

Figure 3.3. Complex HFSS Model – Cabinet Frames 3D View (Without Panels)

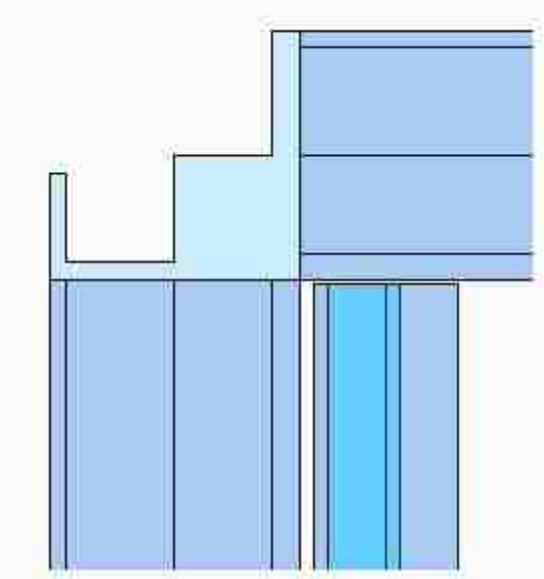

Figure 3.4. Complex HFSS Model – Frame Cross-Section View

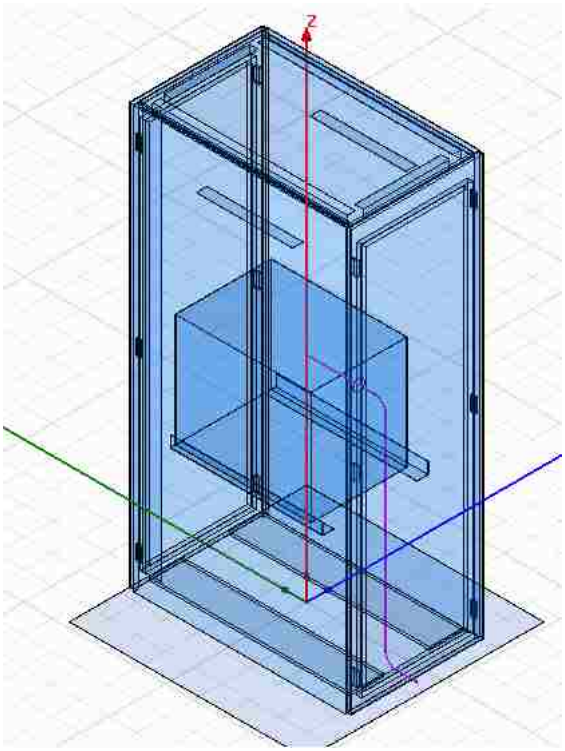

Figure 3.5. Complex HFSS Model – Cabinet Panels 3D View (Without Frames Shown)

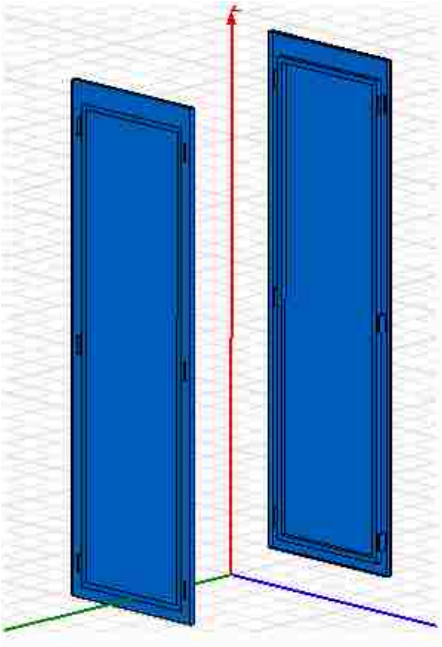

Figure 3.6. Complex HFSS Model – Two Doors (3D View)

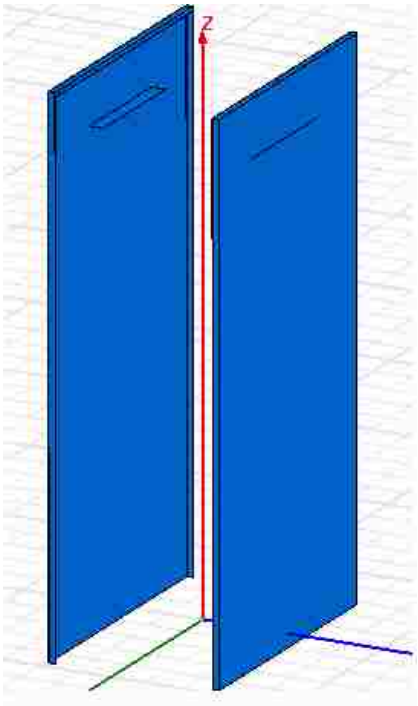

Figure 3.7. Complex HFSS Model – Side Panels (3D view)

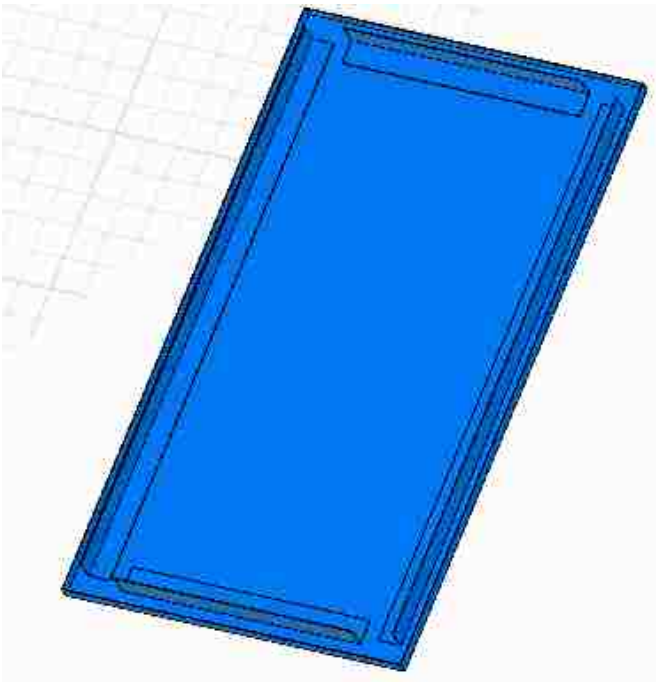

Figure 3.8. Complex HFSS Model – Top Panel (3D View)

3.2.2. Simplified HFSS Model. The complex HFSS model was simplified from the original structure to reduce the memory requirement in the simulation. The major modifications include:

1) The opening of all thin slots is set at one size (1/8 inch).
2) Shape of cross-section of inner frames is simplified to regular rectangles.
3) The angle edges of all doors and panels are removed and the cross-section shape of outer frames is simplified, see Figure 3.9 and Figure3.10.
4) All additional shapes on doors and top panel are removed.
5) Cable radius is increased to 1 inch.

Three different rack cabinet setups are simulated using the simplified HFSS models, as in Figures 3.11 through 3.13, which show the 3D view of the different setups of the cabinet model summarized in Table 3.1. The related simulations are set up as:

i) Boundary: infinite ground plane and radiation boundary condition for the remaining boundaries.
ii) Excitation: current source (1000mA) of the cable with one end in the module and the other end just above the ground plane.
iii) Analysis: frequency range 100MHz to 2GHz.

Table 3.1. Three Different Setups for the Simplified HFSS Model

Simplified Model I	Back door closed, cable (exiting floor) extended by 1 foot
Simplified Model II	Back door taken off, cable (exiting floor) extended by 1 foot
Simplified Model III	Back door closed, cable exiting top

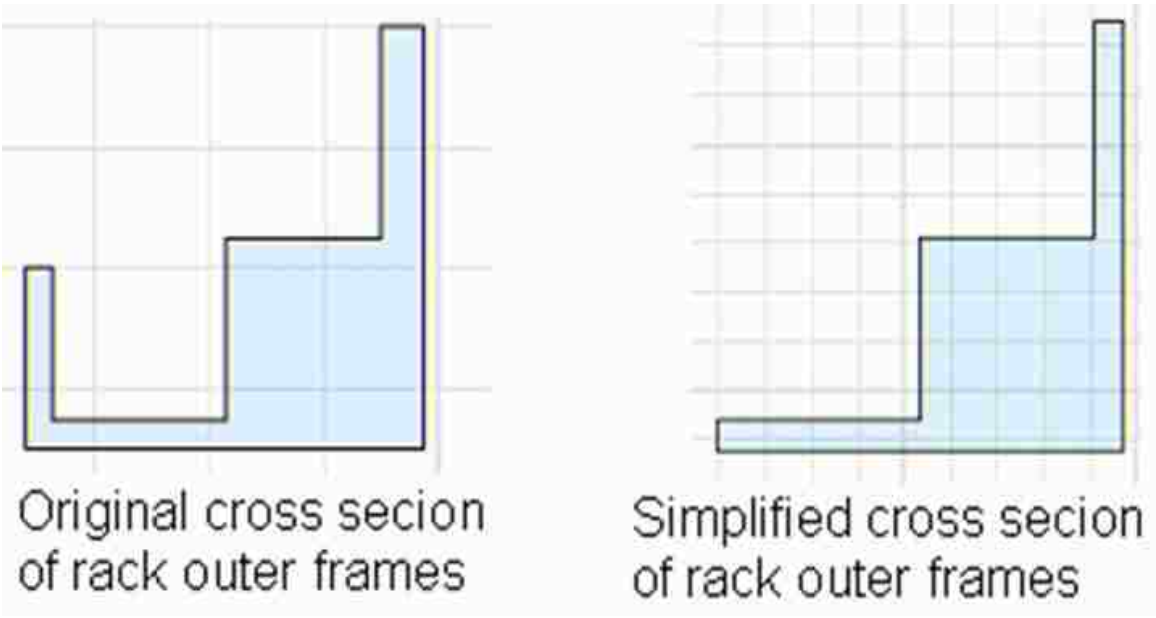

Figure 3.9. Simplified HFSS Model – Cross Section View of the Simplified Outer Frames

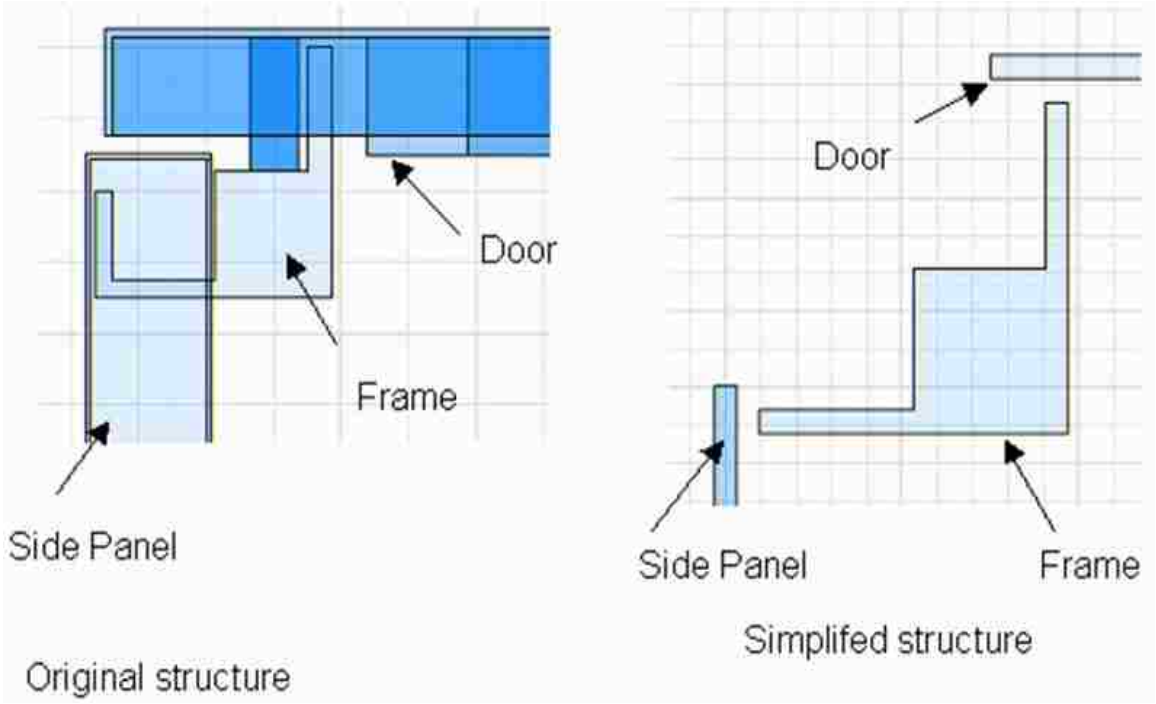

Figure 3.10. Simplified HFSS Model – Cross Section View of the Simplified Panels and Frames

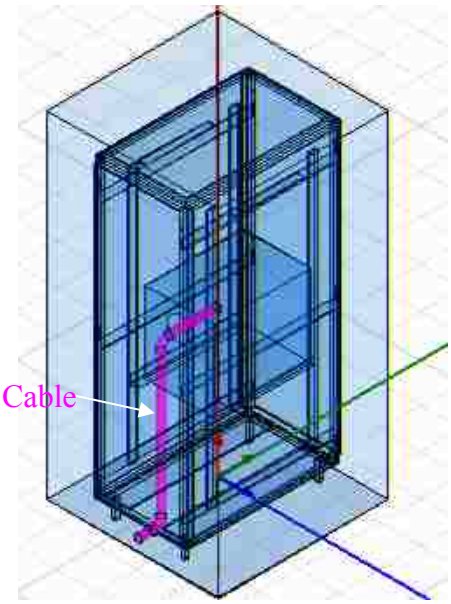

Figure 3.11. Simplified HFSS Model I – Back Door Closed and Cables Exiting the Bottom (3D View).

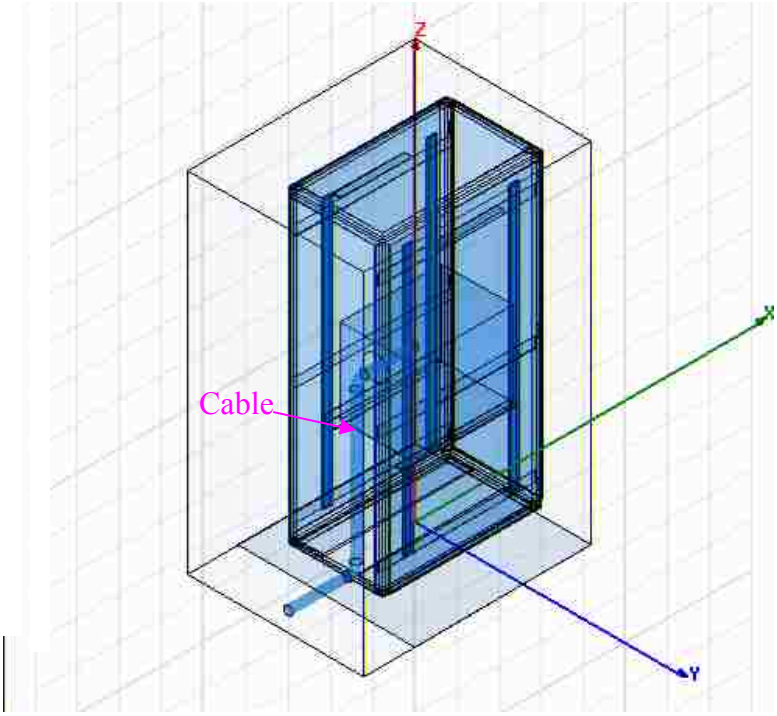

Figure 3.12. Simplified HFSS Model II – No Back Door and Cables Exiting the Bottom (3D View).

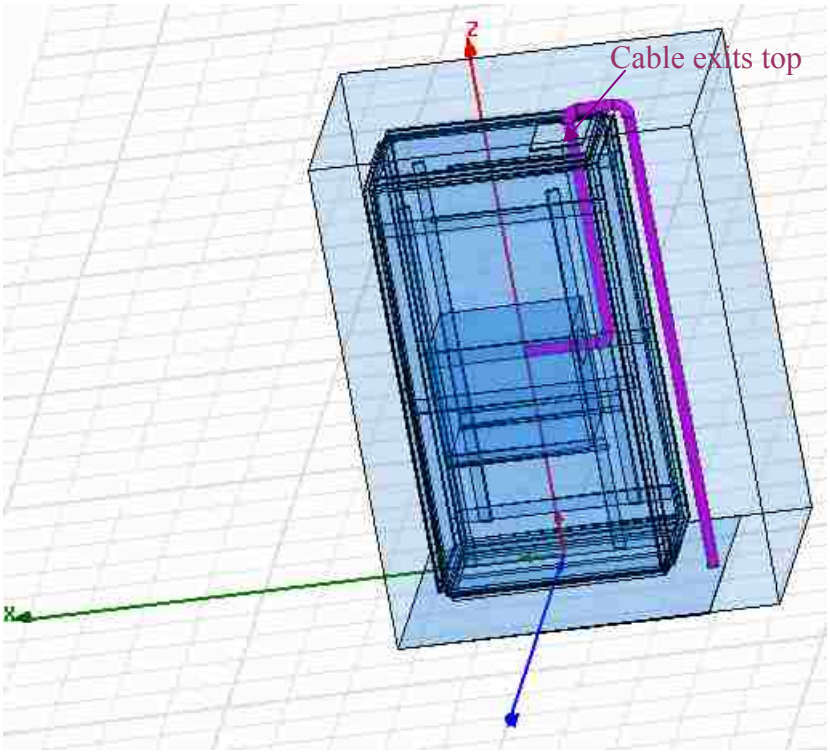

Figure 3.13. Simplified HFSS Model III – Back Door Closed and Cables Exiting the Top (3D View).

3.3. RESULTS

3.3.1. Complex HFSS Model Results. The model passed the validation check in HFSS version 9.2. But HFSS failed to reach a convergence of the adaptive passes and aborted the simulation, as shown by Figure 3.14. No results are available for this model.

3.3.2. Simplified HFSS Model Results. The far field patterns are plotted at frequency of 627 MHz, 1254 MHz and 1881 MHz. The three particular frequencies are the fundamental, the first harmonic and the second harmonic respectively of the BYNET data stream in the real working cabinet [1]. Figures 3.15 through 3.17 show the far field pattern for simplified model I, i.e. with the back door closed and the cable exiting the bottom. Figures 3.18 through 3.20 are plots for the far field pattern for simplified model II with the back door taken off and the cable exiting the bottom, and Figures 3.21 through 3.23 indicate the far field pattern for simplified model III with the back door closed and the cable exiting the top of the node rack.

It is observed that in Model II, when back door is taken off, the maximum electric field at 627 MHz is 370 mV/m (51 dBmV/m), which is about 12 dBmV/m higher than that (93 mV/m or 39 dBmV/m) at the same frequency in model I, when the back door is closed.

Comparing Figure 3.21 with Figure 3.17, it is found that when cable exits the top of the rack, the far field radiation is slightly higher than that when cables exit the bottom, and the field assumes a strong half circle distribution that completely differs with the far field pattern for Model I, where the cable exiting the bottom.

Task	Real Time	CPU Time	Memory	Information
Start				Time: 03/13/2006 11:01:28, Host EMCLAB64, HFSS Version 9.2.1
Mesh Refinement				Lambda Based
wave_I_seed	00:02:11	00:02:10	450976 K	316609 tetrahedra
Adaptive Pass 1				Frequency: 0.8 GHz
adapt_part1	00:02:07	00:02:03	558560 K	316609 tetrahedra
				Adaptive Passes did not converge.
Total	00:04:18	00:04:13		Time: 03/13/2006 11:06:44, Status: Aborted
Start				Time: 03/13/2006 17:30:35, Host EMCLAB64, HFSS Version 9.2.1
Adaptive Pass 1				Frequency: 0.5 GHz
adapt_part1	00:02:06	00:02:03	558560 K	316609 tetrahedra
Solver CSS	00:21:02	00:14:45	1120044 K	1056974 matrix
Disk I/O temp	00:00:00	00:00:00	0 K	2236393 K
adapt_part2	00:00:55	00:00:50	577044 K	316609 tetrahedra
Adaptive Pass 2				Frequency: 0.5 GHz
mesh3d_adapt	00:08:15	00:08:13	320108 K	356044 tetrahedra
adapt_part1	00:02:28	00:02:25	559696 K	356044 tetrahedra
				Adaptive Passes did not converge.
Total	00:34:46	00:28:16		Time: 03/13/2006 20:24:05, Status: Child Process Error
Start				Time: 03/13/2006 21:44:33, Host EMCLAB64, HFSS Version 9.2.1

Figure 1 Error information in Solution Data.

Figure 3.14. Error Information in Solution Data when Running the Complex HFSS Model

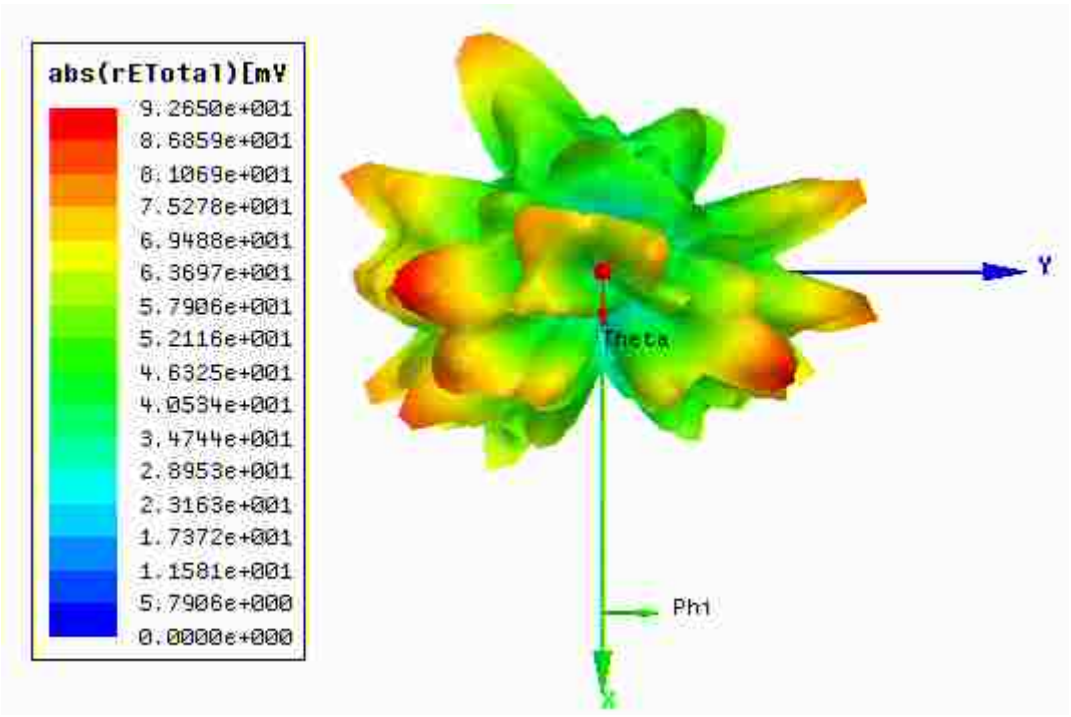

Figure 3.15. Far Field Pattern at f = 627 MHz for Simplified HFSS Model I

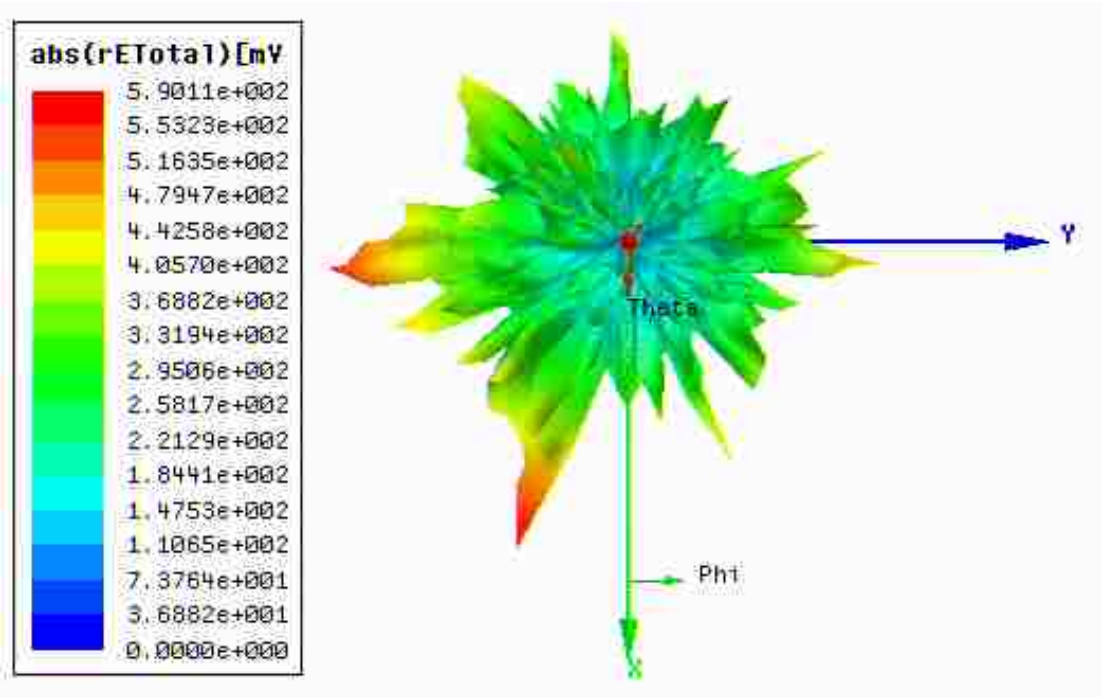

Figure 3.16. Far Field Pattern at f = 1.254 GHz for Simplified HFSS Model I

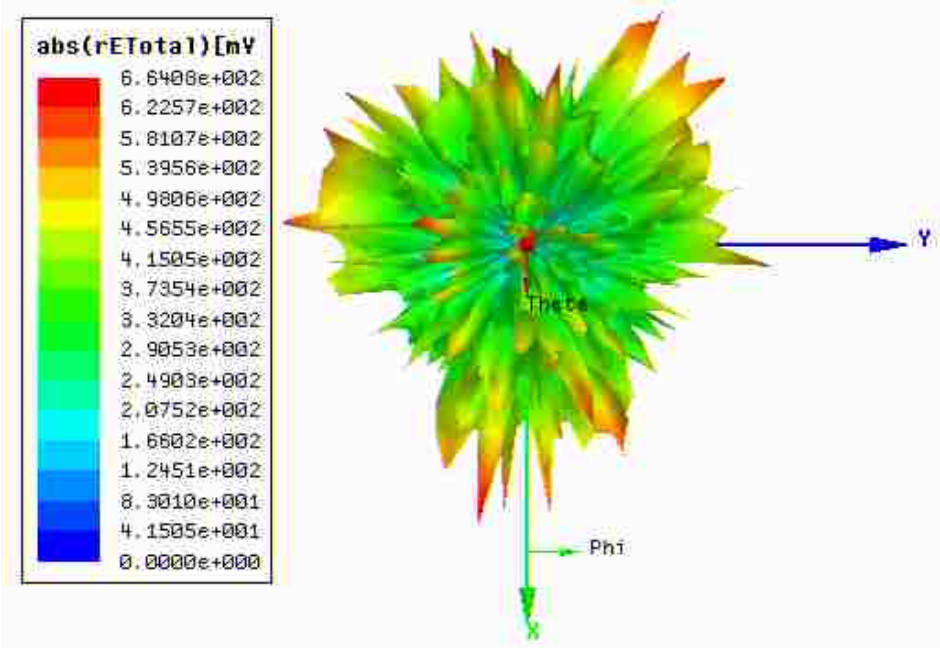

Figure 3.17. Far Field Pattern at f = 1.881 GHz for Simplified HFSS Model I

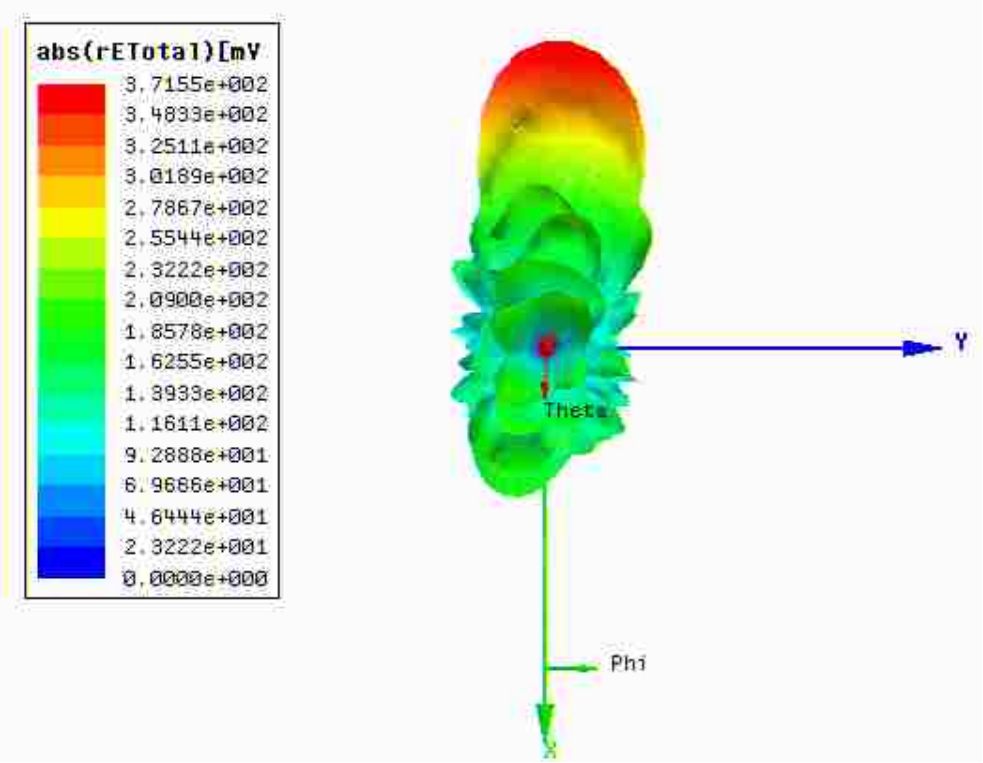

Figure 3.18. Far Field Pattern at f = 627 MHz for Simplified HFSS Model II (Cabinet without Back Door)

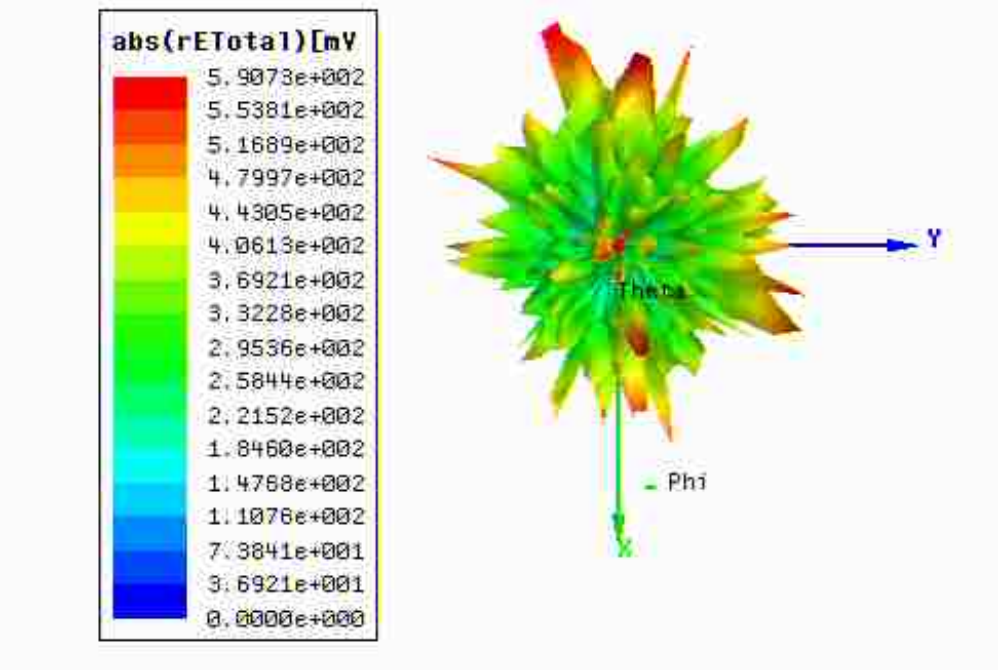

Figure 3.19. Far Field Pattern at f = 1.254 GHz for Simplified HFSS Model II (Cabinet without Back Door)

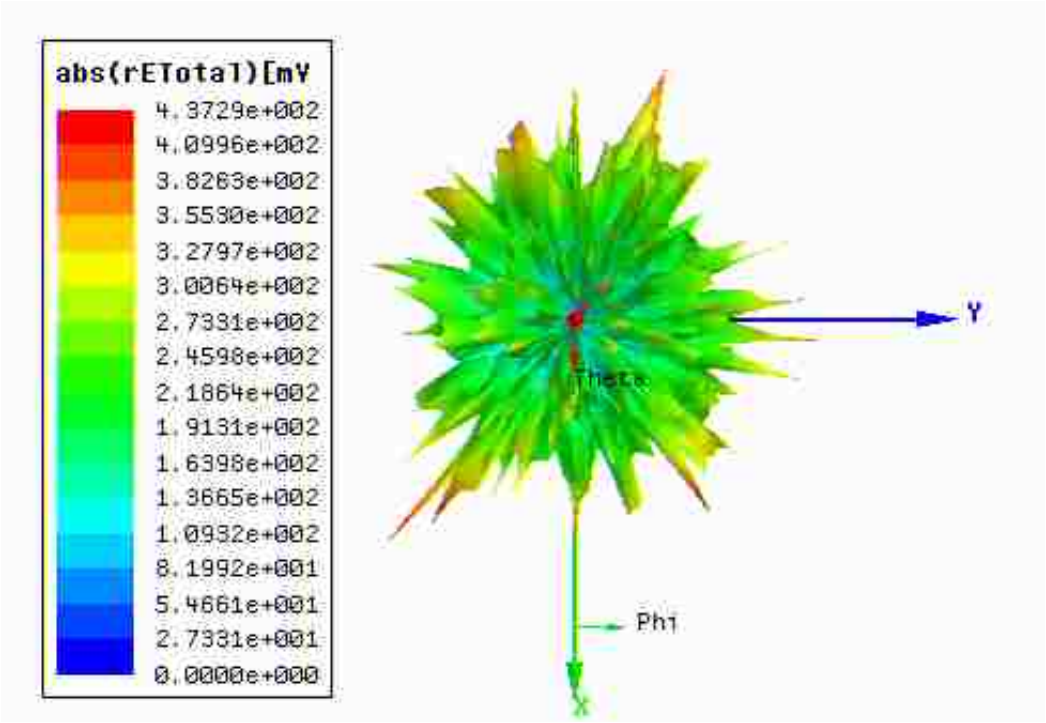

Figure 3.20. Far Field Pattern at f = 1.881 GHz for Simplified HFSS Model II (Cabinet without Back Door)

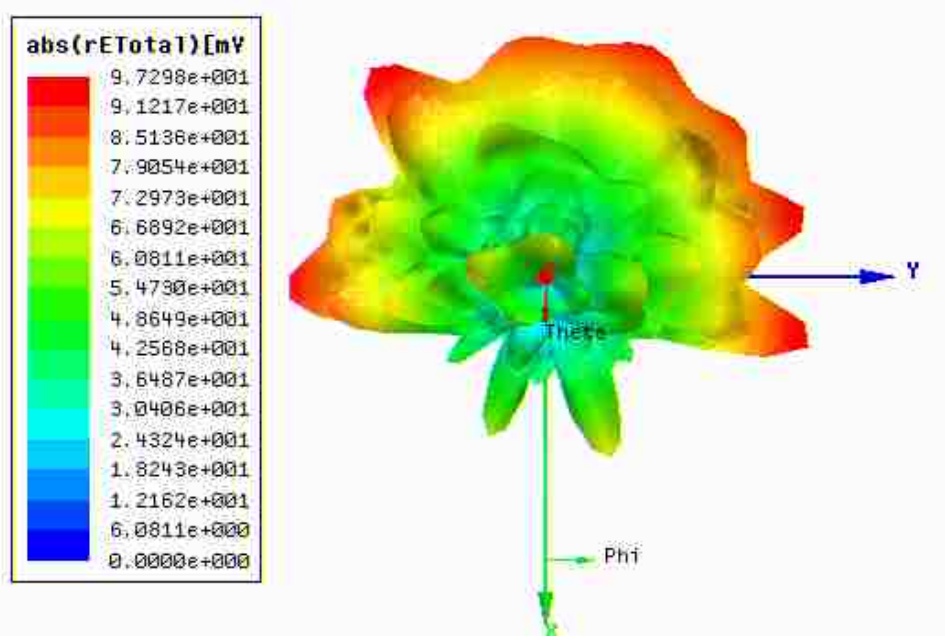

Figure 3.21. Far Field Pattern at f = 627 MHz for Simplified HFSS Model III (Cable Exit Top)

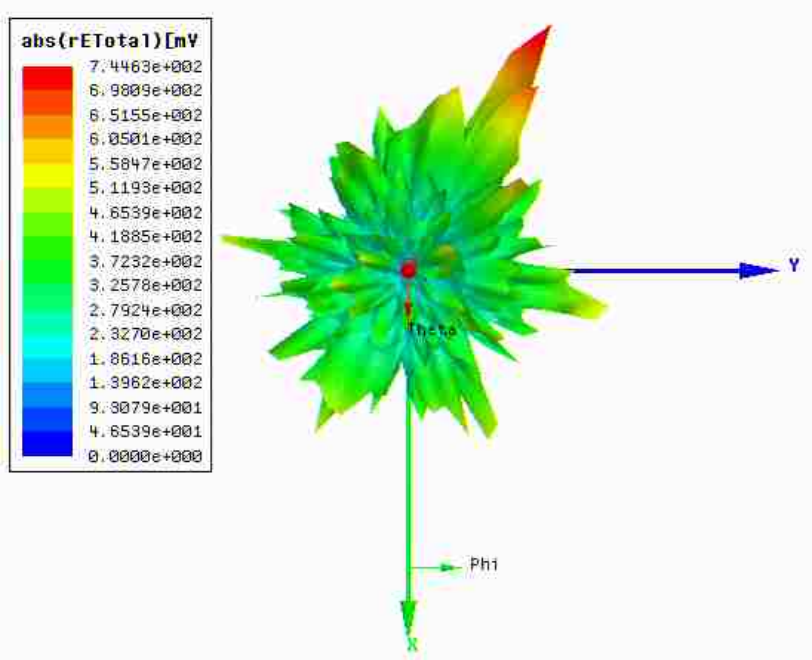

Figure 3.22. Far Field Pattern at f = 1.254 GHz for Simplified HFSS Model III (Cable Exit Top)

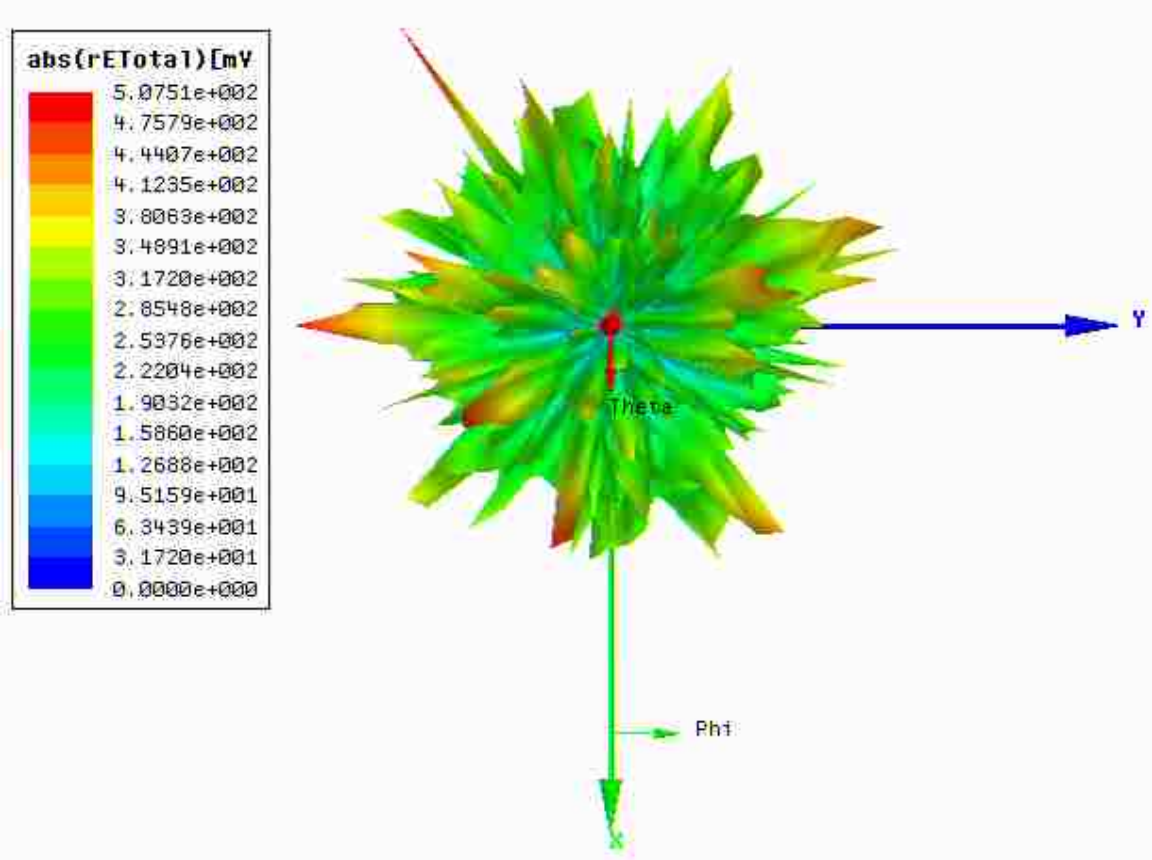

Figure 3.23. Far Field Pattern at f = 1.881 GHz for Simplified HFSS Model III (Cable Exits Top)

3.4. SUMMARY AND CONCLUSIONS

The large size and complex structure of the rack cabinet lead to simulation failure for the complex HFSS model due to its huge demand on the computer memory and space. The simplified model was able to run and the simulations show a general agreement with the results from the EMI measurement of the NCR's working node rack cabinet and of the swept frequency study of a similar node rack cabinet.

BIBLIOGRAPHY

[1] J. L. Drewniak, J. L. Knighten, and J. Flavin, "Investigation of Cable Egress Location and Cabinet Shielding Effectiveness in the NCR Teradata Node Rack," March 21, 2006.

[2] J. L. Knighten, R. D. McLay, P. M. Rostek, and J. Fan, "Cabinet Shielding Inherent in Standard Equipment Racks not Designed to Provide High-Performance Shielding," in *2004 IEEE International Symposium on Electromagnetic compatibility,* Silicon Valley, CA, August, 2004, pp. 528-532.

[3] M. Xu, S. Radu, J. L. Knighten, J. L. Drewniak, T. H. Hubing, L. O. Hoeft and J. T. DiBene II, "Signal Induced EMI in Fibre Channel Cable-Connector Assemblies", in 1999 *IEEE International Symposium on Electromagnetic Compatibility,* Seattle, WA, August, 1999, pp. 201-205.

[4] D. E. Bockelman and W. R. Eisenstadt, "Combined Differential and Common-Mode Scattering Parameter: Theory and Simulation," in *IEEE trans. Microwave Theory Tech.,* Vol 43, No 7, July 1995, pp. 1530-1539.

[5] K. Jung, W. R. Eisenstadt, and R. M. Fox, "SPICE-Based Mixed-Mode S-Parameter Calculations for Four-Port and Three-Port Circuits," in *IEEE trans. Computer-Aided Design of Integrated Circuits and Systems.,* Vol 25, No 5, May 2006, pp. 909-913.

[6] J. Chen , J. L. Drewniak, R. E. DuBroff, J. L. Knighten, J. Fan and J. Flavin, "Predictive Modeling of the Effects of Skew and Imbalance on Radiated EMI from Cables," in *2007 IEEE International Symposium on Electromagnetic Compatibility*, Honolulu, HI, July 2007.

VITA

Jue Chen was born in Jiangsu, People's Republic of China, on June 22, 1970. She received her B.S. from Southeast University, Nanjing, China, in July 1992. From 1992 to 1999, Jue Chen worked as an engineer in Nanjing Electronic Equipment Research Institute. In May 2003, Jue Chen received her M.S. in Mechanical Engineering from University of Missouri-Rolla.

In June 2005, she began her graduate study at the Electromagnetic Compatibility Laboratory in the Department of Electrical Engineering in University of Missouri-Rolla. She received her M.S. in Electrical Engineering in December 2007. She has been a member of IEEE since 2006. She is the winner of the President Memorial Award, IEEE Electromagnetic Compatibility Society, 2007.